
Electronic Thesis and Dissertation Repository

8-22-2012 12:00 AM

Flexural Behaviour of Steel Fibre Reinforced Concrete Tunnel Linings

Martin Blazejowski
The University of Western Ontario

Supervisor
Dr. Tim Newson
The University of Western Ontario

Graduate Program in Civil and Environmental Engineering
A thesis submitted in partial fulfillment of the requirements for the degree in Master of
Engineering Science
© Martin Blazejowski 2012

Follow this and additional works at: <https://ir.lib.uwo.ca/etd>



Part of the [Geotechnical Engineering Commons](#)

Recommended Citation

Blazejowski, Martin, "Flexural Behaviour of Steel Fibre Reinforced Concrete Tunnel Linings" (2012).
Electronic Thesis and Dissertation Repository. 768.
<https://ir.lib.uwo.ca/etd/768>

This Dissertation/Thesis is brought to you for free and open access by Scholarship@Western. It has been accepted for inclusion in Electronic Thesis and Dissertation Repository by an authorized administrator of Scholarship@Western. For more information, please contact wlsadmin@uwo.ca.

FLEXURAL BEHAVIOUR OF STEEL FIBRE REINFORCED CONCRETE TUNNEL LININGS

(Thesis format: Monograph)

By

Martin Blazejowski

Graduate Program in Engineering Science
Department of Civil and Environmental Engineering

A thesis submitted in partial fulfillment
of the requirements for the degree of
Master of Engineering Science

The School of Graduate and Postdoctoral Studies
The University of Western Ontario
London, Ontario, Canada

© Martin Blazejowski 2012

THE UNIVERSITY OF WESTERN ONTARIO
School of Graduate and Postdoctoral Studies

CERTIFICATE OF EXAMINATION

Supervisor

Examiners

Dr. Sean Hinchberger

Dr. Tim Newson

Dr. K.Y. Lo

Dr. J.T. Wood

The thesis by

Martin Andrew Blazejowski

entitled:

**Flexural Behaviour of Steel Fibre Reinforced Concrete Tunnel
Linings**

is accepted in partial fulfillment of the
requirements for the degree of
Master of Engineering Science

Date

Chair of the Thesis Examination Board

ABSTRACT

The promotion of steel fibre reinforced concrete (SFRC) as a construction material for tunnel linings has prompted a number of researchers to focus on methods of evaluating their flexural strength and stiffness. This thesis presents the results of an experimental and numerical investigation of the flexural behaviour of full-scale steel fibre reinforced concrete tunnel lining segments. A series of a three-point flexure tests were performed to evaluate the maximum load carrying capacity, the load-deformation behaviour and crack propagation characteristics of these segments. The material properties of the steel fibre reinforced concrete were also studied, using both destructive and non-destructive methods. Element compression and tension tests were conducted to characterize the compressive and tensile strength properties of the SFRC. Additionally, computed tomographic scanning was conducted to analyse and estimate the density fraction and fibre orientation of the fibres in SFRC cores. Three-dimensional finite element analyses were conducted to calibrate a concrete damage plasticity constitutive model and provide better understanding of the segment flexural behaviour. The experimental program indicated that the variation in structural performance of the segments was likely due to an inhomogeneity of fibre distribution and orientation. Modifying the numerical model to account for these variations resulted in a more accurate analysis. Furthermore, from the numerical finite element analysis it was found that the non-linear elasto-plastic concrete damage plasticity model in the crack zone of the beam was mesh dependent. Parametric analyses also revealed that the model was particularly sensitive to small changes to the tensile material property input parameters.

Keywords: Steel Fibre Reinforced Concrete, Tunnel Lining Segment, Finite Element Modeling, Full Scale Testing, Flexural Strength, Micro CT, Stress-Strain, Cracking.

DEDICATION

To my family

ACKNOWLEDGEMENTS

The author would like to thank his advisor Dr. Tim Newson for the guidance, encouragement, and support which he has provided throughout the duration of the thesis.

The author also wishes to express his gratitude to Dr. Sean Hinchberger who has acted as a mentor and provided him with countless opportunities to better himself as a person and a professional throughout his university career.

The author is grateful to the Natural Sciences and Engineering Research Council of Canada and the IPS sponsoring company Hatch, for the funding that he received during the duration of his study.

The author would also like to express his gratitude to William E. and Ruth Lardner for their generous contribution. Your kindness will forever be cherished.

In addition the author would like to thank the laboratory staff, Mr. Wilbert Logan and Ms. Melodie Richards for their knowledge and help as well as moral support.

Finally, the author would like to thank his family, friends, girlfriend, and especially his parents who have sacrificed so much in their lives in order to provide their children with opportunities they did not have growing up. This diploma is just as much yours as it is mine.

TABLE OF CONTENTS

CERTIFICATE OF EXAMINATION.....	ii
ABSTRACT.....	iii
DEDICATION	iv
ACKNOWLEDGEMENTS	v
TABLE OF CONTENTS.....	vi
LIST OF FIGURES	ix
LIST OF TABLES	xv
NOTATION	xvi
CHAPTER 1 - INTRODUCTION.....	1
1.1 Overview	1
1.2 Objectives	3
1.3 Structure of the Thesis.....	4
CHAPTER 2 - LITERATURE SURVEY	6
2.1 Introduction	6
2.2 Steel Fibre Reinforced Concrete	7
2.2.1 Steel Fibre Characteristics	7
2.2.2 Steel Fibre Reinforced Concrete Stress Block Diagrams	12
2.2.3 Comparison of SFRC and Reinforced Concrete.....	15
2.3 Tunnelling	17
2.3.1 Tunnel Boring.....	19
2.3.2 Steel Fibre Reinforced Concrete Tunnel Lining.....	21
2.3.3 In-situ Shotcrete Tunnel Linings	23
2.3.4 Precast Segment Tunnel Linings	23
2.3.5 Forces Acting on Tunnel Linings	26
2.4 Previous Structural Testing	29
2.4.1 Full Scale Testing	29
2.4.2 Small Scale Testing	39

2.5	Numerical Modelling	41
2.5.1	Ahn (2011).....	41
2.5.2	Sorelli <i>et al.</i> , (2005).....	44
2.6	Summary	46
CHAPTER 3 - METHODOLOGY		48
3.1	Introduction	48
3.2	Segment and Site Description	49
3.3	Arrangement for Conducting Flexure Test.....	53
3.3.1	Experimental Loading System.....	53
3.3.2	Loading Frame	54
3.3.3	Reaction Frame	56
3.3.4	Test Procedures.....	57
3.4	Instrumentation of Segments.....	58
3.4.1	Displacement Transducers	58
3.4.2	Strain Gauges	58
3.4.3	Crack Monitoring.....	60
3.4.4	Computed Tomography	62
3.5	Finite Element Numerical Analysis	65
3.5.1	ABAQUS Concrete Model	65
3.5.2	Loading and Boundary Conditions	70
3.5.3	Mesh Development	71
3.6	Compressive Material Properties	74
3.6.1	Analytical Solution	74
3.6.2	Experimental Cylinder Strength Tests	77
3.7	Tensile Material Properties	81
3.7.1	Flexural Beam Testing.....	81
3.7.2	Experimental Beam Tests	83
3.7.3	Tensile Stress-Strain Approximation.....	85
3.7.4	Verification of Tensile Parameters	90
3.7.5	Experimental Split Cylinder Tests.....	93
3.8	Summary	94
CHAPTER 4 - EXPERIMENTAL RESULTS		96
4.1	Introduction	96
4.2	Load-Deflection Response	97
4.2.1	Pilot Test (SFRC-P).....	97
4.2.2	Tests SFRC-1 to SFRC-6.....	98

4.3	Load-Strain Response.....	108
4.3.1	Pilot Test (SFRC-P).....	108
4.3.2	Tests SFRC-1 to SFRC-6.....	109
4.4	Crack Propagation Analysis	113
4.5	Fracture Energy and Toughness Characterization.....	118
4.6	Concrete Core Computed Tomography Scanning.....	122
4.7	Summary	124
CHAPTER 5 - FINITE ELEMENT MODELING		126
5.1	Introduction	126
5.2	Tunnel Lining Segment Response Predictions.....	127
5.3	Modified Analysis Study	131
5.4	Sensitivity Analysis	135
5.4.1	Modified Modulus of Elasticity Parameter.....	136
5.4.2	Modified Tensile Stress-Strain Parameters	138
5.5	Location of the Neutral Axis	144
5.6	Summary	146
CHAPTER 6 - SUMMARY AND CONCLUSIONS.....		148
6.1	Summary	148
6.2	Recommendations for Future Work	151
REFERENCES.....		152
APPENDIX A – Mesh Sensitivity Analysis		158
APPENDIX B – Input Parameter Sensitivity Analysis		159
APPENDIX C – Neutral Axis Location Analysis		163
CURRICULUM VITAE		167

LIST OF FIGURES

Figure 2.1 - Fibre shape (Ghoraishi <i>et al.</i> , 2011)	8
Figure 2.2 - Toughness of SFRC with varying fibre volume (Chanh, 1999)	9
Figure 2.3 - Effect of segment production on the fibre orientation (De Waal, 1999).....	11
Figure 2.4 - Load-deflection curve of different cracking phases of steel fibre reinforced concrete beam (Tlemat <i>et al.</i> , 2006)	13
Figure 2.5 - Schematic representation of a steel fibre reinforced concrete beam under flexural loading (Tlemat <i>et al.</i> , 2006)	14
Figure 2.6 - Typical tunnel lining rebar cage assembly	15
Figure 2.7 - Tunnel lining reinforcement sections (Rancourt <i>et al.</i> , 2007).....	18
Figure 2.8 - Tunnel Boring Machine	20
Figure 2.9 - Precast segment linings (a) a stacked full tunnel ring, (b) storage yard.....	24
Figure 2.10 - Tunnel ring assembly mock up	25
Figure 2.11 - Segmented tunnel liner casting bed.....	25
Figure 2.12 - Typical moments acting on a tunnel liner (Mashimo <i>et al.</i> , 2002)	26
Figure 2.13 - Bending due to inadequate grout filling (Gettu <i>et al.</i> , 2004)	27
Figure 2.14 - Moment loads acting on stored segments	28
Figure 2.15 - Schematic diagram of the flexure test (Moccichino <i>et al.</i> , 2006)	29
Figure 2.16 - Flexural test: load vs. midspan displacement (Moccichino <i>et al.</i> , 2006)	30
Figure 2.17 - Flexural test: load vs. crack width (Moccichino <i>et al.</i> , 2006)	30
Figure 2.18 - Flexural test set-up and instrumentation (Poh <i>et al.</i> , 2009).....	32
Figure 2.19 - Plain concrete flexure test: load-midspan displacement (Poh <i>et al.</i> , 2009)	33

Figure 2.20 - SFRC flexure test: load- midspan displacement (Poh <i>et al.</i> , 2009)	33
Figure 2.21 - Various loadings simulating different ground conditions (Mashimo <i>et al.</i> , 2002)	34
Figure 2.22 - Experimental setup (Ahn, 2011)	38
Figure 2.23 - Load-displacement comparison of plain and TSL covered tunnel lining segments subjected to flexural loading (Ahn, 2011).....	38
Figure 2.24 - A bench-scale model (1/30) test setup (Aruga <i>et al.</i> , 2007).....	40
Figure 2.25 - Finite element geometry of the segmented concrete liner (Ahn, 2011)	42
Figure 2.26 - A comparison between experimental and finite element results (Ahn, 2011)	42
Figure 2.27 - Experimental tensile test response (Sorelli <i>et al.</i> , 2005)	44
Figure 2.28 - (a) Test setup, (b) Experimental and finite element response (Sorelli <i>et al.</i> , 2005)	45
Figure 3.1 - Toronto-York Spadina subway extension map (TTC)	50
Figure 3.2 - Detail drawing of segment tunnel lining (HMM)	51
Figure 3.3 - Geometry of the Dramix -80/60- steel fibre	52
Figure 3.4 - Experimental system	53
Figure 3.5 - Loading frame	54
Figure 3.6 - Frame force distribution	55
Figure 3.7 - Support system layout	56
Figure 3.8 - Strain gauge and transducer layout	59
Figure 3.9 - Crack monitoring area	60
Figure 3.10 - (a) crack propagation (SFRC-6), (b) magnified image of CMOD	61

Figure 3.11 - Gray scale intensity profile plot of crack width (SFRC-6)	61
Figure 3.12 - General view of computed tomography scanning machine (Caliskan, 2007)	63
Figure 3.13 - Typical steel fibre reinforced concrete core computed tomography image	64
Figure 3.14 - Uniaxial loading concrete response (a) compression and (b) tension (ABAQUS, 2006).....	67
Figure 3.15 - Bi-linear yield surface of concrete (ABAQUS, 2006)	68
Figure 3.16 - Boundary conditions and loading distribution	70
Figure 3.17 - Element types: tetrahedral, wedge, and hexahedral	71
Figure 3.18 - Stress-strain curve for 60 MPa concrete used in the finite element analysis	75
Figure 3.19 - Coring machine setup.....	77
Figure 3.20 - Concrete cylinders equipped with sulfur caps and vertical strain gauge	78
Figure 3.21 - Cylinder core compressive stress-strain.....	80
Figure 3.22 - Standardized flexural beam test setup (Jankowiak <i>et al.</i> , 2005)	82
Figure 3.23 - Beam testing apparatus as per ASTM C78-10 (2010)	83
Figure 3.24 - Typical beam test load-deflection data (TEC Services, 2010).....	84
Figure 3.25 - Bi-linear approximation of the post-cracking behaviour of SFRC	85
Figure 3.26 - Approximated SFRC tensile stress-strain behaviour	89
Figure 3.27 - Finite element beam test model (425 elements).....	90
Figure 3.28 - Finite element model with (a) coarse, (b) medium, and (c) fine meshes	91
Figure 3.29 - Comparison of varying mesh size with experimental beam test behaviour	92
Figure 4.1 - Load-displacement response of pilot test SFRC-P.....	97

Figure 4.2 - Load-vertical deflection curves of the segments	101
Figure 4.3 - A vertical displacement-load comparison for LVDT D-1 (central midspan)	103
Figure 4.4 - Load-transverse deflection curves of the segments.....	107
Figure 4.5 - Pilot test (SFRC-P) tensile strain vs. load	108
Figure 4.6 - Load-strain curves of the segments	112
Figure 4.7 - Crack width propagation at midspan load deflection (SFRC-5)	114
Figure 4.8 - Crack width at specified load-displacement (SFRC-5).....	115
Figure 4.9 - Crack width at specified load-displacement (SFRC-6).....	115
Figure 4.10 - Crack width propagation at midspan load deflection (SFRC-6)	116
Figure 4.11 - CMOD vs. midspan deflection (SFRC-5 & 6)	117
Figure 4.12 - Load-CMOD curve with toughness indices points (SFRC-5)	119
Figure 4.13 - Load-CMOD curve with toughness indices points (SFRC-6)	119
Figure 4.14 - Toughness indices of specimens (Deng <i>et al.</i> , 2006)	120
Figure 4.15 - Computed tomography fibre density (%) and orientation (SFRC-1 & -2)	123
Figure 4.16 - Load-midspan displacement (SFRC-1 & -2)	123
Figure 5.1 - Finite element lining segment model (12,528 elements)	127
Figure 5.2 - A comparison between experimental and finite element results (at D-1) ...	129
Figure 5.3 - A comparison between experimental and finite element results (at S-2)....	129
Figure 5.4 - A comparison between experimental and finite element results (at S-3)....	130
Figure 5.5 - Finite element lining model with top section modelled as plain concrete ..	131
Figure 5.6 - A comparison between experimental, finite element and modified finite element results (at D-1).....	133

Figure 5.7 - A comparison between experimental, finite element and modified finite element results (at S-2)	134
Figure 5.8 - A comparison between experimental, finite element and modified finite element results (at S-3)	134
Figure 5.9 - Comparison between original and modified finite element analysis with input modulus of elasticity ($\pm 50\%$) at D-1	137
Figure 5.10 - Modified approximation of SFRC tensile stress input parameters	138
Figure 5.11 - Comparison between original and modified finite element results at D-1 with modified tensile softening stress ($\pm 30\%$)	139
Figure 5.12 - Modified approximation of SFRC tensile strain input parameters	140
Figure 5.13 - Comparison between the original and finite element results at D-1 with modified tensile softening strain ($\pm 30\%$)	141
Figure 5.14 - Modified approximation of SFRC tensile stress-strain slope (AB) input parameters	142
Figure 5.15 - Comparison between the original and modified finite element results at D-1 with modified tensile stress strain slope (AB) ($\pm 30\%$)	143
Figure 5.16 - Finite element tensile and compressive strain plot.....	145
Figure 5.17 - Comparison between the experimental and modified finite element neutral axis movement at the midspan of the tunnel lining segment	145
Figure A.1 - Number of mesh elements vs. numerical peak load	158
Figure B.1 - Comparison between experimental and finite element results at D-1 with modified compressive stress-strain relationship ($\pm 50\%$)	160

Figure B.2 - Comparison between experimental and finite element results at D-1 with modified Poisson's ratio (± 0.5)	161
Figure B.3 - Comparison between experimental and finite element results at D-1 with modified concrete density ($\pm 100\%$)	162
Figure C.1 - Numerical strain plot diagrams.....	164

LIST OF TABLES

Table 2.1 - History of steel fibre reinforced concrete tunnels (Hansel <i>et al.</i> , 2011).....	22
Table 2.2 - ABAQUS material input parameters (Ahn, 2011)	41
Table 3.1 - Geometrical properties of TTC Spadina Line extension tunnel lining.....	51
Table 3.2 - Steel fibre specifications.....	52
Table 3.3 - Setting used for CT scanning of cores.....	64
Table 3.4 - Material and concrete damage plasticity (CDP) parameters	69
Table 3.5 - Concrete core compressive strength results.....	79
Table 3.6 - Limit of proportionality and residual flexural loads.....	86
Table 3.7 - Tension stiffening stress-strain input parameters	89
Table 3.8 - Tensile split cylinder strength results	93
Table 4.1 - Average and standard deviation of segment flexure test behaviour	103
Table 5.1 - Tensile stress-strain parameters for plain concrete.....	132
Table 5.2 - Material parameter impact on the model output.....	135
Table 5.3 - Modified modulus of elasticity input parameters	136
Table 5.4 - Modified tension stiffening stress numerical input parameters.....	138
Table 5.5 - Modified tension stiffening strain numerical input parameters.....	140
Table 5.6 - Modified tension stiffening slope (AB) numerical input parameters	142
Table B.1 - Parameter impact on the model output	159
Table C.1 - Summary of experimental and numerical neutral axis location against displacement.....	163

NOTATION

β	fibre influence factor
δ_i	flexure beam deflection (mm)
ε	arbitrary strain
ε_o	strain at peak stress
f_c'	compressive strength (MPa)
f_t	tensile strength (MPa)
ρ	density of concrete (kg/m ³)
σ_c	compressive stress (MPa)
σ_i	uniaxial tensile stress (MPa)
σ_{c0}/σ_{b0}	initial biaxial/uniaxial ratio
b	width of the specimen (mm)
μ	viscosity parameter
$\mu\varepsilon$	micro-strain (10 ⁻⁶)
γ	specific weight of concrete (kN/m ³)
Ψ	dilation angle
C_i	stress coefficients
E_c	modulus of elasticity (MPa)
f_{Ri}	residual flexural tensile strength (MPa)
F_L	limit of proportionality (kN)
F_{Ri}	residual flexural loads (kN)
h	height of the specimen (mm)
K_c	second stress invariant on the tensile meridian/compressive meridian
k_h	size factor
L	length of the specimen (mm)
m	flow potential eccentricity
V_f	steel fibre volumetric fraction (%)
<i>ASTM</i>	American society for testing and materials

<i>CDP</i>	concrete damage plasticity model
<i>CMOD</i>	crack mouth opening displacement
<i>CSC</i>	concrete smeared crack model
<i>CT</i>	computed tomography
<i>FE</i>	finite element
<i>LVDT</i>	linear variable displacement transducer
<i>SFRC</i>	steel fibre reinforced concrete
<i>TBM</i>	tunnel boring machine
<i>TLS</i>	tunnel lining segment
<i>TYSSE</i>	Toronto York Spadina subway extension

INTRODUCTION

1.1 Overview

Applications of steel fibre reinforced concrete (SFRC) have increased in civil infrastructure due to enhanced tensile behaviour, increased toughness and better crack arrestment properties (Burgers 2006). These advantageous material characteristics are of particular interest for application to tunnel support systems. Therefore, designers, contractors and other stake-holders of the tunnelling industry are becoming more interested in employing SFRC due to its structural, durable and long-term characteristics. In addition, the application of SFRC tunnel lining segments can result in material, labour, and manufacturing cost savings. However, there is currently a lack of clear design guidelines and construction procedures for SFRC members and tunnel linings in particular. As a result, SFRC members are often over-conservatively designed or even avoided, and replaced with more traditional reinforced concrete sections.

An efficient way to determine the load carrying capacity of a tunnel lining is to perform full-scale tests on full ring segmented linings. However, such methods are case specific, and can be highly expensive and time consuming. In addition, it is difficult to apply the range of loads that may be experienced in the field within a laboratory environment. Finite element modelling is a good complementary technique to prototype testing, but can still lack key predictive components; it can be difficult to take into account and model a number of aspects, such as non-homogeneity and non-linearity in materials, initiation and

propagation of cracking in the structure, and appropriate boundary and loading conditions.

To further develop these methods and provide greater understanding for use in design, this study has examined the flexural resistance and crack development of SFRC tunnel lining segments using experimental and numerical methods. The research was conducted on prototype scale segments, which eliminates discrepancies encountered through model experimental testing. Full-scale experimental tests, using a three-point flexure setup, were performed on SFRC tunnel segments to establish the load and displacement characteristics, crack bridging properties and material behaviour. Furthermore, a numerical analysis was performed using the ABAQUS (Version 6.8.1), finite element software to provide further interpretation of the full-scale testing and to calibrate the concrete damage plasticity constitutive model in the finite element coding.

This study will enhance the coupling between prototype testing and numerical modelling, and develop improved methods that will more accurately predict the load carrying capacity and cracking of SFRC tunnel linings. In addition, it will assist in developing a calibrated method of predicting the performance of future SFRC tunnel liners, subject to different forms of loading, as well as providing support for the development of new design methods.

1.2 Objectives

- i. To review the state-of-the-art literature for steel fibre reinforced concrete technology used for segmented tunnel linings, compile a summary of SFRC tunnel lining test methods and evaluate current design methods to identify areas requiring improvement.
- ii. To evaluate the flexure load carrying capacity of full scale SFRC segmented tunnel linings using three-point bending tests and compile a database of behaviour covering load-displacement, load-strain and crack propagation response.
- iii. To generate a non-linear elasto-plastic finite element model to interpret the observed behaviour in the laboratory testing and to calibrate an advanced concrete damage plasticity constitutive model for cracked SFRC concrete, in an attempt to contribute to methods of design of SFRC members.
- iv. To monitor and assess crack initiation and propagation of SFRC segments during flexural loading.
- v. To investigate the effects of fibres on the strength and stiffness properties of SFRC, using standard laboratory tests and investigate the distribution of the fibres from the lining casting process using computed tomography scanning.
- vi. To link the material properties and spatial distribution of fibres through the casted lining segments to the observed results in the experimental flexure tests.

1.3 Structure of the Thesis

This thesis consists of six chapters. Following the introductory chapter, Chapter 2 presents a detailed literature survey of current tunneling methods, steel fibre reinforced concrete material properties, constitutive models and usage, full and reduced scale experimental SFRC tunnel lining testing and numerical modelling analysis methods.

In Chapter 3, the testing procedures, for the experimental and numerical investigations, are discussed in detail. The segment properties and geometry, material properties, laboratory testing system (e.g. support frame, loading frame, loading cell actuator and data acquisition), finite element simulation technique and material testing methods are all described.

Chapter 4 presents the obtained experimental testing results. This includes load-deflection, load-strain, and crack propagation behaviour from the full scale tunnel lining segment testing. Furthermore, image analysis was used to determine the crack initiation, propagation and to quantify the crack mouth opening displacement. Lastly, computed tomography scanning was employed to establish the internal fibre structure of the concrete mix, resulting from the casting process.

In Chapter 5, the flexural resistance and material behaviour of SFRC tunnel lining segments is analyzed using the finite element software ABAQUS. The experimental results are compared with the finite element analysis to provide greater understanding and to calibrate the constitutive model. Further interpretation of the results is provided by a modified study that elucidates the effects of the fibre distribution through the lining

thickness. Furthermore, a sensitivity analysis is performed to quantify the effects that variability of input parameters in a numerical model have on the model output.

Chapter 6 summarizes conclusions from the research and provides recommendations for future studies.

LITERATURE SURVEY

2.1 Introduction

This chapter presents a detailed literature survey of the mechanical properties of steel fibre reinforced concrete, current tunneling design methods, experimental full and reduced-scale flexure testing methods of tunnel linings and previous attempts to numerically model tunnel linings. Steel fibre reinforced concrete is a construction material that is being used more often in civil infrastructure due to its enhanced mechanical properties (e.g. increased toughness and better crack arrestment properties). These advantageous material characteristics are particularly of interest in the application of tunnel support systems and so new industry projects and research studies have been emerging at an increasing rate.

The main objectives of this chapter are: *(i)* to provide a background for steel fibre reinforced concrete material characteristics, *(ii)* to outline the various uses of tunnels and summarize the equipment and methods used in current tunneling practices, *(iii)* to review previous experimental testing methods for assessing the flexural capacity of tunnel lining segments and *(iv)* examine the approaches taken with the finite element numerical model for analysis of segmented tunnel linings.

2.2 Steel Fibre Reinforced Concrete

Steel fibre reinforced concrete (SFRC) is a heterogeneous structural material comprising of typical concrete elements, with the addition of steel fibres to provide tensile resistance. These fibres are discontinuous discrete entities and are distributed and oriented randomly (nominally uniformly) throughout the concrete matrix. SFRC can be used by itself, or in conjunction with conventional reinforcing bars, depending on the application (Banthia, 2001).

2.2.1 Steel Fibre Characteristics

SFRC is a composite material, with the ultimate performance being directly affected by the concrete mixture design, material selection and casting quality control (i.e. fibre type, fibre aspect ratio¹, volume fraction and uniform distribution). A description of how each of these components plays a role in dictating the material behaviour is discussed below.

ASTM A820-06 (Standard Specification for Steel Fibres for Fibre-Reinforced Concrete) provides a classification of five general types of steel fibres based upon their manufacturing process:

1. Type I, cold-drawn wire
2. Type II, cut sheet
3. Type III, melt-extracted
4. Type IV, mill cut
5. Type V, modified cold-drawn wire

Type I fibers have tensile strengths ranging from 1000 to 3000 MPa, while Types II, III, IV, and V have a tensile strength as low as 350 MPa. Fiber shapes range from round

¹ Aspect ratio is the ratio of length to diameter for the fibre (l/d)

² Balling is an effect where fibres entangle into large clumps or balls in a mixture

wires with deformed ends (Type I), rectangular or square rod shapes with dimples (Type II), triangular cross-section and twisted (Type V), or crescent cross-section and corrugated (Type V), as well as other shapes. They also come in different lengths, ranging from 5 mm to more than 50 mm. Longer fibers tend to perform better, however they can be more difficult to mix well into the concrete. To solve this problem, manufacturers often bundle fibers using water-soluble glue to achieve better dispersion in concrete during mixing (Burgers, 2006).

For conventionally mixed fibre reinforced concrete, a higher aspect ratio of fibres results in superior post-peak performance due to the high pullout resistance of the fibres. However, research shows that a high aspect ratio of fibres can lead to a balling² effect during mixing, resulting in loss of flexural resistance and consequently an adverse effect. Generally, aspects ratios of steel fibres between 20 and 100 are used in concrete mixtures (ACI 544.1R-96, 1996, ACI 544.3R-2, 1998). To maintain high pullout resistance while reducing the aspect ratio, a number of approaches are employed: enlarging or hooking the fibre ends, roughening the surface of the fibres, or crimping to produce a wavy, rather than straight fibre. Figure 2.1 illustrates hooked end, waved, and straight fibres.



Figure 2.1 - Fibre shape (Ghoraishi *et. al.*, 2011)

² Balling is an effect where fibres entangle into large clumps or balls in a mixture

The amount of fibres introduced into the mixture (or fibre volumetric fraction), also plays a vital role in the overall material behaviour. Toughness (total area under the load-deflection response) increases with a higher fibre volume dosage. Figure 2.2 shows that the addition of fibres to plain concrete greatly increases the toughness of the material. Fibre dosage typically ranges from 0.1 to 3%; fibre content in excess of 3% may also result in poor workability (Chanh, 1999).

Moreover, increased volume fraction of steel fibres in concrete improves and increases the energy absorption capacity leading to enhanced post-peak ductility. The exact optimization of steel fibres needs to be performed to achieve the desired results and minimize the material costs.

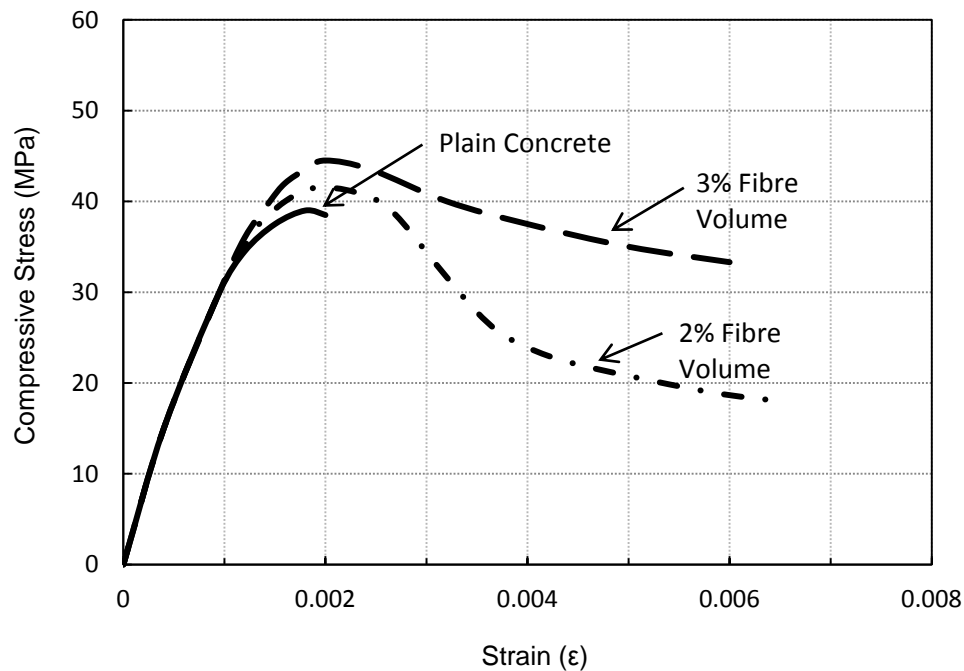


Figure 2.2 - Toughness of SFRC with varying fibre volume (Chanh, 1999)

Furthermore, quality control employed during casting is a critical component in achieving the desired material properties. Even with an ideally designed concrete mixture, the structure's overall performance can prove to be inadequate without the presence of proper quality control.

One of the main obstacles in obtaining a uniformly distributed fibre matrix is avoiding the balling phenomenon. Balling may be attributed to a number of factors:

- i. The fibres may already be clumped together before being added to the concrete mixture. They should be passed through a screen, as normal mixing action will separate these clumps.
- ii. The addition of fibres may be too quick, preventing them from dispersing in the mixer.
- iii. The volume of fibres added may be too high for the corresponding aspect ratio.
- iv. The mixing equipment may be damaged, or inefficient in dispersing the fibres.
- v. The introduction of fibres to the mixture before all other concrete constituents are added may cause balling.

Due to these potential complications, great care must be taken during the mixing phase (Chanh, 1999).

Another barrier commonly encountered while casting fresh SFRC is the influence of the pouring and compacting process on the distribution and orientation of fibres. Typically, fibres are distributed evenly in all directions throughout the concrete matrix. However, in the casting process of tunnel lining segments, the concrete flows from the middle of the formwork down to the edges due to the formwork's downward curvature (De Waal, 1999). As a result, the fibre percentage experiences a gravity effect and tends to be denser near the intrados of the segment. This effect actually provides higher tensile resistance when the intrados section is subjected to tension; however it has the inverse effect when the extrados region is subject to tension. Figure 2.3 illustrates this effect.

Researchers (eg. Edgington *et al.*, 1972; Stroeven *et al.*, 1977; Stroeven *et al.*, 1979; Soroushian *et al.*, 1990; Toutanji *et al.*, 1998) have also concluded that external vibrations during the compaction process contribute to the segregation and overall orientation of fibres. The use of an internal vibrator for compaction of the concrete can disturb the orientation of the fibres locally if applied for an extended duration. Additionally, the application of an external vibrator tends to orient the fibres perpendicular to the direction of the vibration (De Waal, 1999). As a result of this inhomogeneous orientation of the fibres, the material properties may not be the same in every direction and may vary at different locations of the structure. Hence great care must be taken during the casting process to ensure even distribution and isotropic orientation of fibres (Gettu *et al.*, 2004).

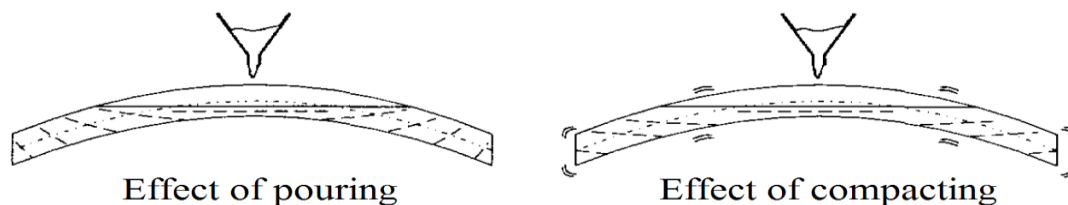


Figure 2.3 - Effect of segment production on the fibre orientation (De Waal, 1999)

2.2.2 Steel Fibre Reinforced Concrete Stress Block Diagrams

In the design of the concrete elements, the location and magnitude of the compressive and tensile stresses acting on the element is of great importance. Simplified stress blocks have proven to be an excellent tool in achieving this. Figure 2.5 shows the typical stresses acting on a steel fibre reinforced concrete beam with respect to four main cracking phases.

In phase 1, the stress-displacement relationship can be idealised as linear elastic. There is no crack in the tensile zone (T1) and the maximum tensile stress is reached at strain ϵ_{MS} . In this phase, the fibre geometry usually has no influence on the load capacity, hence the maximum tensile stresses are only related to the concrete strength and fibre ratio (Banthia, 2001).

In phase 2, cracking is initiated in the concrete resulting in a loss of strength in the fracture zone (FZ). Once the crack starts opening (around 0.1 to 0.2 mm), the fibres with long embedment lengths are still capable of carrying extra load, but shorter fibres begin to pull-out. By the end of phase 2, the crack is well established and most fibres have exceeded their peak loads and begin to slip from the concrete matrix (Banthia, 2001). With respect to the stress block, the deflection behaviour of the prism changes from elastic to more or less elasto-plastic, with a hinge developing in the mid-span.

Phase 3 initiates when the main concrete crack has formed and the fibres resisting the opening are doing so primarily through fibre-pullout. Naturally, not all fibres that cross the crack provide resistance, since many are not sufficiently anchored. As the crack width increases, the neutral axis moves upward towards the compression zone.

Eventually, with increasing crack opening, most fibres will pull-out with no residual force and that brings phase 3 to an end.

During phase 4, the concrete near the notch carries no tensile stress, but the load is carried by the part of the section in which the fibres are still engaged and the neutral axis depth moves closer to the compressive zone.

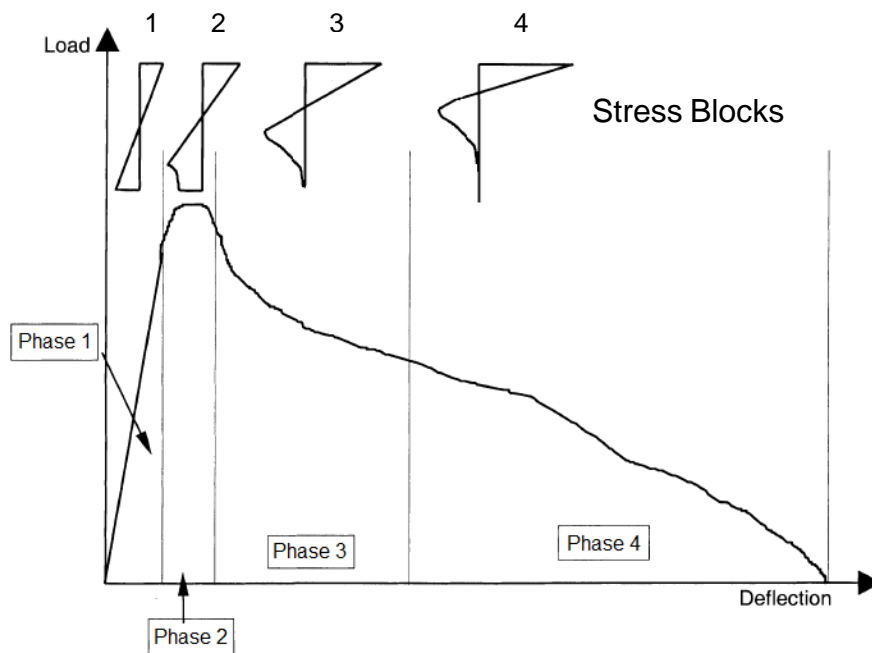


Figure 2.4 - Load-deflection curve of different cracking phases of steel fibre reinforced concrete beam (Tlemat *et al.*, 2006)

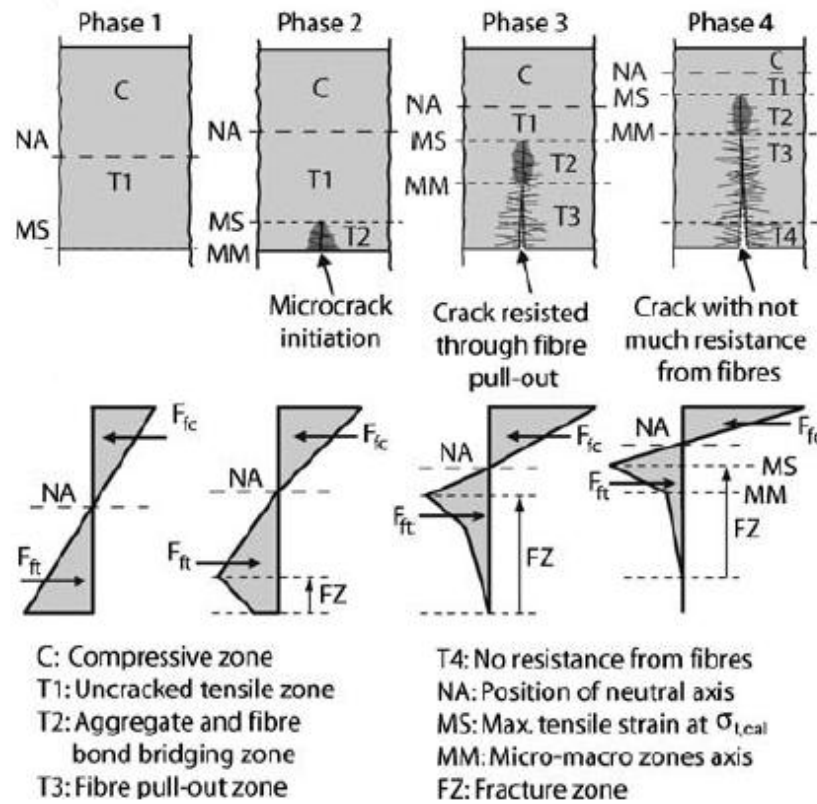


Figure 2.5 - Schematic representation of a steel fibre reinforced concrete beam under flexural loading (Tlemat *et al.*, 2006)

2.2.3 Comparison of SFRC and Reinforced Concrete

It is well known that plain concrete has a low tensile strength and strain capacity at fracture (Chanh, 1999). This deficiency is traditionally overcome by including reinforcing bars or pre-stressed steel members. The design of conventional reinforced segmented tunnel linings is successful in providing the required tensile resistance, however it possesses certain limitations. The complex geometric shape results in difficult assembly of the rebar cage as shown in Figure 2.6. Mass production of tunnel lining segments typically requires an additional fabrication unit to accommodate the assembly of these rebar cages, consequently increasing manufacturing, labour and material costs.

A study performed in an effort to compare the cost saving benefits of replacing current forms of concrete with SFRC, concluded that approximately 25% cost saving benefits are achievable with respect to material costs alone (Venkatesh *et al.*, 2006). The addition of labour intensive rebar fabrication and installation in the forms may also result in a schedule impact, increasing the costs further.



Figure 2.6 - Typical tunnel lining rebar cage assembly

For certain concrete applications, conventional rebar proves to be a more suitable alternative. However, in specific loading conditions, SFRC has the ability to perform better and can completely replace conventionally reinforced concrete (Burgers, 2006; Moccichino et al., 2006). Moreover, in the case of tunnel linings, the internal forces are mainly a combination of bending moments and hoop forces, which make SFRC an ideal substitute. Steel fibres not only increase the structural capacity of concrete, but also improve long term durability issues. Additionally, steel fibres can be introduced directly into the concrete batch during the mixing stage. This greatly improves the production time, removes the necessary quality control inspection of steel rebars and provides large cost saving benefits.

In comparison to conventional reinforced concrete, SFRC has superior resistance to cracking and crack propagation. Unlike reinforcing rebars, which are located in a single plane, steel fibres are distributed throughout the concrete mixture. The fibres are able to hold the structure's matrix together, even after extensive cracking, providing a high resistance against spalling (e.g. Chanh, 1999; Machimo *et al.*, 2002; Moccichino *et al.*, 2006). The main purpose of steel fibres is to regulate micro and macro cracking. They restrict the formation and propagation of cracks at their origin. Furthermore, the enhanced durability properties of SFRC limit the onset of corrosion. Since the fibres are dispersed, the absence of contact between them does not allow the initiation of corrosive current, leading to formation of corrosion products. Moreover, the fire protection performance of concrete is also increased with the use of steel fibres, by limiting the cracking and spalling (Chen *et al.*, 2004). Considering all these beneficial properties, SFRC proves to be a suitable material for use in precast tunnel lining segments.

2.3 Tunnelling

Tunneling has been a form of creating underground infrastructure for thousands of years. Throughout this period, there have been many advancements in technology improving the safety, efficiency and overall productivity of tunneling systems.

Many different applications of tunnels exist, serving different purposes. The most common form, transportation tunnels (i.e. roadway, subway, and pedestrian) offer a more convenient means of access from one location to another or in some cases to locations not previously accessible. Other applications of tunneling are pressure tunnels, which are a crucial component in the operation of hydroelectric power plants. Their purpose is to divert water from an upstream reservoir to a hydro-electric power house, carrying very large outward pressures. Micro tunnels are also employed in the routing of telecommunication cables.

Tunneling operations consist of the excavation of soil/rock which results in increased in-situ stresses due to the loosened native soil. As such, additional reinforcement is employed in areas of low in-situ strength, or where cover is inadequate. Reinforcing the tunnel walls are often done with rock bolts, wire mesh, and concrete lining, depending on the in-situ condition present (i.e. soil/rock type, stress state, water table location). In the application of pressure tunnels, steel linings grouted with concrete may be used. Figure 2.7 illustrates the basic different types of linings; the lined section, the semi-lined section, and the unlined section.

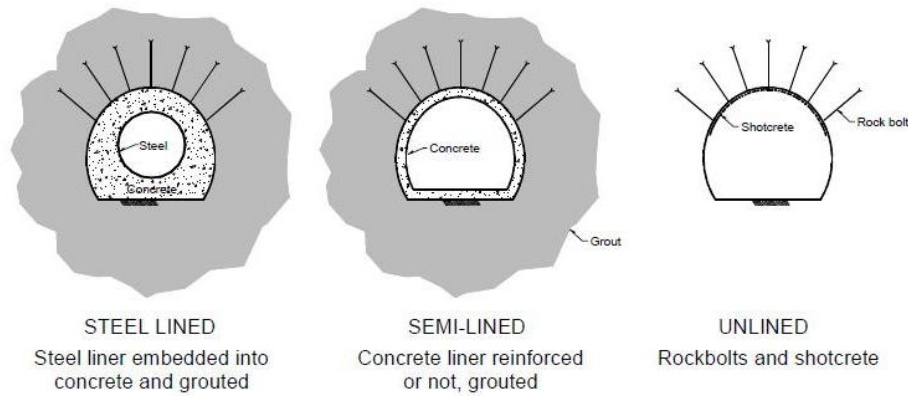


Figure 2.7 - Tunnel lining reinforcement sections (Rancourt *et al.*, 2007)

Several different methods of tunneling are used depending on the characteristics of the tunnel being built (i.e. depth, length and location). The process of drilling and blasting (D&B) revolutionised tunneling technology and continues to be the most common form of tunneling to date. As the name suggests, the process of D&B consists of drilling a number of holes at the tunnel face, filling them with explosives and detonating the explosives causing the rock to collapse. The rubble is removed and the exposed surface is reinforced appropriately. This process is repeated, until the tunnel is constructed.

Cut-and-cover tunneling is often employed in shallow tunnels, such as those commonly used in subway, railway and metro systems. The process involves excavating a trench the length of the tunnel, constructing the tunnel inside it, carefully back-filling the trench and reinstating the surface.

The tunnel boring machine is an increasingly common method of tunneling and is described in the following section.

2.3.1 Tunnel Boring

A tunnel boring machine (TBM) is a circular cross-section machine used to excavate tunnels through a variety of soils and rock strata. In unstable ground conditions, concrete segments are erected in place forming a lining as the TBM advances. The tunnel lining contributes greatly towards the serviceability, increased mechanical and ultimate capacity of the excavated area and reduces uncertainties during and after construction by increasing the factor of safety (Mashimo *et al.*, 2002). The TBM has advantages of limiting disturbances to the surrounding ground, which is crucial when tunnelling in soft unstable soils. It is also favorable when tunneling in residential areas, where drill and blast techniques may cause disturbances to the local population. Furthermore, by producing a smooth tunnel wall, the cost of lining the tunnel is highly reduced. The main disadvantage of using a TBM as a method of tunneling is the large overhead costs due to the complexity of this machinery. However, as modern tunnels become longer, TBMs actually prove to be a more economical solution compared to D&B due to their efficiency and resulting shorter project time frame.

The double shield TBM is nowadays the most commonly used machine for highly sophisticated operations and is suitable for a variety geological conditions. It consists of a front shield, telescopic gripper shield, and has the ability to operate in the following two modes:

- i) In stable ground, gripper pads are propped against the side wall of the tunnel to provide forward thrust capabilities and allow for segment installation to occur simultaneously during excavations.

- ii) In fractured ground, the thrust is shifted to thrust cylinders that push off the concrete tunnel segments behind the machine. This prevents damage to fragile tunnel walls, which could induce large disturbances. In this process however, excavation and segment installation are performed independently and thus tunnel productivity is diminished.

The TBM has revolutionized the tunnelling industry by making tunnelling safer, a more economical solution for creating underground space and by opening the possibility of creating tunnels where it was not feasible before (Spencer *et al.*, 2009). Figure 2.8 demonstrates a typical TBM.



Figure 2.8 - Tunnel Boring Machine

2.3.2 Steel Fibre Reinforced Concrete Tunnel Lining

SFRC is nowadays extensively used in civil infrastructure due to its enhanced mechanical and durability performance. It has been successfully employed in various applications including rock slope stabilization, footings, offshore structures, slabs on grade, hydraulic structures, architectural panels, precast segments and shotcrete technology (Banthia, 2001)

The application of SFRC in the construction of tunnel lining segments (TLS) has been predominantly applied in Europe, Australia, and the UAE beginning in the early 1990's (Hansel *et al.*, 2011). Typical tunnel inner diameters range from 2.8 – 9.2 m in diameter, having lining thicknesses of 150 – 400 mm thick. Table 2.1 provides a list of major tunnel projects utilizing SFRC as a primary material in the fabrication of concrete tunnel linings. To date, Canada has no history of SFRC use as a material in tunnel lining applications.

In 2008, the municipality of Toronto, Ontario initiated a preliminary investigation to evaluate the novel properties of SFRC for the tunnelling industry. A 150 m long test section of the new 8.6 km long Toronto York Spadina Subway Extension is planned to consist of solely steel fibre reinforced concrete tunnel lining. This will be the first employment of this innovative material in Canada.

Tunnel	Country (Year of Construction)	Inner Diameter (m)	Lining Thickness (mm)	Length (km)	Number of Segments per Ring
Channel Tunnel Rail	Britain & France (1994)	7.5	350	37.9	9 + key
Oenzberg Tunnel	Switzerland (2004)	12.3	480	3.16	-----
Hofoldingen Stollen	Germany (2004)	3.3	180	17.5	6
Wehrhahn Line	Germany (2014)	9.2	450	3.40	7 + key
Step Tunnel	Abu Dhabi (2018)	6.3	280	42.0	-----
Copenhagen	Denmark (2009)	4.2	300	3.90	5 + key
2nd Heinenoord	Netherlands (1999)	7.6	350	1.35	7 + key
Gold Coast	Australia (2009)	2.8	150	2.00	6
Fanaco	Italy	3.0	200	4.82	-----
Metrosud	Italy	5.8	300	2.64	-----
Heathrow	U.K. (1995)	4.5	150	1.40	-----
Jubilee	U.K. (1996)	4.4	200	2.40	-----
Essen	Germany	7.3	400	1.20	-----
Lotschberg	Switzerland	4.5	220	1.10	-----

Table 2.1 - History of steel fibre reinforced concrete tunnels (Hansel *et al.*, 2011)

2.3.3 In-situ Shotcrete Tunnel Linings

Shotcrete is a form of sprayed concrete typically used in the repair of existing structures, or as preliminary/permanent structural support. Concrete is pneumatically projected through a hose onto a surface at high velocity, where it is compacted on impact. It is commonly used when formwork is costly, impractical or access to the working area is limited. In the case of tunnel linings, the area is first excavated and then lined with shotcrete. The shotcrete serves as structural support to the unreinforced surroundings. Shotcrete linings between 100 – 150 mm thick begin to act as rock stabilizer, and linings with thickness more than 250 mm can be designed using the same approaches as used for precast concrete linings (Brekke *et al.*, 1987). The main disadvantage of shotcrete is the lack of achieved quality control. Since this technique is performed in the field, under difficult conditions, material defects are more likely to occur.

2.3.4 Precast Segment Tunnel Linings

Precast concrete tunnel liners are produced by casting concrete in reusable molds, allowing them to cure in a controlled environment. The casting beds for precast operations can be used repeatedly with small maintenance (if needed), which makes the cost of formwork/unit lower than on site production. Once fully cured, the segments can be stacked in a storage yard until ready for transportation to the construction site. During excavation, they are simultaneously assembled inside the shield of the TBM to form a ring. Unlike shotcrete, or cast in place liners, precast segments have the benefit of being jointed; ultimately lowering the overall stiffness of the structure. Thus, the tunnel absorbs external forces by deforming, and hence is subjected to lower moments (El Naggar, *et al.*, 2008).

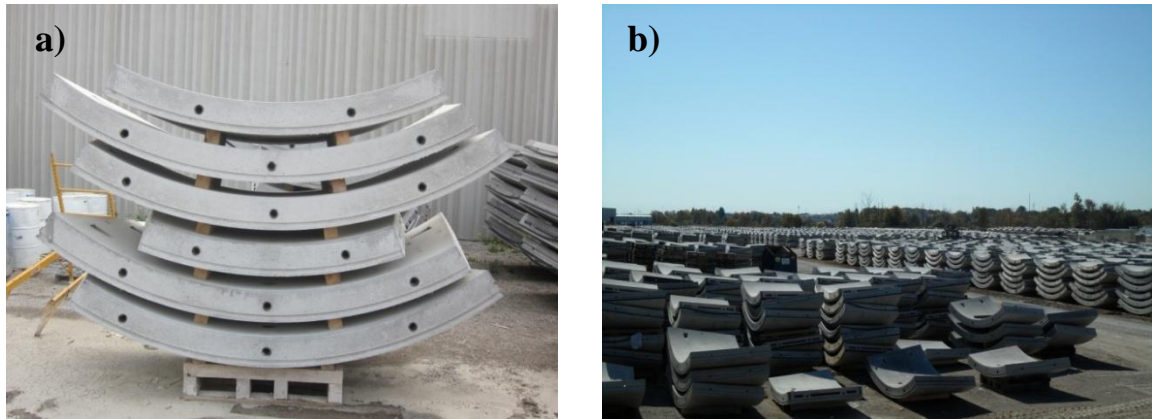


Figure 2.9 - Precast segment linings (a) a stacked full tunnel ring, (b) storage yard

The main disadvantage of precast concrete tunnel lining segments is the minimal allowable tolerance, which in turn requires very high quality control. If a tunnel segment is out of line by only a few millimetres, the joint alignment may be compromised and the lining may not be able to be properly assembled. As a result, it is crucial that a high level of quality control be present throughout the fabrication timeline of each segment. Mock-up tests are often performed, which involve assembling a small section (typically 2-3 rings) in a controlled environment to ensure high production quality. Figure 2.10 illustrates a mock-up test. Quality strength performance tests are also performed every few batches, as to ensure proper concrete mixing and minimal design strength requirements. Tensile and compressive tests are often done at time of casting, 28 days, 56 days, and before delivery to site, to ensure the segments meet design specifications.



Figure 2.10 - Tunnel ring assembly mock up



Figure 2.11 - Segmented tunnel liner casting bed

2.3.5 Forces Acting on Tunnel Linings

Prior to doing full scale testing or finite element modeling, it is crucial to first determine the type of loads acting on the tunnel lining system. The bending stresses present within the tunnel liner are a direct cause of the moments acting on the tunnel structure (Figure 2.12). Typically in isotropic ground conditions, the maximum moments are present at the springline of the tunnel. Moreover, the magnitude of these moments is also dependent on the stiffness of the liner. Jointed tunnels have a much lower stiffness in comparison to continuous liners because the in-situ stresses acting on the liner are absorbed by the ability of the joints to rotate (El Naggar *et al.*, 2008).

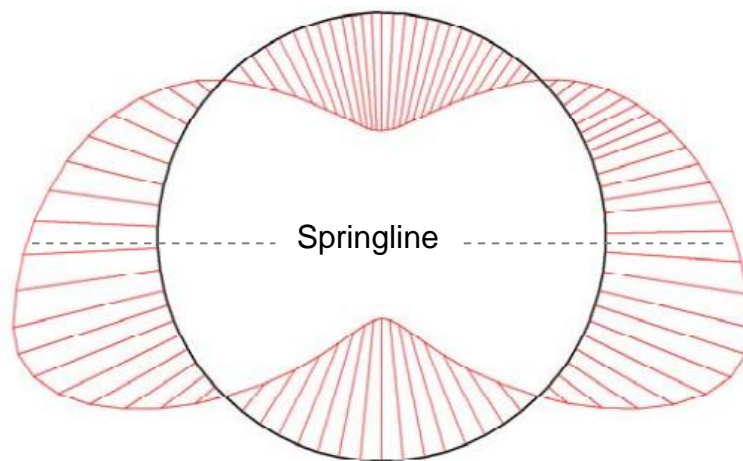


Figure 2.12 - Typical moments acting on a tunnel liner (Mashimo *et al.*, 2002)

Additionally, the tunnel liner may be subjected to higher stress states when weak soil conditions are present, or when ground supports fail. According to Mashimo *et al.*, (2002), there are three critical loading scenarios where the tunnel liner may experience larger than expected stresses:

- i) An increase in earth pressure due to loosened or weak soil at the tunnel crown, resulting mainly in an increase of axial forces
- ii) Loosened ground in conjunction with loss of support or confinement of the lining ring at the crown and shoulders causing bending moments at the tunnel shoulders.
- iii) Large uniform pressures acting on the lining due to very weak ground conditions resulting in a combination of axial and bending forces.

Moreover, a tunnel liner may be subject to higher bending stresses if care is not taken during installation. A tunnel is typically excavated with a slightly larger diameter than the outside diameter of the tunnel ring. Post installation, a layer of concrete or grout is backfilled between the tunnel lining and soil wall to create an integrated supporting structure. When inadequate grout filling between the structure and soil surface is present, the tunnel lining is consequently subjected to flexural stresses, as illustrated in Figure 2.13.

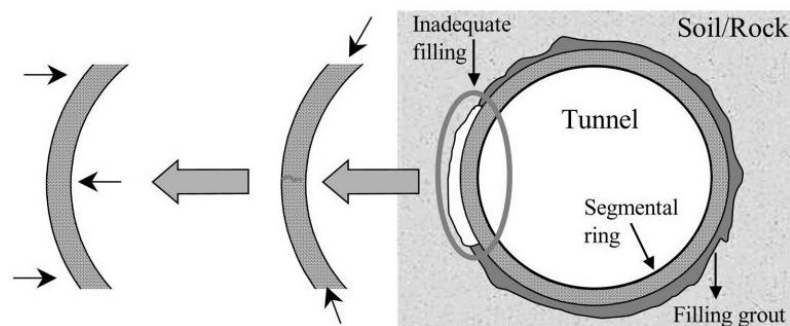


Figure 2.13 - Bending due to inadequate grout filling (Gettu *et. al.*, 2004)

Furthermore, after the casting and curing phase, segments are set down and stacked on supports. Timber blocks are usually placed between segments taking care that they are aligned with the supports. It is possible that eccentric placing of segments due to differences in the location of supporting blocks between segment layers, may results in additional bending moments. Such additional forces can lead to unplanned cracks or deformations, particularly in long segments used in big diameter tunnels. The loading effects due to storage of the segments can be calculated according to the formulas shown in Figure 2.14, where M = the maximum moment at the centre of the beam ($\text{kN}\cdot\text{m}$), w = width of the segment (m), d = depth of the segment (m), L = length of the segment (m), and γ = specific weight of concrete (kN/m^3).

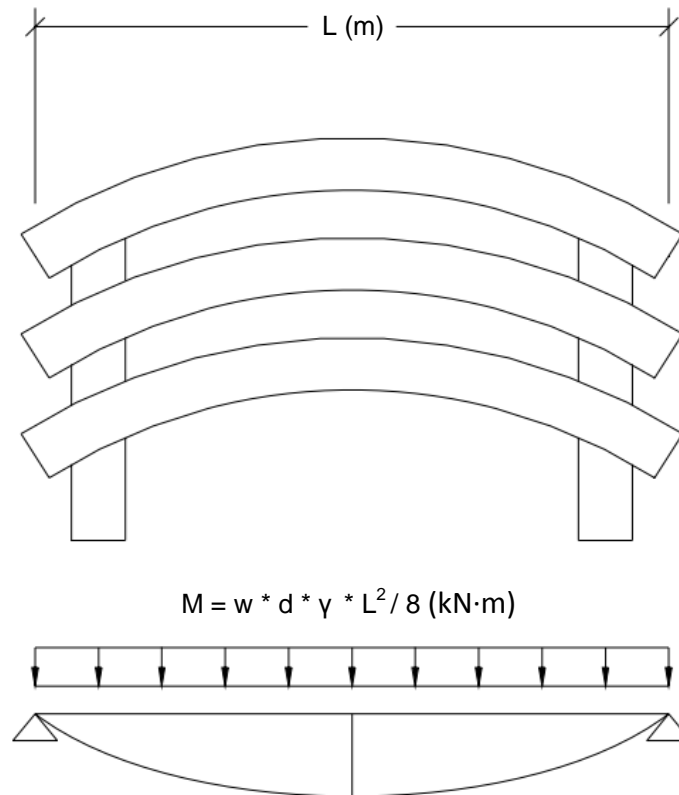


Figure 2.14 - Moment loads acting on stored segments

2.4 Previous Structural Testing

2.4.1 Full Scale Testing

2.4.1.1 Moccichino *et al.* (2006)

Full-scale bending tests were performed on tunnel segment specimens, to compare the flexural performance of SFRC elements with respect to the conventionally reinforced ones. The tunnel segments analyzed were modelled after the Brenner Base Tunnel, located between Italy and Austria, which were designed for the application of mechanized tunnelling with a TBM double shield machine. The segments considered in the study had a thickness of 200 mm, a width of 1500 mm, a length of 3640 mm and a compressive strength of 75 MPa. A line load was applied through a load distribution frame using an electromechanical actuator with a maximum load of 1000 kN. Vertical displacements were measured by using three linear variable displacement transducers (LVDTs) placed at the intrados midspan of the segment. The crack openings were recorded with two LVDTs located at the central intrados of the segment. Finally, the applied load was measured using a load cell placed between the frame and the segment. The test setup is shown in Figure 2.15.

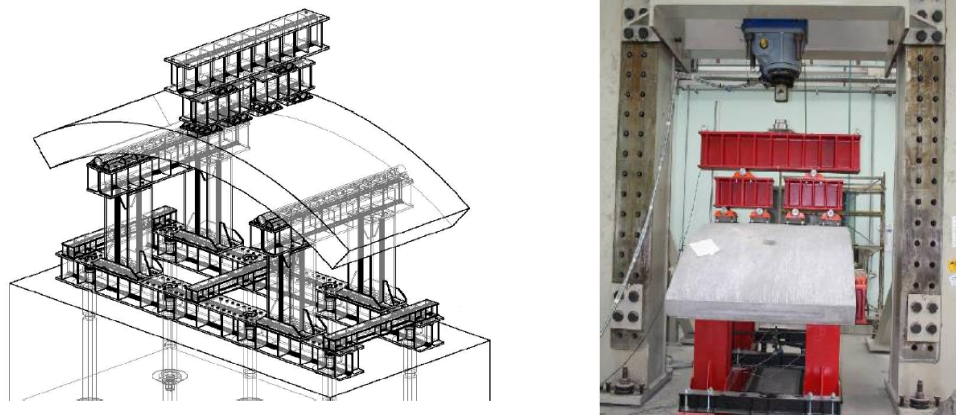


Figure 2.15 - Schematic diagram of the flexure test (Moccichino *et al.*, 2006)

Figure 2.16 and Figure 2.17 show the load against displacement and load against crack width relationship, respectively. For a traditional reinforced concrete segment, it can be seen that the first cracking develops at an applied load of 70 kN, while the segment yields at 125 kN. Eventually strain hardening occurs up to a failure load of 175 kN.

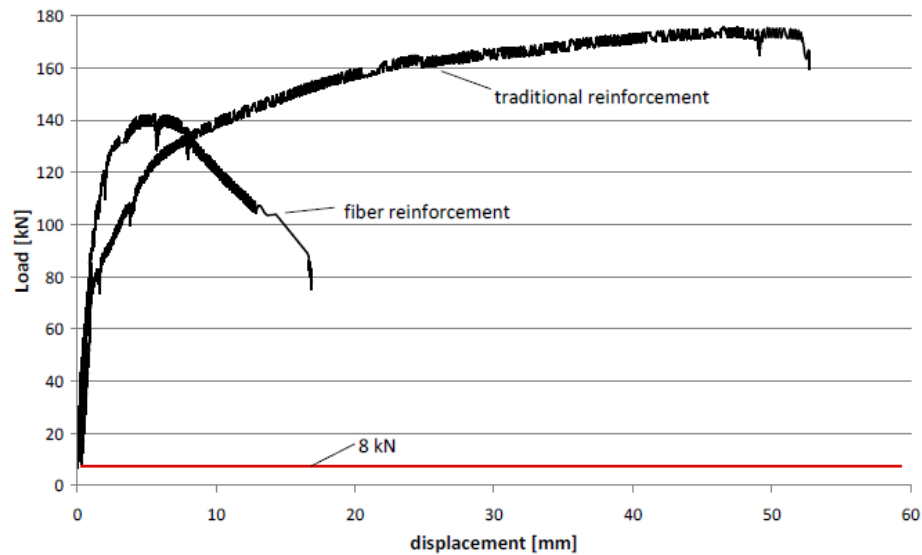


Figure 2.16 - Flexural test: load vs. midspan displacement (Moccichino *et al.*, 2006)

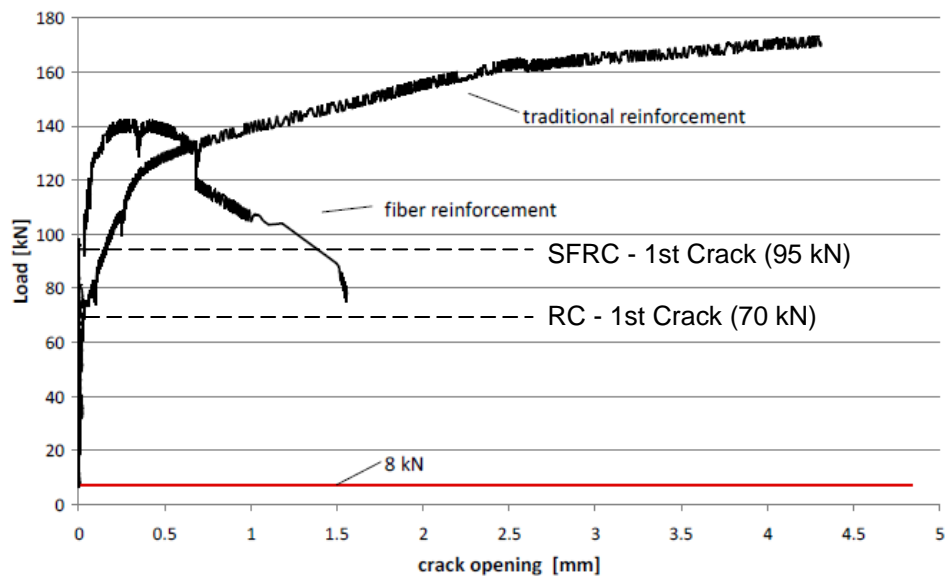


Figure 2.17 - Flexural test: load vs. crack width (Moccichino *et al.*, 2006)

The response of the SFRC segments is somewhat different. The segment experiences a higher initial stiffness with the first crack being detected at an applied load of 95 kN. Following this stage, the stiffness remains nearly constant up to a carrying load of 120 kN due to the stress being transmitted along the cracks by the fibre reinforcement. The segment reached a failure load at 140 kN, after which strain softening developed.

Although the flexural capacity of the RC segment was higher in comparison to the SFRC, some considerations have to be taken into account for the particular case of this structure. For precast tunnel segments, the structure is typically subjected to higher stresses during the construction phase rather than the service stage. Therefore, it is prudent to limit concrete cracking, during the curing and assembly steps. With respect to tunnel linings, the onset of cracking can represent an alternative ultimate state (Moccichino *et al.*, 2006). The main finding in this study was that SFRC can be substituted for traditional reinforcement; in particular the segment performance is improved by the fibre presence mainly in terms of crack opening control.

2.4.1.2 Poh *et al.* (2009)

Several full scale laboratory tests were performed to explore the potential of using SFRC in a mass rapid transit tunnel. The flexural tests were specified to investigate the load carrying capacity of conventional plain concrete and SFRC tunnel lining segments. The segments had a length, width, height, and thickness of 2359 mm, 1400 mm, 600 mm, and 350 mm, respectively. Each segment was supported by a roller system on one end and a horizontally restrained roller on the other end. Incremental loads of 10 kN were applied to a force distributing beam at midspan of the segment. The deflections were measured at midspan with the use of dial gauges and cracking was visually observed throughout the loading sequence. The test setup is shown in Figure 2.18.

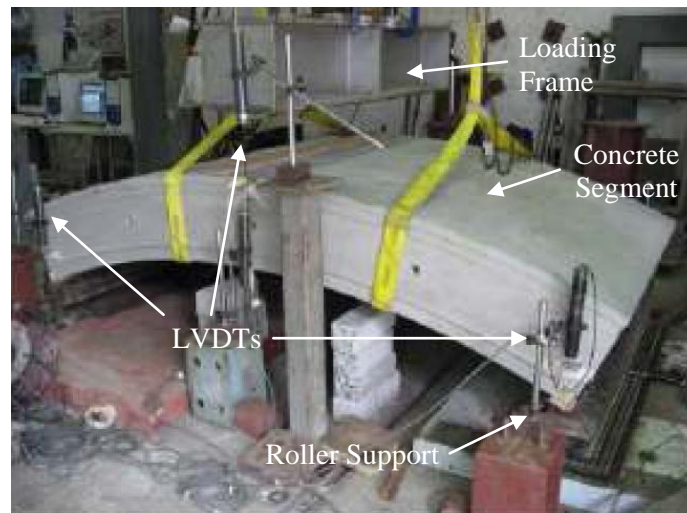


Figure 2.18 - Flexural test set-up and instrumentation (Poh *et al.*, 2009)

The test program comprised of three specimens for both conventional plain concrete and SFRC (30 kg/m³ and 40 kg/m³ of steel fibre). The experimental results for the plain concrete segments showed an initial elastic behaviour up to an applied load of 130 kN. The segment failed abruptly in a brittle manner at the peak load without showing any

characteristics of residual strength. Figure 2.19 shows the load-deflection behaviour of the plain concrete. The SFRC segments on the other hand exhibited a higher initial cracking load as the steel fibres began to provide a bridging effect in between the cracks. The failing load of the SFRC segments was 85% and 92% of the initially developed cracking load for segments having steel fibre 30 kg/m^3 and 40 kg/m^3 , respectively.

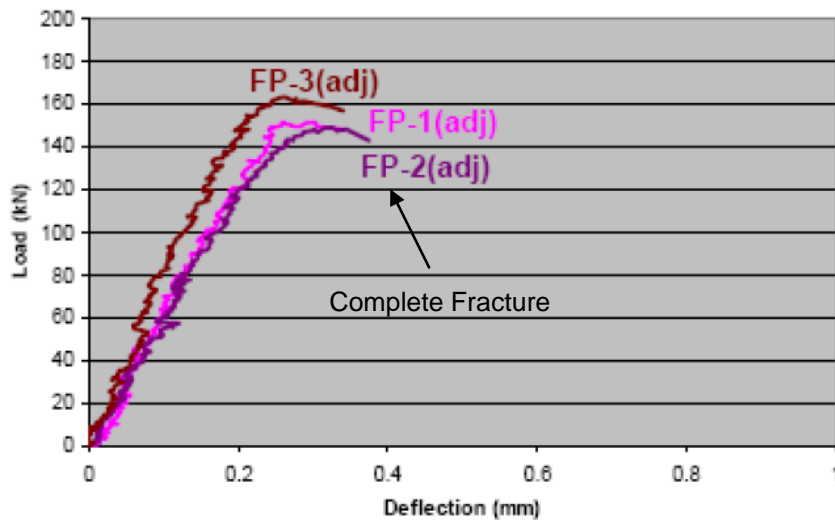


Figure 2.19 - Plain concrete flexure test: load-midspan displacement (Poh *et al.*, 2009)

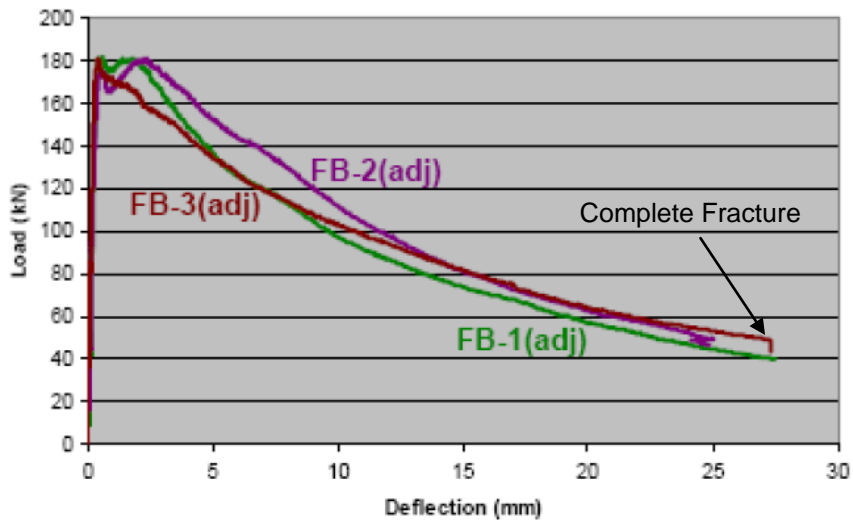


Figure 2.20 - SFRC flexure test: load- midspan displacement (Poh *et al.*, 2009)

2.4.1.3 Mashimo *et al.* (2002)

Mashimo *et al.*, (2002) carried out experimental tests to determine the load carrying capacity of tunnel linings. Three different loading arrangements were used, intended to simulate different ground conditions. Full scale models of both unreinforced and steel fibre reinforced segments were studied. The concrete specimens whose shape was a semi-circle, had diameter, width and thickness of 9700 mm, 1000 mm, and 300 mm, respectively. In the case of SFRC, the lengths of fibre used were 50 mm and 60 mm and the mixture ratio was 0.5 %.

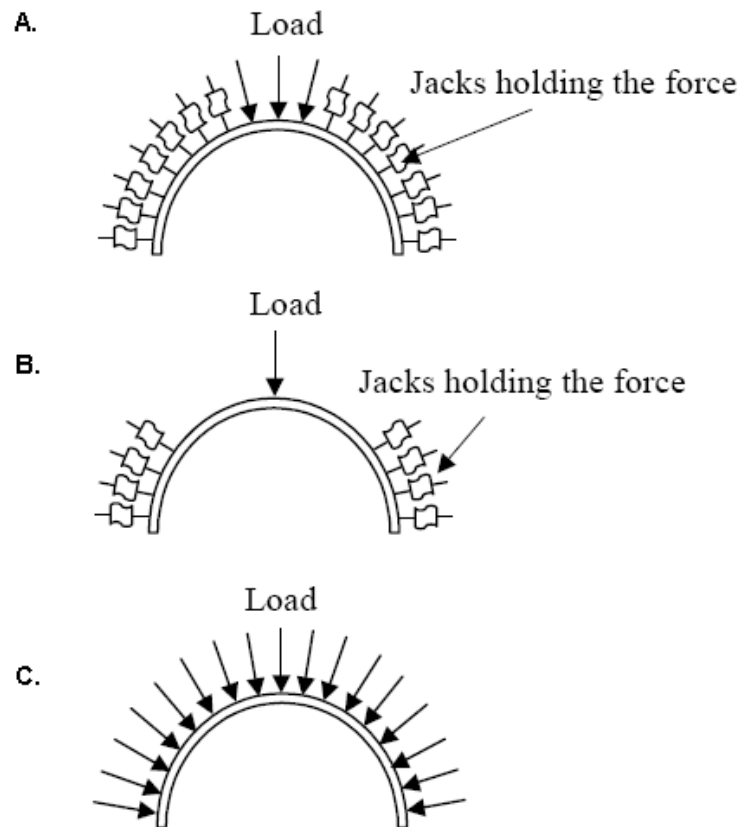


Figure 2.21 - Various loadings simulating different ground conditions (Mashimo *et al.*, 2002)

Three different loading arrangements shown in Figure 2.21 were considered to observe the influence of axial load only, bending load and the combined action of axial and bending loads. These are depicted by loading scenario (A), (B), and (C), respectively. Loading case (A) was designed to simulate the increase in earth pressure at the tunnel crown due to loosened or weak soil. Loading case (B) was an attempt to examine the effects of concentrated loads at the tunnel crown due to loss of support of the lining ring at the crown and shoulders. Finally, loading case (C) represents a tunnel subjected to large uniform pressures acting on the lining, due to very weak ground conditions (Mashimo *et al.*, 2002). The supporting structure consisted of two jacks per section placed equally at a 300 mm distance from the top and bottom edges of the 1000 mm wide specimens. Loading plates were placed between the two jacks to adequately distribute the applied load and simulate realistic ground conditions.

For loading case (A), the unreinforced specimen experienced a failure load of 390 kN/jack, whereas the segment reinforced with steel fibres, withstood a maximum load of 330 kN/jack. The difference in the collapse load resulted from the difference in the compressive strength of each segment. The compressive strengths of the unreinforced and reinforced segments were 26 MPa and 20 MPa, respectively. Consequently, the results indicate that the load carrying capacity was dominated by the concrete compressive strength of the concrete and the effect of steel fibre-reinforcing had minimal effect.

Loading case (B) demonstrated a collapse load of 100 kN/jack for the unreinforced section, which had a compressive strength of 27 MPa. The fibre reinforced segments failed at loads of 115 kN/jack and 155 kN/jack with compressive strengths of 23.7 MPa and 28.3 MPa, respectively. Based on these load test results, it can be suggested that the addition of steel fibre reinforcement increases the load carrying capacity of the segments by 15% to 55%.

Lastly, the collapse load for case (C) was 250 kN/jack and 290 kN/jack for the unreinforced, and reinforced segments, respectively. The load carrying capacity increase of only 16% can be attributed to the reinforced segment having a lower compressive strength by 12.5%, as in case (A)

Mashimo *et al.*, (2002) observed that the most critical loading case overall was when the bending loads were dominant and that the addition of SFRC helped increase the load carrying capacity. Furthermore, it was concluded that the length and the type of fibre have an influence on the load carrying capacity. Fibres of smaller length have a slighter larger load carrying capacity. It was also found that the spalling of concrete from lining can be controlled by using fibre reinforced concrete.

2.4.1.4 Ahn (2011)

A comparison between structural behaviour of plain concrete and concrete equipped with a fire retardant thin spray-on liner (TSL) layer was performed. Several full-scale tests were conducted to study the load-carrying capacity of segmented tunnel linings subjected to a uniaxial loading and to investigate the effects of TSL on the load-carrying capacity, subject to the same loading. The segments considered in this study had a compressive strength of 40 MPa, an outer diameter of 5000 mm, a width of 610 mm and a thickness of 150 mm, and length of approximately 1800 mm. The test setup consisted of a hydraulic actuator, capable of generating a maximum load of 250 kN, supported by two vertical steel columns. The vertical load was applied to a 110 mm wide, 620 mm long and 25.4 mm thick steel loading plate which transferred the concentrated point load to a uniaxial line load acting on the segment extrados. Each segment was supported by a fixed connection on one end and a pin connection on the other. An LVDT was placed at the midspan of the segment in order to measure the load vs. displacement. Two LVDTs were also placed horizontally on the roller end of the segments to ensure uniform loading throughout the test. The experimental setup is shown in Figure 2.22.

Figure 2.23 compares the midspan load-displacement behaviour of the concrete segments with and without the TSL coating. The initial linear-elastic response of the uncoated segment and the TSL coated segments was similar up to a loading of approximately 50 kN. After this point, it can be seen that the TSL coated segments had slightly higher load capacity compared to the uncoated segment reaching a load of 68 kN. Post-peak, differences in the load carrying capacity of the uncoated and the TSL coated segments gradually decreased

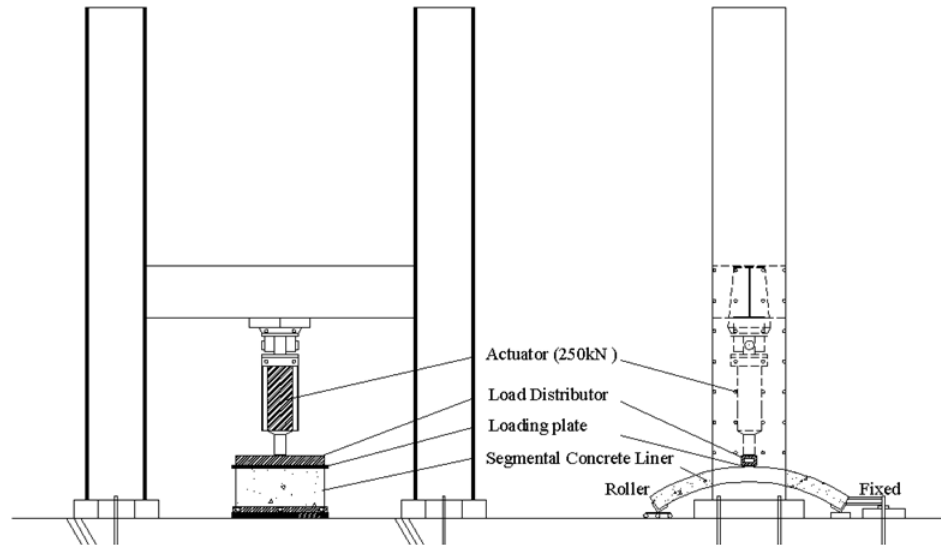


Figure 2.22 - Experimental setup (Ahn, 2011)

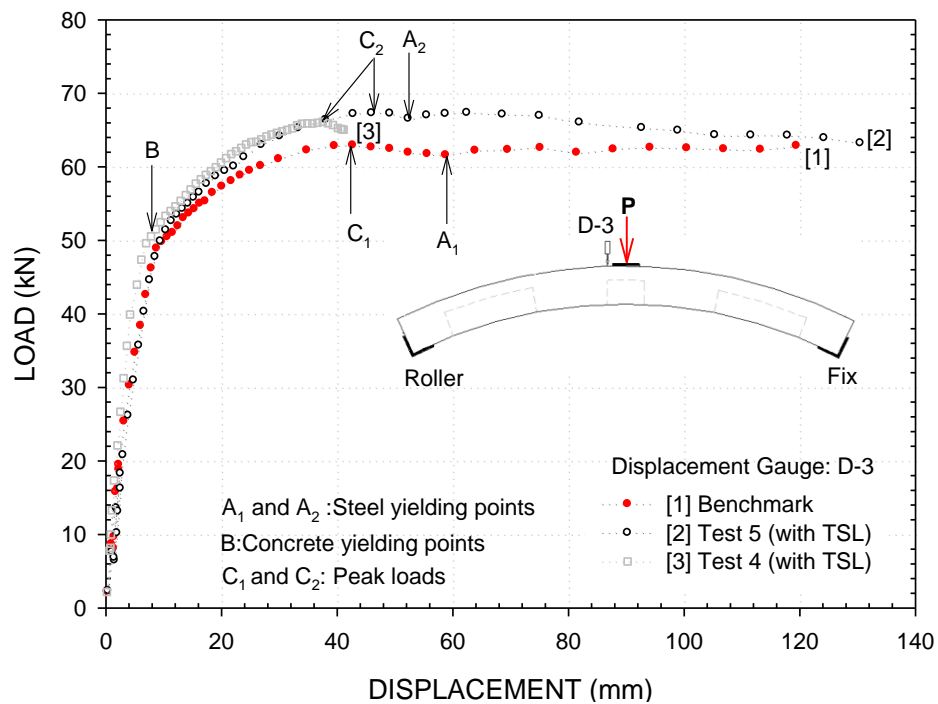


Figure 2.23 - Load-displacement comparison of plain and TSL covered tunnel lining segments subjected to flexural loading (Ahn, 2011)

2.4.2 Small Scale Testing

2.4.2.1 *Aruga et al., (2007)*

In an attempt to study the deformation and cracking of reinforced and unreinforced tunnel linings due to earth pressures, the Railway Technical Research Institute of Japan (RTRI) has performed several experimental tests to assess the structural performance of concrete tunnel linings.

Due to the high costs associated with full-scale testing, a 1/30 bench scale test was proposed as a scaled physical model system. The testing setup consisted of a semi-circular reaction frame, eleven radially spaced loading units and a pair of stoppers to prevent movement of the sidewalls. Loading cells were positioned at each of the loading units to record the reaction forces throughout the test. In addition, curved loading plates were placed between the load cells and the tunnel segment, to achieve adequate contact and to ensure uniform loading. Displacements were measured with seven displacement gauges which were positioned on the intrados of the test segment at angles of approximately 45° . Furthermore, strain gauges were spaced evenly along the intrados, and extrados of the lining model, which allowed for estimation of bending moments acting on the specimen, deduced from measured strain. Moreover, the segments tested had a width, thickness, and outer diameter of 20 mm, 10 mm, and 320 mm, respectively with a concrete compressive strength of 27 MPa. Figure 2.24 shows the testing setup.

The study focused on examining four cases of tunnel linings consisting of reinforced and plain concrete. In addition, segments having physical damage with 20 mm wide and 10 mm deep fragmented sections were also evaluated. According to the testing results from

Aruga *et al.*, (2007), the intact reinforced concrete lining and the plain concrete lining sustained very similar load carrying capacities in the initial loading stages prior to cracking. However, once tensile cracking and compressive crushing initiated in the plain concrete segment, its structural performance was greatly diminished in comparison to the reinforced section. The superior post-crack behaviour of the reinforced segment was attributed to the addition of steel reinforcement, which improved post peak strength characteristics of the concrete. In the case of the damaged concrete liners, both types of linings demonstrated a major decrease in the load carrying capacity after tensile cracking occurred. However, like the intact linings, the reinforced concrete segments displayed better post-failure behaviour, whereas the plain concrete liner failed in a brittle manner. From the test data presented, the post-cracking performance of the reinforced concrete liner was shown to be greater than that of the plain concrete. In addition, the durability of the reinforced concrete lining was substantially better.

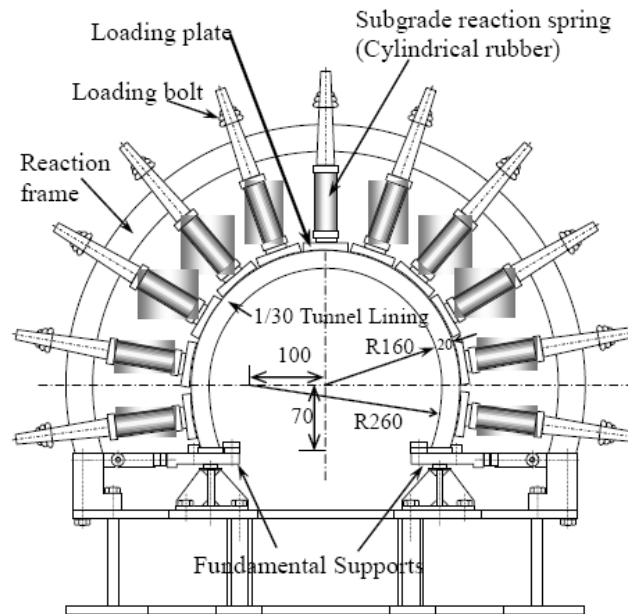


Figure 2.24 - A bench-scale model (1/30) test setup (Aruga *et al.*, 2007)

2.5 Numerical Modelling

2.5.1 Ahn (2011)

Ahn (2011) performed several experimental three point bending flexure tests on segmented tunnel linings to investigate their load-carrying capacities. A non-linear elasto-plastic finite element analysis was then performed in an attempt to simulate the experimental results. ABAQUS, a finite element package was used in the analysis.

ABAQUS provides two general concrete models which are capable of modeling plain and reinforced concrete; the concrete smeared cracking (CSC) model and the concrete damaged plastic (CDP) model. Both models were investigated and it was determined that the CSC model had issues converging before reaching ultimate failure, preventing the investigation of the post-peak behaviour of concrete. The CDP model captured the peak and part of the post-peak strain-softening behaviour and was hence chosen to be used in the study. Table 2.2 summarizes the material input parameters used in the CDP model for concrete and the elasto-plastic strain hardening model for the steel reinforcement.

Parameter	Material	
	Concrete	Rebar (C45 Steel)
Initial tangent elastic modulus (E)	27,800 MPa	210,000 MPa
Poisson's ratio (ν)	0.2	0.3
Density	2500 kg/m ³	8030 kg/m ³
Unconfined compressive strength(f_{cu})	40 MPa	-----
Initial Yield Stress (σ_y)	20 MPa	280 MPa
Tensile failure stress (σ_{tf})	3.3 MPa	800 MPa
Model Behaviour	CDP ³	EP-S ⁴

³Concrete Damaged Plasticity; ⁴Elastoplastic strain-hardening

Table 2.2 - ABAQUS material input parameters (Ahn, 2011)

The 3D finite element model was generated following the dimensions of the full size segmented liner and consisted of 12,599 10-noded tetrahedron elements. Boundary conditions were applied to the segment ends in order to simulate a fixed and roller support, with $U1 = U2 = U3 = 0$ and $U2 = 0$, respectively. The finite element model geometry of the segmented concrete liner is shown in Figure 2.25

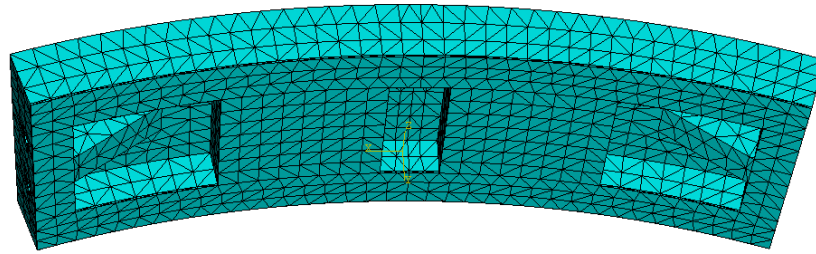


Figure 2.25 - Finite element geometry of the segmented concrete liner (Ahn, 2011)

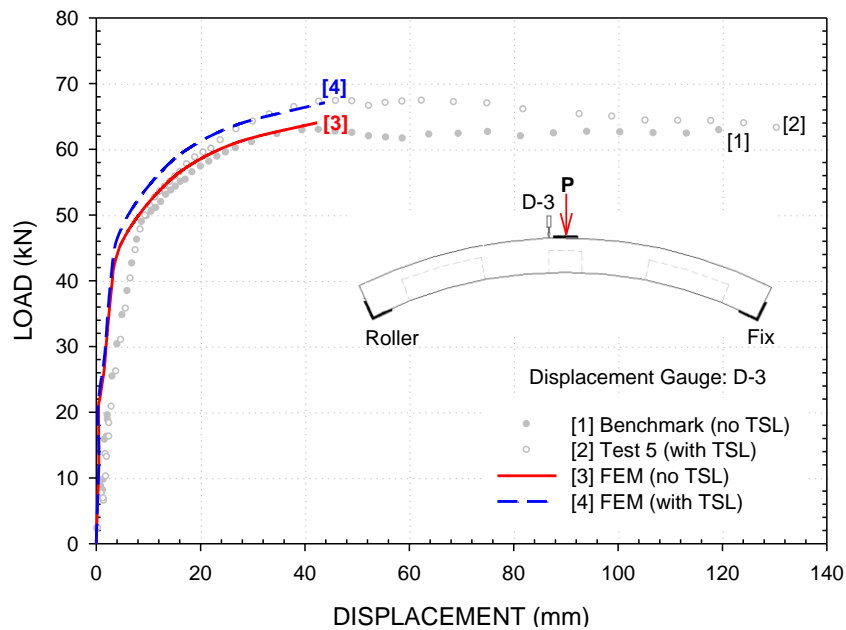


Figure 2.26 - A comparison between experimental and finite element results (Ahn, 2011)

Figure 2.26 illustrates a comparison of the load vs. midspan displacement between the experimental and numerical results. In the initial loading stage (up to 40 kN), the slope of the FE results was slightly steeper, signifying a higher stiffness. The results began to agree with each other once yielding of the material was reached. The slightly higher loading of the FE model could have been attributed to differences such as non-homogeneity and non-linearity in the material properties, inadequate function of the supports, and potential initiation of micro cracking in the concrete liners. Due to only minor differences in the flexural behaviour, it was concluded that a nonlinear FE analysis using Concrete Damaged Plastic (CDP) model in ABAQUS was very effective in predicting the displacement and the strain behaviour of segmented concrete tunnel lining subjects to uniaxial line loading.

2.5.2 Sorelli *et al.*, (2005)

A study was performed by Sorelli *et al.*, (2005) to investigate the possibilities of using SFRC tunnel lining segments as an alternative to conventional RC segments. Because the behaviour of both materials is fairly different, it was of interest to review and examine classical design methods in terms of post-cracking performance with experimental and numerical methods.

Three SFRC segments were cast in industrial conditions to capture realistic material variation caused by flow direction, gravitational forces, and compacting processes during the casting phase. To assess the level of heterogeneity of the SFRC segments, tensile tests were performed on 36 cylinder cores, drilled from the locations shown in Figure 2.27. Based on the post-cracking tensile tests performed on the cylinders, areas of the segment with higher concentrations of fibres were distinctly recognized. It was observed that specimens taken from areas belonging to “row 1” and “column C” exhibited higher residual strength, signifying a higher concentration of fibres. The flow direction of the fresh concrete pumped into the vertically standing moulds, resulted in the uneven fibre distribution.

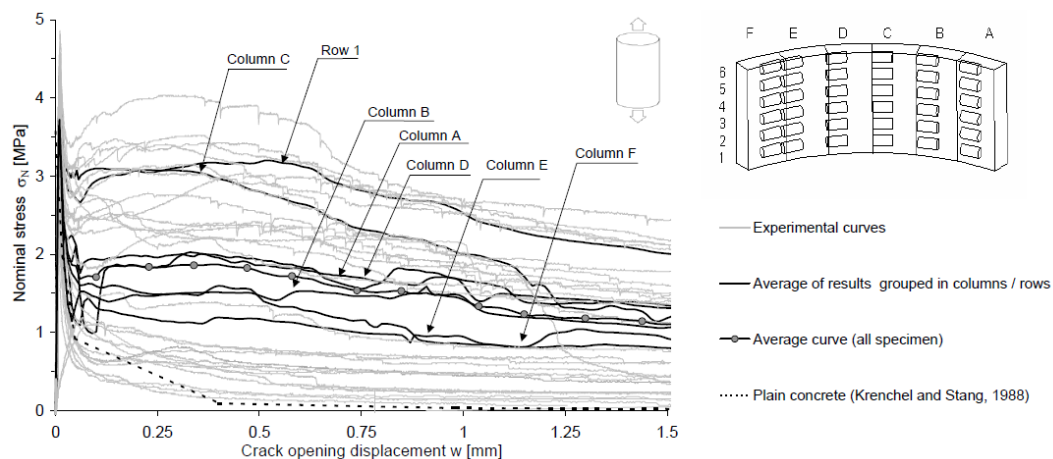


Figure 2.27 - Experimental tensile test response (Sorelli *et al.*, 2005)

The segments being modelled had an inner diameter, thickness and length of 6.3 m, 0.3 m, and 1.42 m, respectively. The configuration of the loading was based on the irregular fibre distribution and was considered the most critical arrangement. Two hydraulic jacks applied concentrated loads at the intrados corners, while the segment was restrained at the extrados midspan. The layout of the test setup is shown in Figure 2.28(a).

The finite element mesh was composed of 11,391 brick elements consisting of 14,000 nodes and utilized the Concrete Smeared Cracking model. The scatter of fibres with respect to the different locations of the segment was taken into account while generating the FE model. Zones with higher concentrations of fibres were prescribed different post-cracking tensile relations to optimize the accuracy of the analysis. A solid homogenous model was also reproduced and it was found that the fibre distribution had a significant effect on the global behaviour of the SFRC structure. Figure 2.28(b) illustrates a good agreement between the heterogeneous model and the experimental results and also highlights the behavioural deviation, when modelling a SFRC structure as a homogenous member. In addition, the CSC model used failed to converge just beyond the peak loading, preventing the investigation of the full post-peak behaviour.

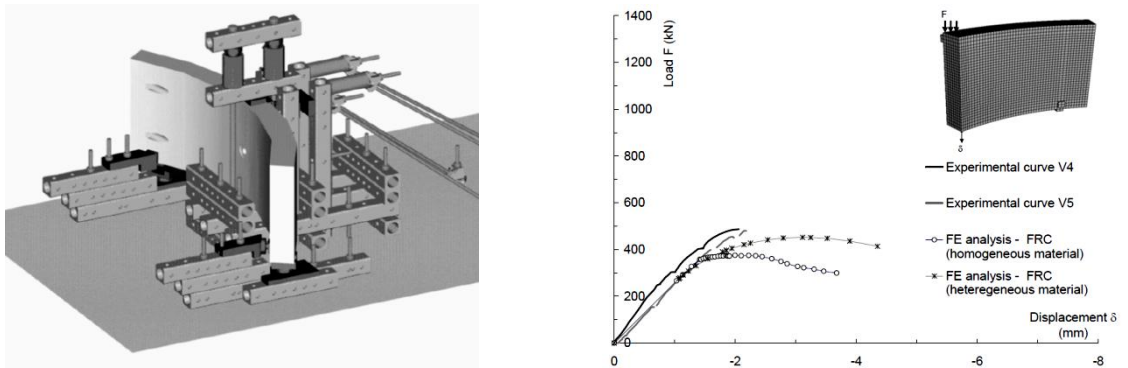


Figure 2.28 - (a) Test setup, (b) Experimental and finite element response (Sorelli *et al.*, 2005)

2.6 Summary

Over the last few decades, steel fibre reinforced concrete has become increasingly popular due to its enhanced mechanical properties and cost saving benefits, particularly in the application of tunnel support systems. Its physical and mechanical properties have been known to increase concrete toughness, and limit crack initiation and propagation preventing chemical seepage and in turn limiting spalling action. Additionally, benefits of replacing current forms of concrete with SFRC can result in approximately 25% cost saving benefits with respect to material costs alone, and greatly minimize production time (Venkatesh *et al.*, 2006). Furthermore, sophisticated tunnel boring machines have recently allowed for the excavation of native earth and installation of concrete segments to be installed simultaneously, resulting in quicker project delivery time. With the potential increase of steel fibre reinforced concrete in tunnel applications, more accurate analyses of tunnel liner behaviour are therefore of great interest.

Based on previous studies performed and reported in the literature, a uniaxial line load causing flexure has been found to represent one of the most critical loading cases for tunnel linings (Mashimo *et al.*, 2002) and proves to be a feasible method for evaluating the flexural response of full-scale segmented concrete tunnel linings in the laboratory. Superior flexural behaviour of a SFRC lining is primarily due to advantageous material properties (i.e. increased toughness, crack control), which are highly reliant on a uniformly distributed fibre matrix. Inadequate quality control employed during the casting process (e.g. the balling effect, excessive vibration, the gravity phenomenon) can lead to poor fibre distribution and orientation, consequently affecting the material's overall structural performance.

Furthermore, numerical attempts to replicate experimental flexure tests of tunnel segments using the Concrete Smeared Cracking model have only been successful in capturing the behaviour up to the peak loading. However, the Concrete Damage Plasticity model in finite element software has been shown to capture the post-peak ductility of reinforced concrete and is the most appropriate model for the analysis of steel fibre reinforced concrete tunnel liners.

METHODOLOGY

3.1 Introduction

In this chapter, the methodology and experimental testing procedures are presented. The design of the flexural test system comprising of a loading unit, loading frame, reaction frame and instrumentation is discussed. The experimental method was used to study the load-displacement, load-strain, and crack propagation behaviour of steel fibre reinforced concrete tunnel liner segments subjected to uniaxial flexure loading conditions. Moreover, several cores were drilled from random positions of two key segments, comprising of two separate concrete batches. Unconfined compressive and tensile tests, along with flexural beam tests were performed to determine the steel fibre reinforced concrete material properties. Analytical solutions of the compressive and tensile stress-strain behaviour are derived and compared to the experimental material testing to validate their approximations. Finally, non-destructive methods for evaluating the SFRC material and spatial characteristics by means of computed tomography scanning are examined.

The primary objectives of this chapter are: *(i)* to describe the method used in evaluating the flexural behaviour of steel fibre reinforced concrete tunnel liners, *(ii)* to determine and validate the compressive and tensile stress-strain characteristics of SFRC using experimental and analytical methods, *(iii)* investigate the concrete models in finite element software ABAQUS which are capable of analyzing the non-linear elasto-plastic behaviour of SFRC and *(iv)* to describe the non-destructive methods undertaken to study the fibre distribution using CT scanning.

3.2 Segment and Site Description

In 2008, the city of Toronto embarked on expanding its subway system between the City of Toronto and The Regional Municipality of York (see Figure 3.1). The 8.6 km long extension is planned to consist of approximately 6.6 km of underground tunnel to accommodate the Toronto York Spadina Subway Extension (TYSSE). A small 150 m test section comprising of 100 rings of SFRC segmented tunnel linings will also be included. This section will be subject to in-situ monitoring over the next decade to investigate its long term performance. The SFRC tunnel lining segments studied were designed by Hatch Mott MacDonald and fabricated by Armtex Pre-Con Manufacturing Ltd. in Woodstock, Ontario in Canada.

The tunnel lining consists of four segments and two key segments, which bolt together to form a ring. The rings are connected together with dowels in the longitudinal direction to form the tunnel lining. The internal diameter of the ring is 5400 mm, the lining thickness is 235 mm and the nominal width is 1500 mm. The segment specifications are summarized in Table 3.1. Figure 3.2 shows the segment geometry and dimensions.

The concrete mixture utilized Dramix 80/60 steel fibres conforming to ASTM A820-06 at a dosage density of 57 kg/m³ resulting in a 2% overall mixture per volume. The exact concrete mixture designed by Armtex Pre-Con remains confidential and is not disclosed in this thesis.

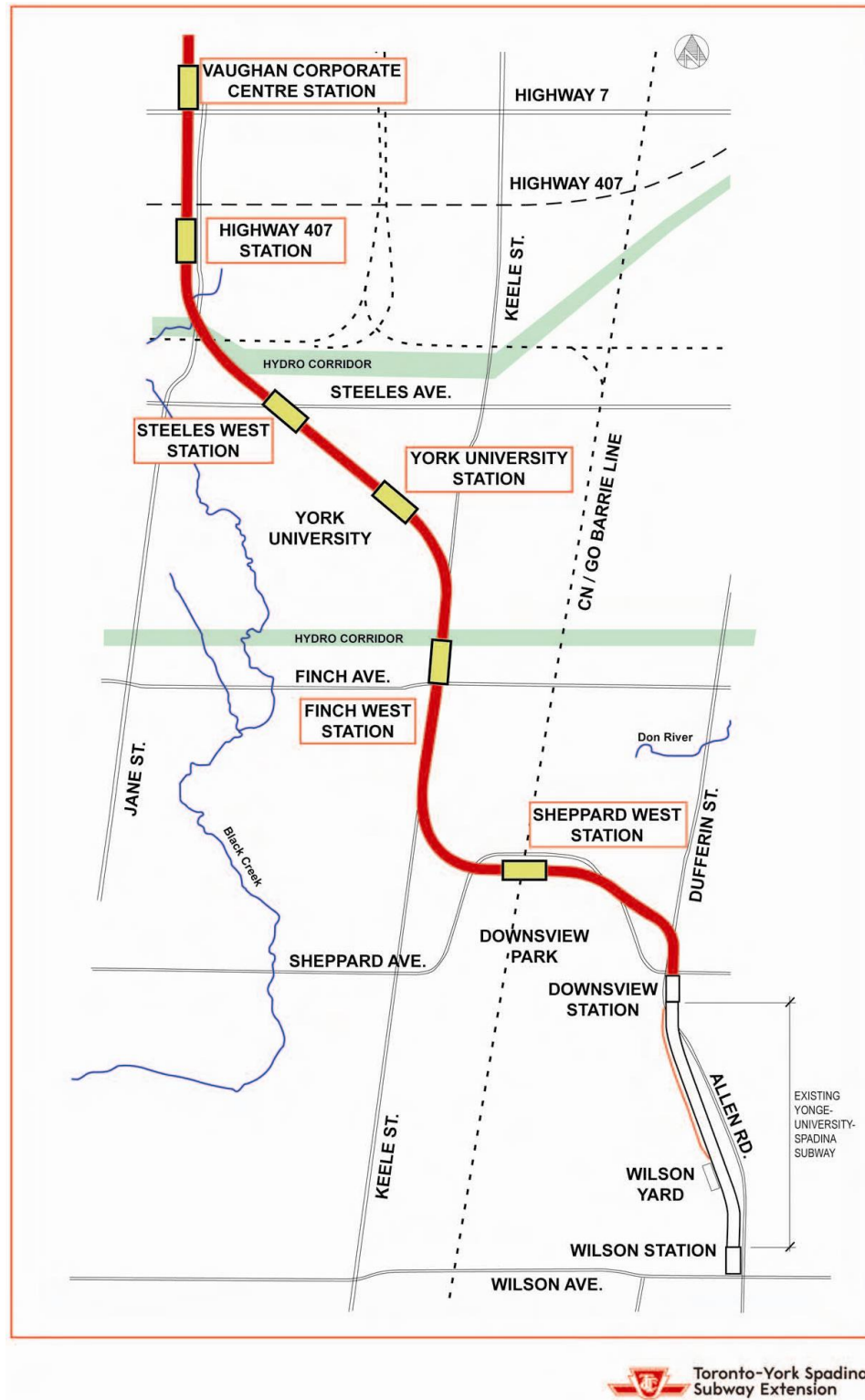


Figure 3.1 - Toronto-York Spadina subway extension map (TTC)

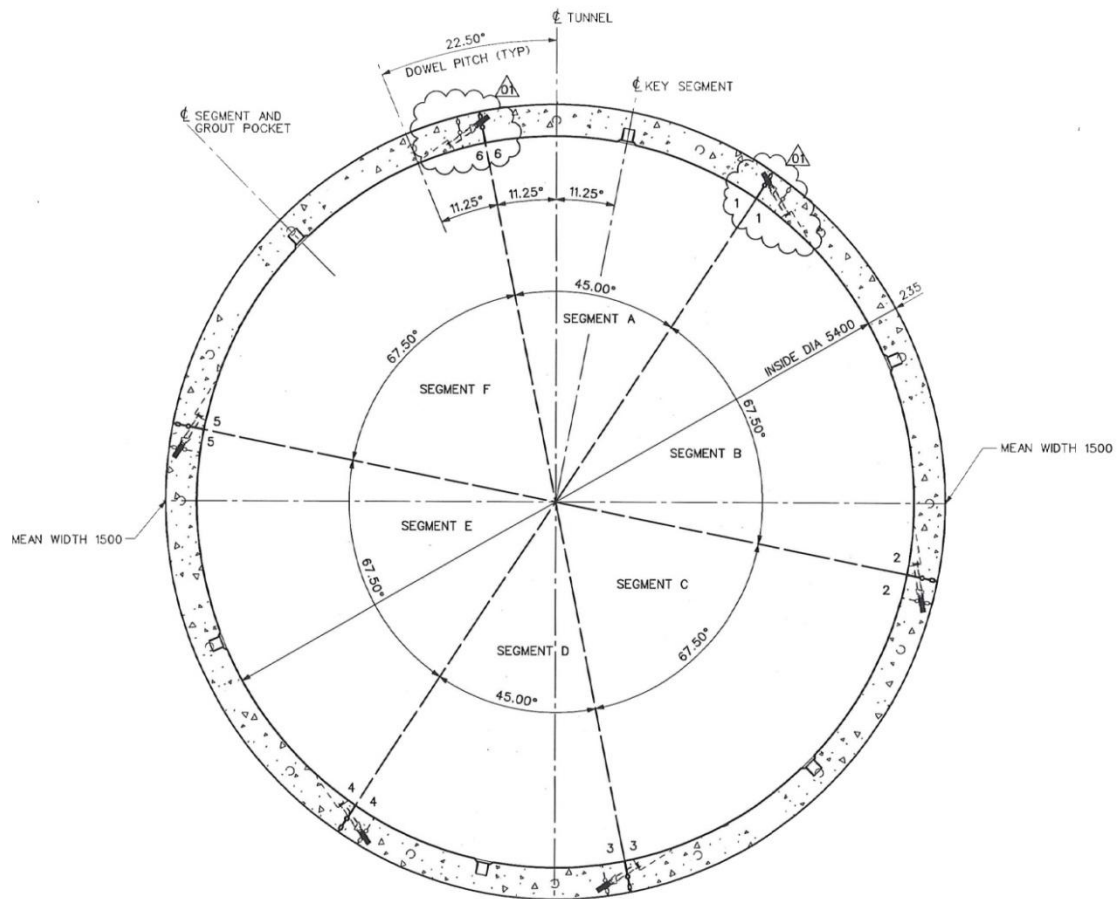


Figure 3.2 - Detail drawing of segment tunnel lining (HMM)

Number of segments	6 + 2 key segments
Thickness	235 mm
Medium ring depth	1500 mm
External diameter	5.87 m
Internal diameter	5.40 m
Angle per segments	67.5°, key segment 45°

Table 3.1 - Geometrical properties of TTC Spadina Line extension tunnel lining

The properties of the steel fibres used are summarised in Table 3.2 and the geometry of the steel fibres is given in Figure 3.3.

Fabricator	Bekaert - Dramix
Type of steel	Carbon
Shape	Hooked
Cross section	Circular
Ultimate tensile strength (MPa)	>1050
Dosage	57kg/m ³
Length (mm)	60
Diameter (mm)	0.75
Aspect ratio (l/d)	80

Table 3.2 - Steel fibre specifications

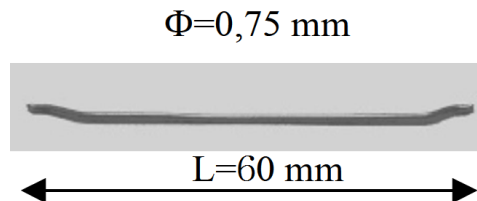


Figure 3.3 - Geometry of the Dramix -80/60- steel fibre

3.3 Arrangement for Conducting Flexure Test

3.3.1 Experimental Loading System

Each segment was tested in an extrados up orientation as shown in Figure 3.4. A uniaxial line load was applied at the middle of the segment using the hydraulic actuator. The hydraulic actuator could generate a maximum force of 1,450 kN with a maximum travel distance of 508 mm and had the ability to record load output to an accuracy of 10 N. The applied load, and movement of the actuator was controlled automatically by a computer system during both loading and unloading. The load-displacement was monitored during the test and recorded for future analysis.

The loading unit consisted of a two roller floor supports, a loading frame and a hydraulic actuator supported by two steel columns. The individual components are described in detail in the following sections.

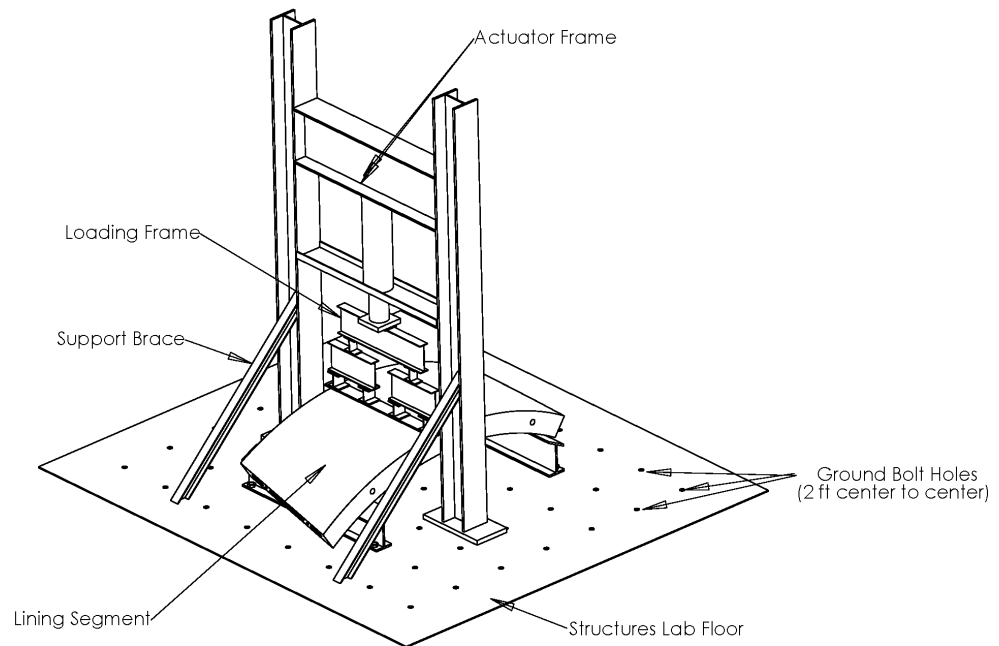


Figure 3.4 - Experimental system

3.3.2 Loading Frame

A loading frame was used to transmit a point loading from the actuator to a uniformly distributed line load acting on the concrete tunnel lining segment. The loading was applied at the midspan oriented at 90° to the central axis of the segment. Figure 3.5 shows an isometric view of the frame. It consists of a six W150x37, and three W310x24 strategically staggered I-beams with reinforcing web stiffeners. A steel loading plate of a 110 mm width, 620 mm length and 25.4 mm thickness was welded to the top of the frame to evenly transmit the load from the actuator to the frame.

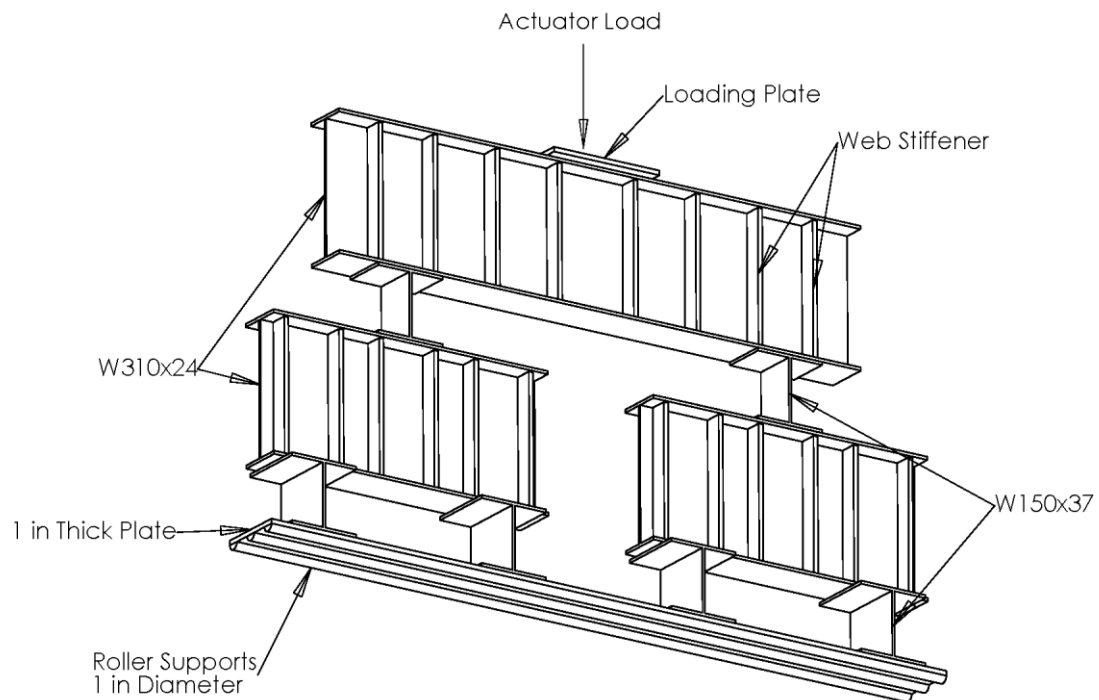


Figure 3.5 - Loading frame

The loading frame was designed based on a wiffle tree frame design (Moccichino *et al.*, 2006). This type of frame adequately distributes the force from a single point load, to a uniformly distributed line load as shown in Figure 3.6. A single force, P , is distributed into two point loads of $\frac{1}{2} P$. These forces are then distributed further into four loads of magnitude $\frac{1}{4} P$. These four point loads are then applied to a 150 mm wide, 25.4 mm thick, and 2000 mm long plate. Attached to this plate are three evenly spaced semi-circular rollers with a diameter of 25.4 mm. A rubber strip liner was placed between the frame and segment to accommodate for any out of plane shifting of the frame and to ensure uniform loading.

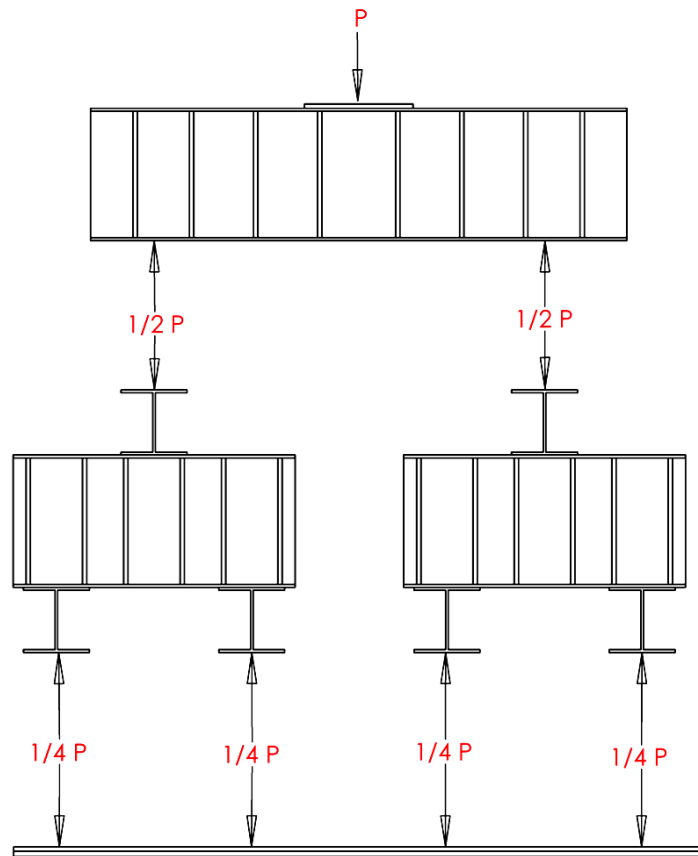


Figure 3.6 - Frame force distribution

3.3.3 Reaction Frame

The support system for the test setup consisted of two reaction frames spaced 2438 mm (8 feet) apart. Each reaction frame was bolted to the structures laboratory concrete slab floor with 50.8 mm (2 inch) diameter bolts, to prevent any movement. The frame comprised of a 25.4 mm (1 inch) thick rolled steel section fastened to a large I beam with a series of bolts. The roller allowed for displacement in the longitudinal direction but prevented any vertical movement. Figure 3.7 depicts the fundamental support system.

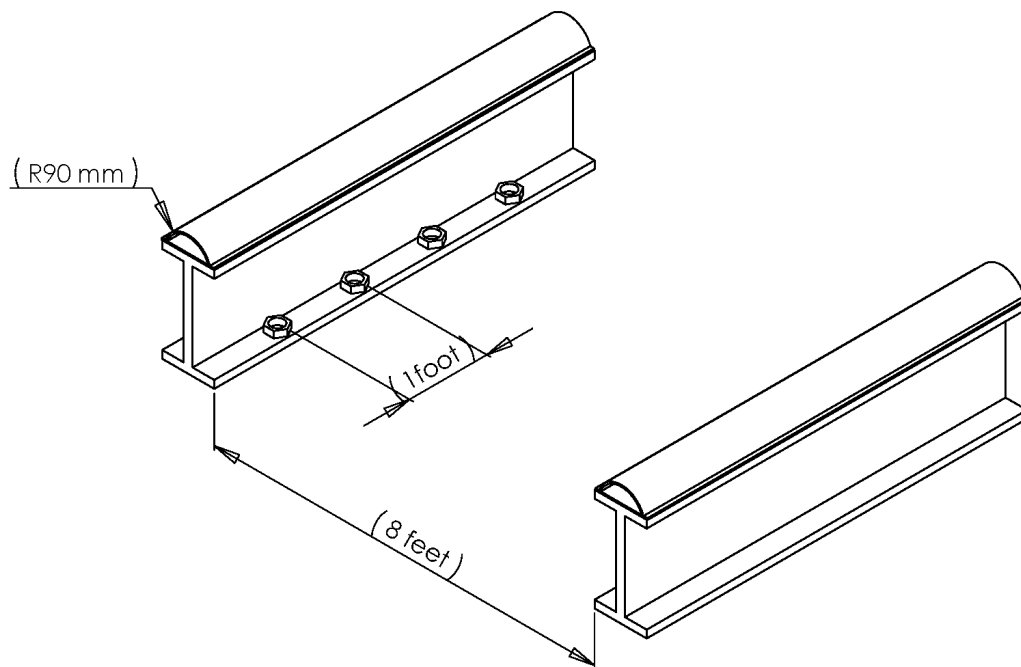


Figure 3.7 - Support system layout

3.3.4 Test Procedures

The following summarizes the test procedures used in determining the flexural response of SFRC tunnel lining segments:

- i) For each test, the segment was lifted using a 10 ton capacity overhead crane and placed on two support beams, which were fixed to the testing floor.
- ii) Strain gauges were bonded to the segment's extrados surface with a strong epoxy at six specific locations.
- iii) A 6.35 mm thick strip of stiff rubber was placed on the loading zone followed by the steel loading frame. The frame was positioned in the middle of the segment directly centered under the loading actuator.
- iv) Three LVDTs were placed at the midpoint of the segment to record vertical displacement; one in the centre and one on each edge to ensure uniform loading. Two LVDTs were also positioned on both ends of the segment recording horizontal displacement to ensure uniform loading.
- v) The actuator was brought into contact with the loading frame. The loading rate was set to 5 mm/min and the segment was loaded until failure.
- vi) Cracks were monitored and mapped during the testing using a digital camera for future analysis.
- vii) Post-failure, the actuator was unloaded, the gauges removed and the segment was broken up for later disposal.

3.4 Instrumentation of Segments

3.4.1 Displacement Transducers

To accurately estimate the flexural response of the tunnel segments, proper loading symmetry and boundary conditions needed to be established. Three LVDTs (D-1 to D-3) were used on the centreline of the individual segments to measure displacements at the midspan. In addition, two LVDTs (D-4 to D-7) were placed horizontally on each end of the specimen to verify that the segment was deforming symmetrically and to ensure that no torsion was present. Figure 3.8 illustrates the LVDT layout. The displacement transducers used were manufactured by Penny & Giles, having a maximum travel distance of 100 mm and a tolerance of ± 0.01 mm.

3.4.2 Strain Gauges

Strain measurements were also recorded during the test to provide estimates of localized load-strain responses. Eight strain gauges were fixed using high strength epoxy to the surface of the lining to provide strain estimates. The strain gauges were labelled S-1, S-2 and so on. Gauges S-1 to S-6 were bonded on the outer surface (extrados) while gauges S-7, S-8 were positioned on the intrados face. Post-test, the strain data was interpreted and load-strain graphs were plotted. Figure 3.8 illustrates the location of the strain gauges, which were located at $\frac{1}{4}$ points along the section. The uniaxial strain gauges used were manufactured by Showa Measurement Instrument Co. The gauge length was 30 mm, the sensitivity was $1 \mu\epsilon$ and the measurable strain ranged from 2% to 4% maximum.

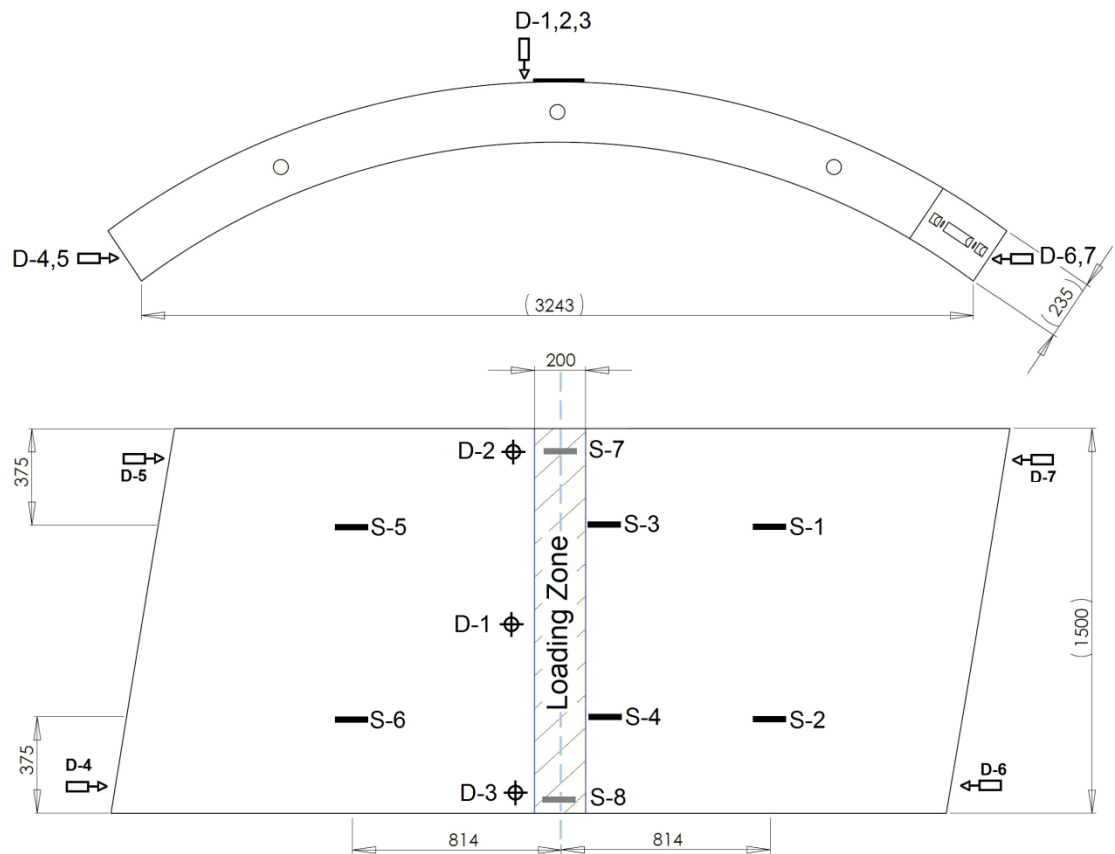


Figure 3.8 - Strain gauge and transducer layout

3.4.3 Crack Monitoring

The crack initiation and propagation at the midspan of the segment was monitored and analyzed for test SFRC-5 and SFRC-6 at the location shown in Figure 3.9. Photographs were taken at 60 second intervals using a Canon high resolution SLR camera, capturing the propagation of the crack during loading of the segment in a 150 mm wide and 235 mm high area. Image processing software, ImageJ, was used to analyze this propagation (Abramoff *et al.*, 2004)

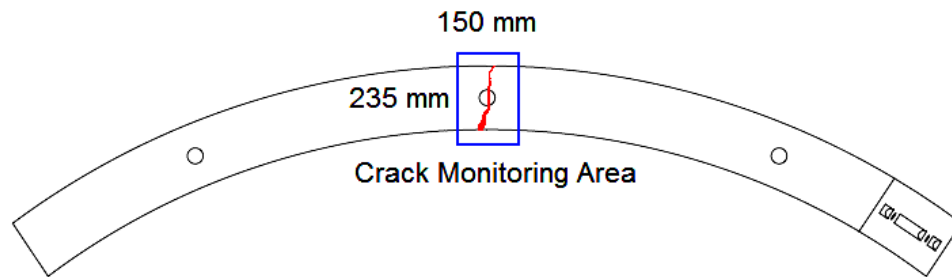


Figure 3.9 - Crack monitoring area

By modifying the intensity threshold of certain objects, and magnifying the image, the crack mouth opening displacement (CMOD) was determined with very high precision. Referring to Figure 3.10(b) a line was drawn at the magnified CMOD location. From this, a profile plot was generated. The profile plot showed the grey scale intensity along the drawn line. The grey scale value was lowest where the crack was present and this is clearly shown in Figure 3.11. The pixel distance of the crack opening was converted to “real world” coordinates by proportioning the pixel distance of a known reference length. This process was repeated for every subsequent photograph and the CMOD propagation throughout the test was plotted.

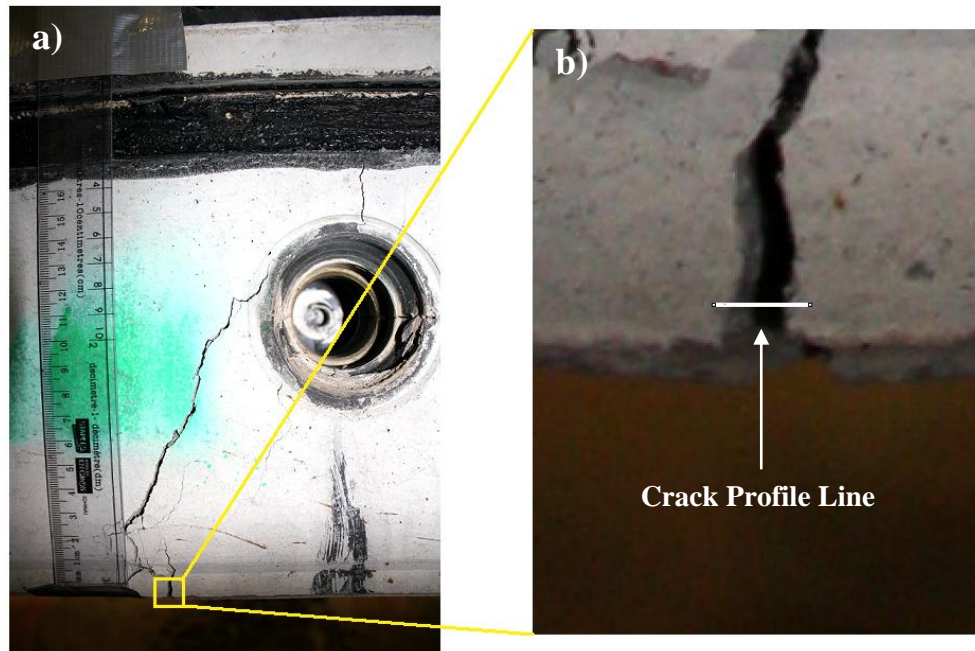


Figure 3.10 - (a) crack propagation (SFRC-6), (b) magnified image of CMOD

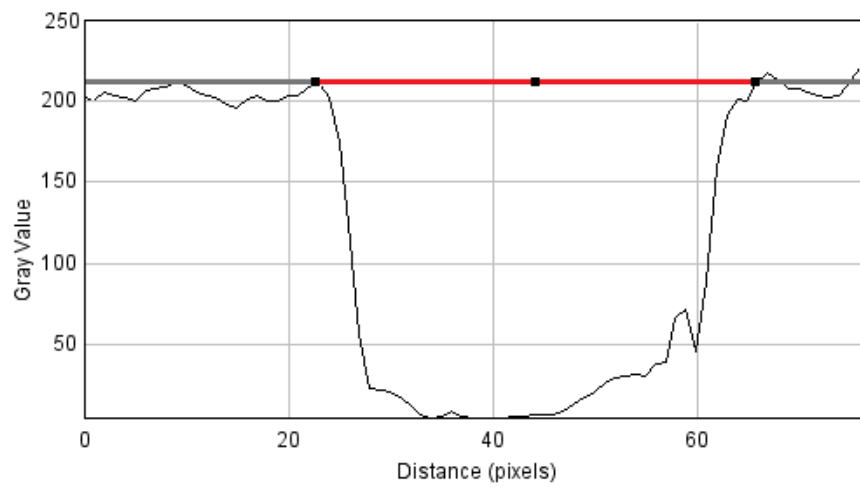


Figure 3.11 - Gray scale intensity profile plot of crack width (SFRC-6)

3.4.4 Computed Tomography

Computed tomography (CT) scanning allows for non-destructive two- and three-dimensional interior imaging of objects; it is used predominantly in medicine, biology and material sciences. It has effectively been employed previously in evaluating the interior structure of concrete mixes and for estimating the volume fraction of its constituents (e.g. Caliskan, 2007, Ghaffar *et al.*, 1992). The device attempts to relate changes in penetration of a particle, or x-ray beam through an object, to the density of that object. The data is then transmitted to a highly sophisticated computer processor, which transposes the data into a three-dimensional computer model. Using this technique, it was attempted to analyse and estimate the density fraction and fibre orientation of fibres in the SFRC cores.

Post-failure of tests SFRC-2 and SFRC-3, a core was extracted near the failure plane. The nominal core dimensions were 235 mm in length and 96 mm in diameter. A medical grade CT scanner was used in the analysis as shown in Figure 3.12. The CT scanning parameters utilized are presented in Table 3.3.

Afterwards, MicroView (3D image viewer software) was used in the visualization and analysis of the scanned cores. By altering the threshold and brightness of the 3D image, a distinction between fibres and other concrete elements is clearly visible. Utilizing gray-scale histogram profiles, the percentage of fibres in a given area can be determined. Furthermore, each core was divided into five subsections. In each subsection, the fibre fraction was determined using MicroView, allowing for the development of a fibre distribution profile with respect to segment thickness.

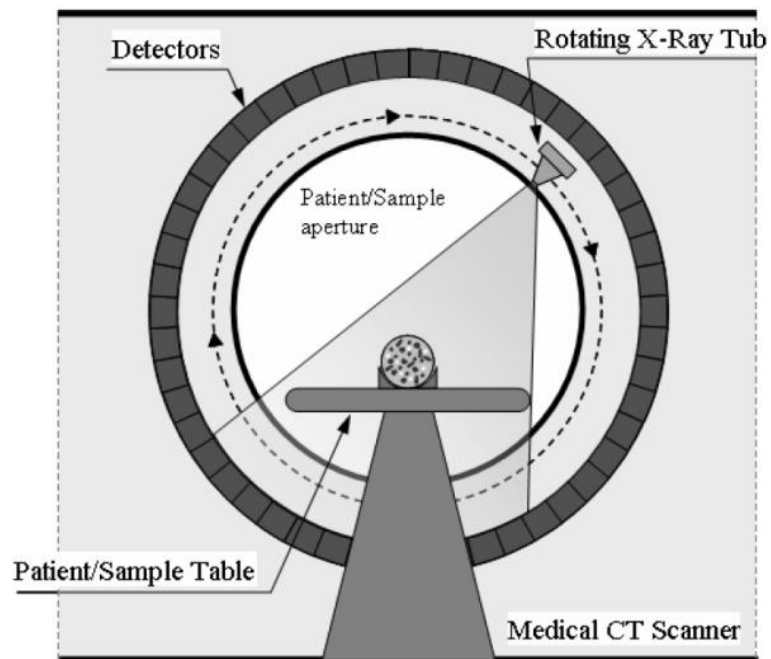
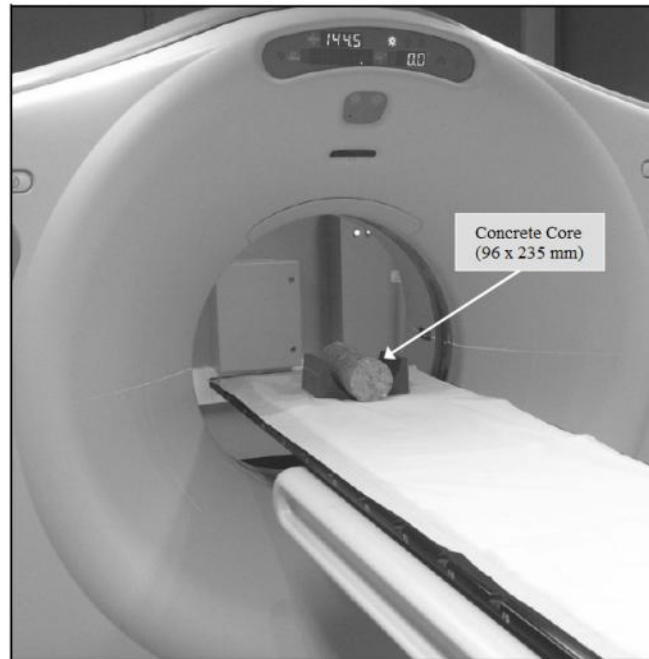


Figure 3.12 - General view of computed tomography scanning machine (Caliskan, 2007)

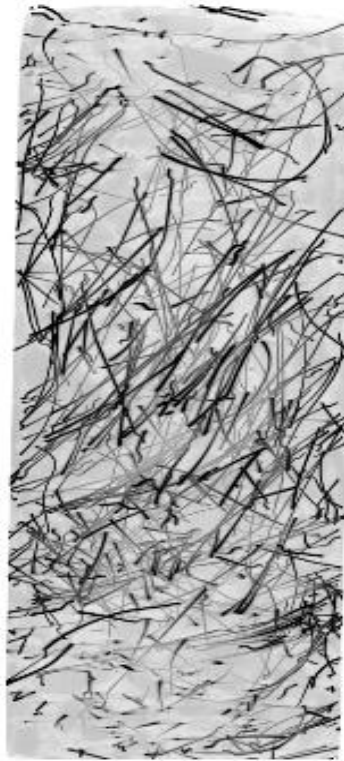


Figure 3.13 - Typical steel fibre reinforced concrete core computed tomography image

Scanner	GE Locus Ultra
X-ray exposure	120 kV and 20 mA
Exposure time	16 sec
Number of views	900
Effective pixel size	0.154 mm
Scan technique	360 degrees

Table 3.3 - Setting used for CT scanning of cores

3.5 Finite Element Numerical Analysis

3.5.1 ABAQUS Concrete Model

ABAQUS offers several different models of inelastic behaviour to represent a wide range of potentially brittle materials, such as metals, soils, cast iron, and concrete. Unfortunately, there is no specific model available for the modelling of SFRC structures. Nonetheless, the material behaviour of a particular model can be modified and adjusted in such a way as to appropriately represent the desired material behaviour (Pevsner *et al.*, 2005). There are two main types of constitutive models available in ABAQUS for the inelastic behaviour of concrete: the concrete damaged plasticity model (CDP) and the concrete smeared crack model (CSC).

The CDP model is a continuum, plasticity-based, damage model for concrete. It provides a general capability for modeling concrete using concepts of isotropic damaged elasticity in combination with isotropic tensile and compressive plasticity to represent the inelastic behaviour of concrete. It is designed to be used for applications in which the structure is subjected to monotonic, cyclic, or dynamic loading. It assumes that the main failure mechanisms are tensile cracking and compressive crushing of the concrete material. This model consists of a combination of non-associated multi-hardening plasticity and isotropic damaged elasticity to describe the irreversible damage occurring during the fracturing. The post-failure behaviour for direct straining is modelled with tension softening parameters which define the strain softening behaviour for cracked concrete. This behaviour also allows the effects of the reinforcement interaction with concrete to be simulated in a simple manner (ABAQUS Analysis User's Manual, 2006).

The CSC model is intended to model concrete behaviour for monotonic loading, however for fairly low confining pressures, less than four to five times the maximum stress that can be carried by the concrete in uniaxial compression. Accordingly, this model has been noted to have issues converging past the yielding point of concrete (Ahn, 2011).

The CDP model requires compressive and tensile input parameters to accurately model the material behaviour. The uniaxial compressive response is linear-elastic until the value of initial yield, σ_{c0} , is reached. The material experiences a hardening effect, ultimately reaching a maximum compressive stress, σ_{cu} , followed by a softening branch. If the concrete specimen is unloaded from any point on the strain softening branch, of the stress strain curve, the unloading response is weakened. The elastic stiffness of the material is considered damaged, as some residual stress remains present (Figure 3.14a).

The uniaxial tensile stress-strain response is initially linear-elastic, with the same modulus of elasticity as in compression. As the tensile failure stress, σ_{t0} , is reached, cracking initiates in the concrete. Following this, a post-failure strain softening behaviour ensues, which can be modelled in ABAQUS with tension stiffening parameters. The tension stiffening can be specified by means of post failure stress-strain (σ - ϵ) relation (discussed in Section 3.7.3) or by applying a fracture energy cracking (σ - ω) criterion developed from flexure beam testing.

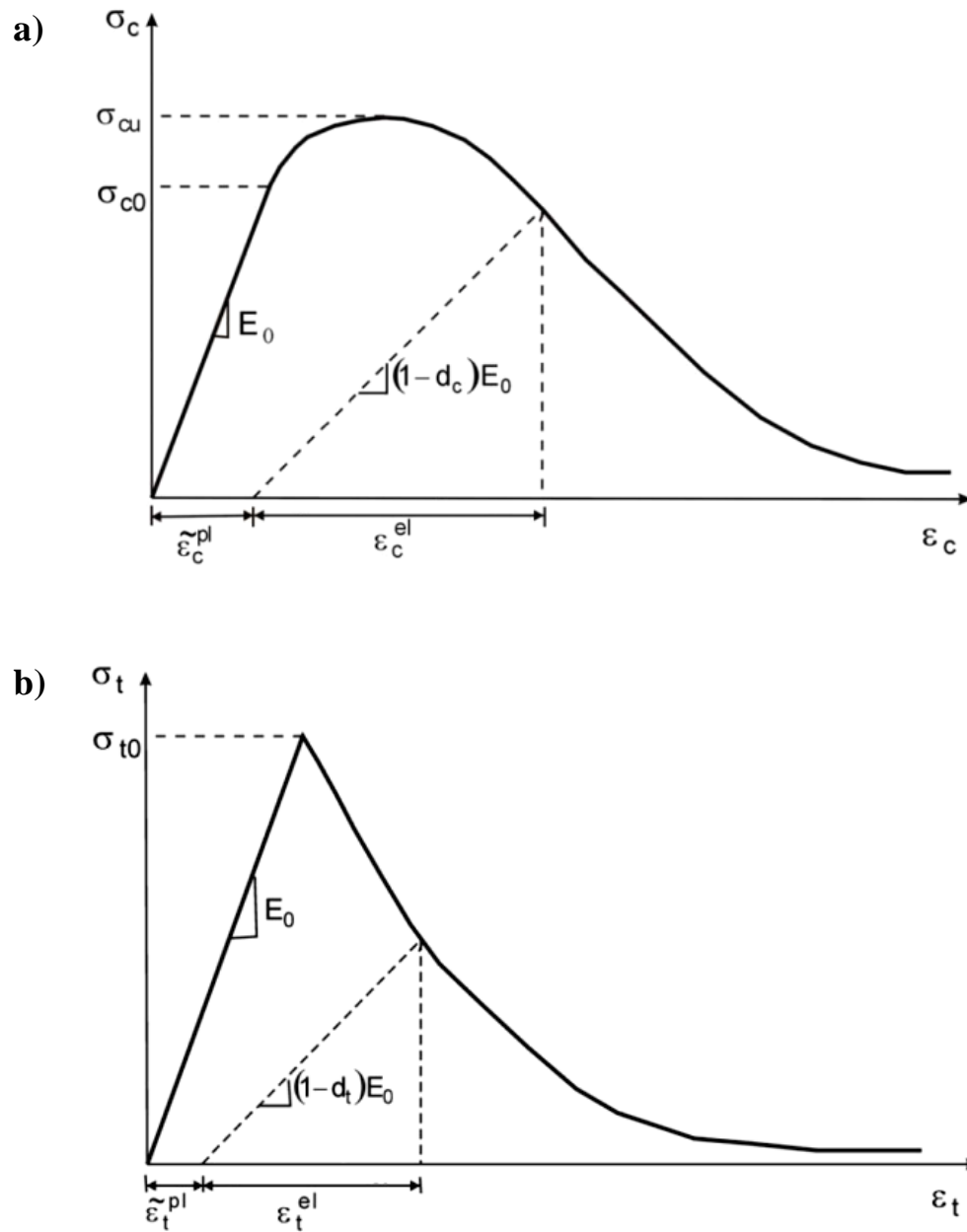


Figure 3.14 - Uniaxial loading concrete response (a) compression and (b) tension (ABAQUS, 2006)

In addition to the compressive and tensile parameters that identify the stress-strain relationship, parameters based upon the microstructure of the concrete must also be identified. The CDP model includes the dilation angle Ψ , flow potential eccentricity m , initial biaxial/uniaxial ratio σ_{c0}/σ_{b0} , the ratio of the second stress invariant on the tensile meridian to that on the compressive meridian K_c , and the viscosity parameter μ . These parameters are related to the yield surfaces of the individual finite concrete elements. As mentioned previously, concrete has different yield stress in compression and tension; in essence, a yield surface attempts to envelope these stresses in order to create an interaction relationship. The yield surface of the concrete damage plasticity model is given in Figure 3.15 where the enclosed area represents the elastic states of stress. In plane stress conditions, the yield function presents a shape that is close to the real behaviour of concrete (Burgers, 2006).

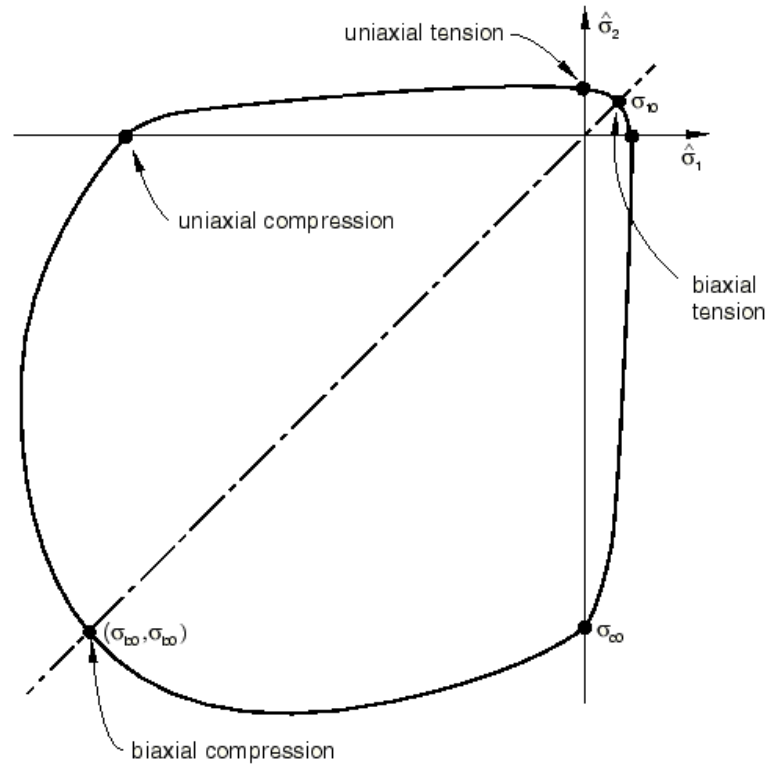


Figure 3.15 - Bi-linear yield surface of concrete (ABAQUS, 2006)

In this study, it was desirable to capture the material behaviour up to and past the peak loading and so the concrete damage plasticity model, which exhibits a non-linear ascending curve followed by a softening post peak response, was chosen. The default finite element CDP model parameters were used in this analysis and are summarized in Table 3.4. The first two parameters (dilatation angle and eccentricity) control the plastic straining response of the material and since the later segment analyses will be unrestrained, there should be little change with the dilation angle and eccentricity. The next two parameters (σ_{c0}/σ_{b0} and K_c) determine the shape and size of the bi-linear yield surface. Since the response of the segments will be predominately uniaxial, it is not anticipated that there will be significant changes to the analyses by varying these parameters. The viscosity has been set to zero and this assumes that there are no strain rate effects.

Material Properties	Value
Unconfined compressive strength (f_{cu})	60 MPa
Young's Modulus (E)	37.2 GPa
Poisson's Ratio (ν)	0.15
Density (ρ)	3000 kg/m ³
CDP Parameters	Value
Dilation angle (Ψ)	36.31°
Viscosity Parameter (μ)	0
Eccentricity (m)	0.1
σ_{c0}/σ_{b0}	1.16
K_c	0.67

Table 3.4 - Material and concrete damage plasticity (CDP) parameters

3.5.2 Loading and Boundary Conditions

The geometric properties of the tunnel segment were modeled to fit the prototype dimensions. The segment details (eg. bolt pockets, shear key, grout pocket) were initially modelled however mesh concentrations at the corners of these details resulted in convergence issues and so it was decided to disregard them in the modelling process. The segment width, thickness and internal diameter were 1500 mm, 235 mm, and 2700 mm, respectively. The loading and boundary conditions implemented into ABAQUS simulated the experimental test setup. At one end of the segment, a pin support was produced by setting the allowable displacement, $U1=U2=U3=0$, limiting movements in all three directions. On the other end, a roller support was simulated with $U2=0$, preventing any vertical displacement, but allowing transverse movement. Both ends were free to rotate and were spaced 2,438 mm apart following the experimental setup. A 150 mm wide and 1500 mm long rigid plate was configured at the midspan of the segment. A displacement controlled loading of 20 mm was used, simulating the laboratory loading applied. Figure 3.16 shows the boundary conditions and load distribution applied.

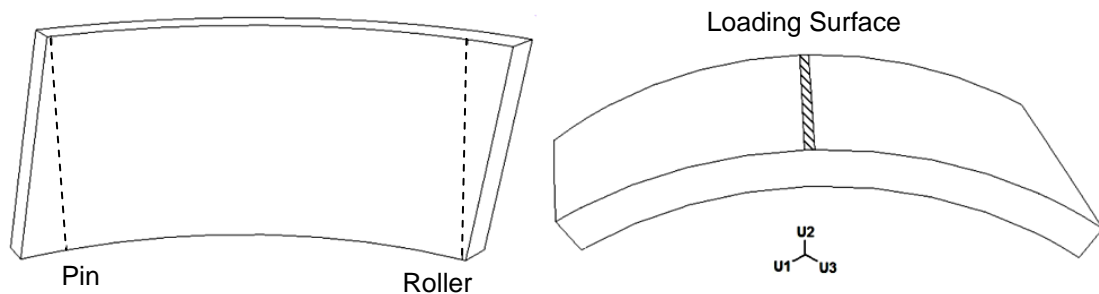


Figure 3.16 - Boundary conditions and loading distribution

3.5.3 Mesh Development

The elements used and their size/arrangement in a finite element mesh plays a significant role in a numerical simulation. ABAQUS uses an array of points defined as nodes which form a grid called a mesh. The structural and material properties are programmed within this mesh and determine how the structure will react to certain loading condition. Generally, an element with a higher number of nodes (higher order element) yields a more accurate analysis. ABAQUS offers 3D element types: tetrahedral, wedge, and hexahedral (brick). Figure 3.17 illustrates each element, along with the number of associated nodes. The tetrahedral element is limited to only four nodes per element and risks severe locking of tetrahedrals when exposed to problems with plasticity and acute bending (Puso *et al.*, 2006). It takes five tetrahedral elements to fill the volume of one brick element and hence many more elements are required to produce a converged solution. In comparison, an eight-noded hexahedral (brick) element has higher capabilities of converging due to its increased node count, resulting in a more accurate analysis. Due to this, linear isoparametric hexahedral elements were chosen as the element type in this study.

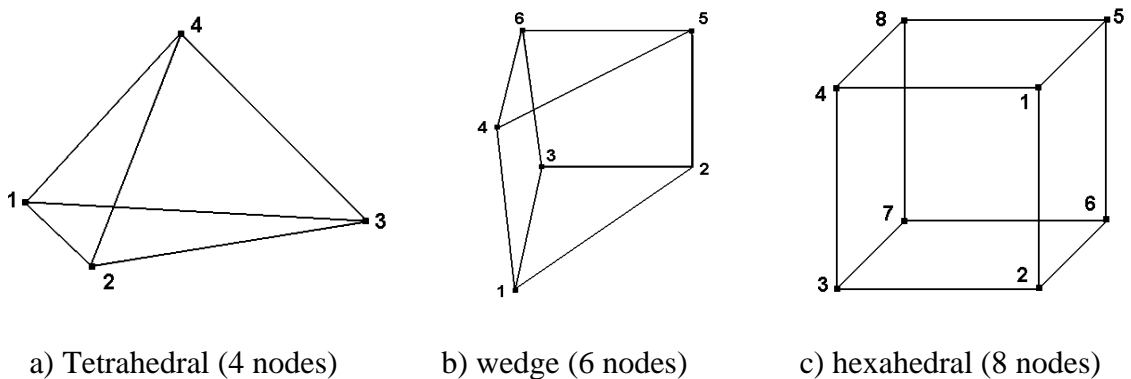


Figure 3.17 - Element types: tetrahedral, wedge, and hexahedral

Furthermore, the controlled cracking of concrete is one of the most important aspects of SFRC non-linear behaviour. One desirable attribute of the finite element method is convergence of the solution with reasonable mesh refinement. However, finite element solutions are known to have difficulty converging if the materials being modeled contain softening formulations (Murray *et al.*, 2007). Researchers conducting numerical methods to perform the non-linear analysis of concrete structural members have noted certain computational difficulties that arise due to mesh dependency influences. In particular, the element size within a SFRC model has been found to affect the structural behavioural response, such as the load-displacement and load-strain characteristics, and ultimate load capacity (Shayanfar *et al.*, 1997). This is because the load response behaviour is highly dependent on the cracking propagation and crack width. If a finite element within the cracking zone is too coarse, the response may appear to be stiffer than in reality, because only one crack is being modeled within the element length, when in reality there are two. If the stress remains constant, the resultant deformations would be much lower if only one crack was being modelled (Burgers 2006). On the other hand, a finer mesh results in a much longer computation time, but yields a more accurate analysis. Additionally, if a mesh is refined too much in a non-linear analysis of concrete, the response may actually appear softer than in reality (Tlemat *et al.*, 2005). To overcome these issues, it is necessary to produce an appropriately sized mesh to efficiently capture the cracking behaviour (Tlemat *et al.*, 2005; Jankowiak *et al.*, 2005; Noel *et al.*, 2012). This can be achieved by employing an inverse analysis method, which consists of refining the mesh size until the numerical behaviour matches the experimental test data (eg. Tlemat *et al.*, 2005; Burgers 2006).

Lastly, the softening behaviour of a material is defined as the reduction in strength with continued straining once a damage threshold is reached. Murray *et al.*, (2007) used regulation of softening with respect to mesh size, i.e. material parameters are also a function of the element size. It was found that regulation in compression decreased brittleness, while regulation in tension increased brittleness (as the mesh was refined). Hence, if an analysis is conducted with a mesh that is too crude, there is a tendency to under predict tensile damage and over predict compressive damages.

3.6 Compressive Material Properties

3.6.1 Analytical Solution

Various closed form equation models describing the compressive stress-strain relationship have been proposed by Barros and Figueiras (1999), Bencardino *et al.*, (2007), Ezeldin and Balaguru (1992), and Nataraja *et al.*, (1999); they all have relatively similar approximations of the concrete behaviour subjected to uniaxial compression (Burgers, 2006). Generally, steel fibres only have minor effects on the ultimate compressive strength of concrete, slightly increasing or decreasing its magnitude, depending on the characteristics of the fibres themselves (ACI 544.1R-96, 1996, ACI 544.3R-2, 1998). However, to ensure full accuracy, a solution used to model SFRC was still employed. The compressive stress-strain behaviour of the SFRC concrete was based on analytical solutions for plain concrete (Carreira *et al.*, 1985). Slight modifications to the base curve were then employed to fit the SFRC parameters (Luiz Alvaro de Oliveira Junior *et. al*, 2010). The procedure undertaken is described below.

1. Peak strain for plain 60 MPa concrete

$$\varepsilon_o = 0.00076 + \left[\left(0.626 \frac{f_c'}{f^*} - 4.33 \right) \times 10^{-7} \right]^{\frac{1}{2}} \quad [\text{Eq. 3.1}]$$

Where ε_o = the strain at peak stress, f_c' = unconfined compressive strength (MPa), $f^* = 1$ MPa. The strain at peak stress for 60 MPa plain concrete is determined using equation 3.1. This equation shows a strong correlation between the compressive strength (f_c') and strain at peak stress (ε_o) to experimental results for concrete with a wide range of compressive strength (i.e. from 10 MPa to 100 MPa).

2. Determining the fibre influence factor

$$\beta = [0.0536 - 0.5754 V_f] f_c' \quad [\text{Eq. 3.2}]$$

Where β = fibre influence factor, V_f = steel fibre volumetric fraction (%), f_c' = compressive strength (MPa)

3. Determining the stress at arbitrary strain

$$\sigma_c = \frac{f_c' \beta \left(\frac{\varepsilon}{\varepsilon_o}\right)}{\beta - 1 + \left(\frac{\varepsilon}{\varepsilon_o}\right)^\beta} \quad [\text{Eq. 3.3}]$$

Where σ_c = compressive stress (MPa), f_c' = compressive strength (MPa), ε = arbitrary strain, ε_o = strain at peak stress, and β = fibre influence factor. Using Eq. 3.1, 3.2 and 3.3, concrete stresses at any strain can be calculated. The calculated stress-strain behaviour of 60 MPa concrete is plotted in Figure 3.18.

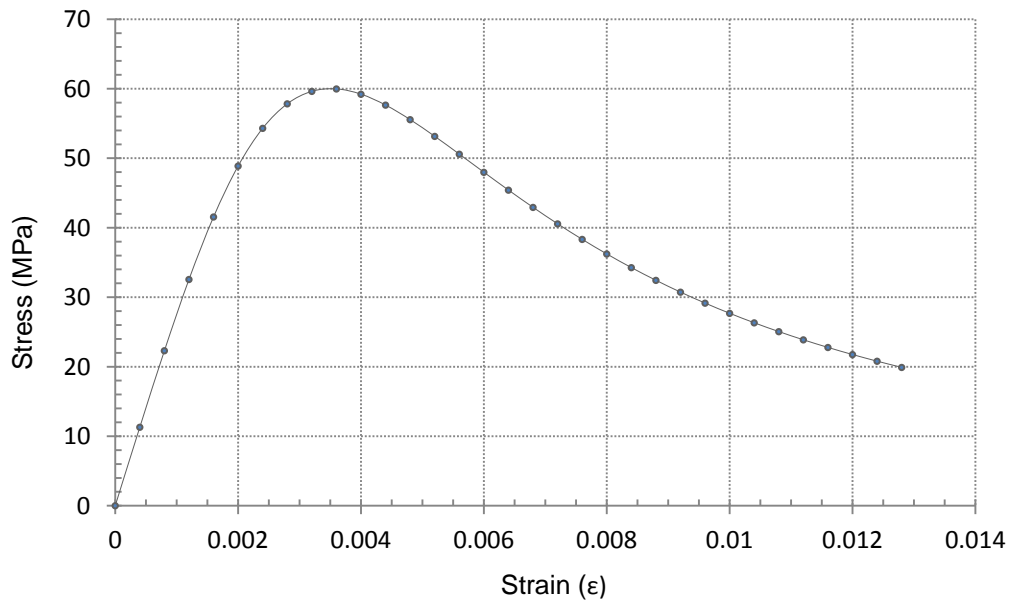


Figure 3.18 - Stress-strain curve for 60 MPa concrete used in the finite element analysis

4. Elastic modulus of 60 MPa concrete (Vandewalle *et al.*, 2003)

$$E_c = 9500 (f'_c)^{\frac{1}{3}} \quad [\text{Eq. 3.4}]$$

Where E_c = modulus of elasticity (MPa), f'_c = unconfined compressive strength (MPa).

For a 60 MPa concrete, the modulus of elasticity is 37.2 GPa.

3.6.2 Experimental Cylinder Strength Tests

To validate the theoretical compressive stress-strain model of the SFRC material, uniaxial compressive strength tests were performed. Eight cylinder cores were drilled from a SFRC key segment using a CAT core-bore drilling machine. The cores were taken from random locations of the segment to represent the average material strength. Each core had a nominal length of 235 mm and diameter of 96 mm. Unconfined compression tests were performed on the cylinders to characterize the compressive stress-strain behaviour of the SFRC according to ASTM C39-10 (Standard Test Method for Compressive Strength of Cylindrical Concrete Specimens).

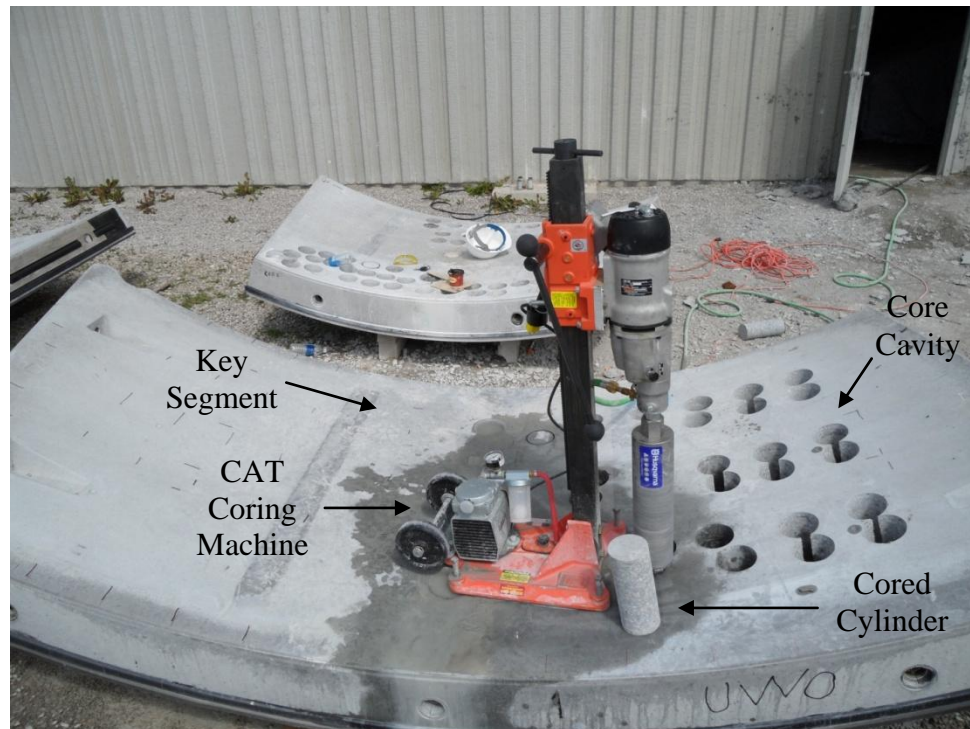


Figure 3.19 - Coring machine setup

To minimize end effects (stress concentrations), each specimen was cut using a diamond blade saw, to achieve flat orthogonal ends. The resulting nominal dimensions of each core were 200 mm in length and 96 mm diameter. In addition, sulfur caps were produced at the end of each specimen, according to ASTM C617-10 (Standard Practice for Capping Cylindrical Concrete Specimens), to ensure uniform stress propagation. Furthermore, four cores were equipped with axial strain gauges bonded vertically in the centre of each specimen to record strain change during compression. These tests were performed using a computer controlled axial compressive machine. Figure 3.20 illustrates the prepared cores for the cylinder compression tests.



Figure 3.20 - Concrete cylinders equipped with sulfur caps and vertical strain gauge

The average compressive strength for the SFRC core specimen was 61.92 MPa. According to ASTM C42/C 42 M-04, the core strengths are generally representing 85% of the corresponding standard cured cylinder. Therefore, a factor of 1.17 was applied to the core strength to get the equivalent cylinder strength. Table 3.5 shows the average strength and standard deviation of the core strength and equivalent cured cylinder strength for SFRC.

The average standard cured cylinder strength of the SFRC was 72.41 MPa with a standard deviation of 7.34 MPa. Additionally, according to ASTM C39-10 and ASTM C670, the allowable compressive strength range of eight specimens sized 200 mm by 100 mm is 13.76 %. From the experimental testing, a range of 38.35% in the standard cured cylinder strength is present, demonstrating a degree of variability across the segment. Furthermore, the minimum strength from the eight specimens was 62.24 MPa, conforming to a minimum design criterion of 60 MPa. Because the eight cores were retrieved from random locations of the segment, this suggests the possibility of even lower concrete strength in certain locations. Thus, a design compressive strength of 60 MPa was chosen as a conservative approach.

Specimen	Core strength (MPa)	Standard cured cylinder strength (MPa)
C-1	63.41	74.19
C-2	63.60	74.41
C-3	55.56	65.01
C-4	60.27	70.52
C-5	73.62	86.11
C-6	53.23	62.24
C-7	67.96	79.44
C-8	57.68	67.39
Average	61.92	72.41
Standard Deviation	6.28	7.34

Table 3.5 - Concrete core compressive strength results

Moreover, specimens C5-C8 were also employed with strain gauges. The gauges were placed vertically at the centre of the specimens to capture the most representative strain field by avoiding stress concentration effects near boundary conditions. The uniaxial strain gauges used were manufactured by Showa Measurement Instrument Co. The gauge length was 30 mm, the sensitivity was $1\ \mu\epsilon$ and the measurable strain ranged from 2% to 4% maximum. The resulting stress-strain relationship deduced from the experimental compressive strength tests is plotted in Figure 3.21. It can be concluded that the theoretical stress-strain curve (from Figure 3.18) is representative of the compressive strength of the SFRC concrete tunnel lining segments and will thus be used in characterising the compressive material properties in later chapters.

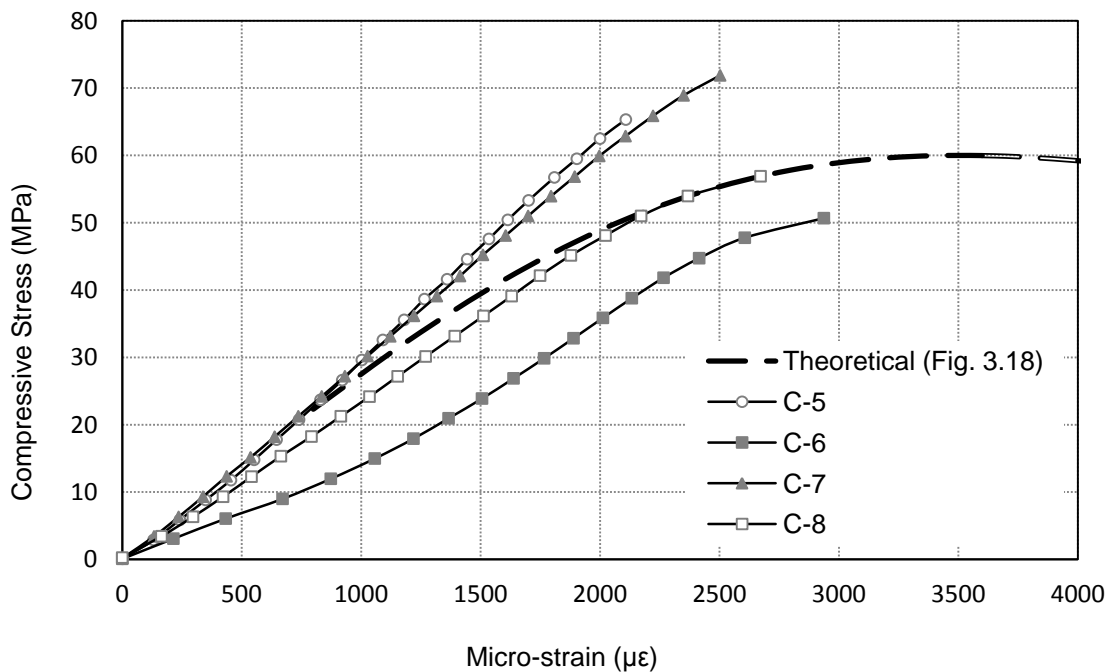


Figure 3.21 - Cylinder core compressive stress-strain

3.7 Tensile Material Properties

The concrete damage plasticity model (CDP) in ABAQUS requires the tensile behaviour of concrete to be well characterized with tension stiffening parameters. The tension stiffening can be specified by means of a post-failure stress-strain (σ - ϵ) relation or by applying a fracture energy cracking (σ - ω) criterion which relates the tensile stress with the crack width displacement (ABAQUS Analysis User's Manual, 2006). The σ - ϵ design method proposed by Vandewalle *et al.*, (2003) in Section 3.7.2 was used for approximating the stress-strain parameters from experimental three-point bending beam tests.

3.7.1 Flexural Beam Testing

The tension stiffening parameters required to define the concrete damage plasticity model in finite element software ABAQUS, can be deduced from flexural beam tests following ASTM C1609M-10 (Standard Test Method for Flexural Performance of Fiber-Reinforced Concrete). This method is particularly of interest when analysing complex materials such as steel fibre reinforced concrete.

The use of SFRC is continuing to increase, but this development is being hindered by a general lack of theoretical knowledge and methods for its design, particularly under flexural loading. Generally there is currently a lack of analytical design methods for determining the tensile behaviour of SFRC (Jones *et al.*, 2008). Thus, the mechanical properties of SFRC must be determined empirically by means of standardized laboratory tests. Three-point bending tests on notched beam specimens are often performed to characterise the flexural performance of SFRC. Figure 3.22 illustrates a standardized test setup.

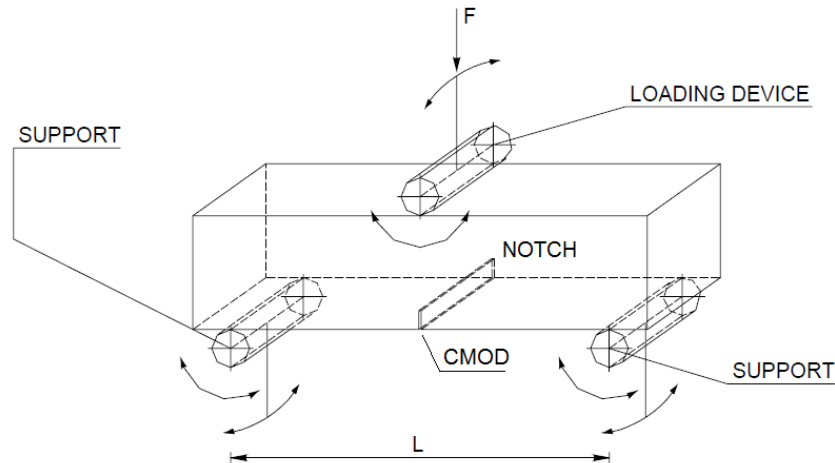


Figure 3.22 - Standardized flexural beam test setup (Jankowiak *et al.*, 2005)

In the middle of the span, the specimen may be notched (typically 2-3 mm wide) to a depth of 25 mm (RILEM TC 50). As the beam is loaded, the notch tends to “open up” and a crack originates at the notch tip, propagating vertically upward. The widening crack is measured using a clip gauge placed across the notch location. The degree of crack opening is characterized as the crack mouth opening displacement (CMOD) and is an index for evaluating the crack opening during the fracture of concrete. The load-CMOD curve or load-deflection curve obtained from testing can be used to approximate the stress-strain relation of the material using fracture mechanics theories following Vandewalle *et al.*, (2003), as discussed in Section 3.7.3. This approximation characterises the uniaxial tensile properties of the SFRC necessary for the numerical analysis using the CDP model.

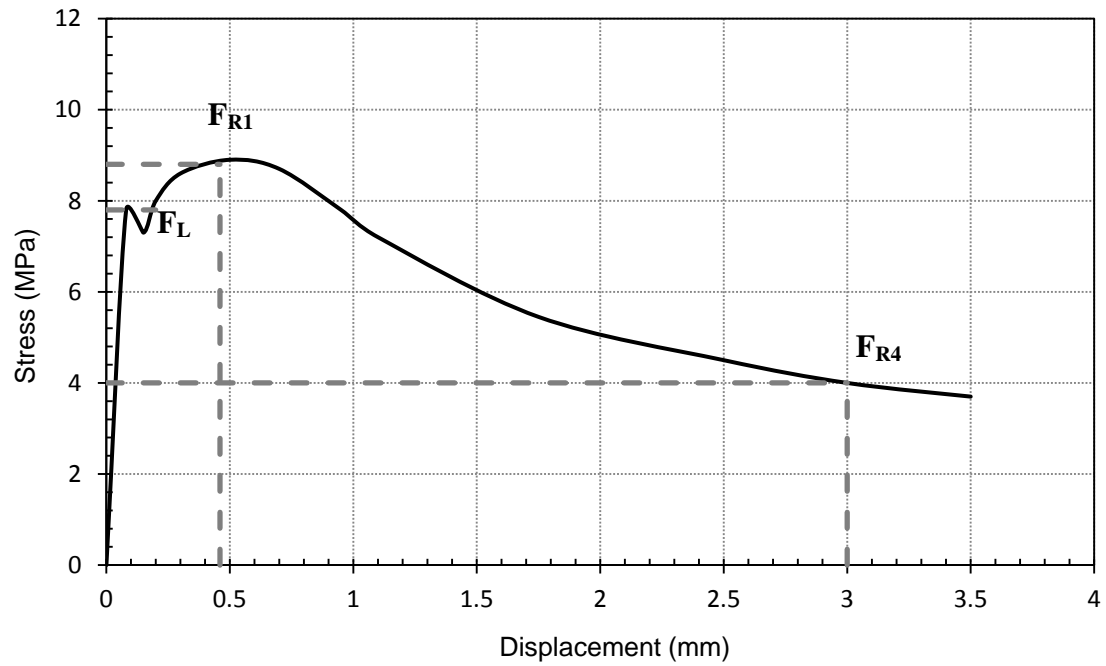


Figure 3.24 - Typical beam test load-deflection data (TEC Services, 2010)

3.7.3 Tensile Stress-Strain Approximation

Several constitutive models exist for determining the tensile behaviour of SFRC concrete (Barros and Figueiras, 1999; Tlemat *et al.*, 2006; Lok and Pei, 1998; Lok and Xiao, 1999). The residual strength of SFRC is much higher than that of plain concrete and also has a greater effect on the overall behaviour of the material; care must be therefore taken when using a model to approximate the tensile behaviour. Vandewalle *et al.*, (2003) proposed a “ σ - ϵ design method” as an attempt to characterise the softening behaviour of SFRC using experimental beam test data. Figure 3.25 illustrates this bi-linear approximation of the post-cracking behaviour for SFRC.

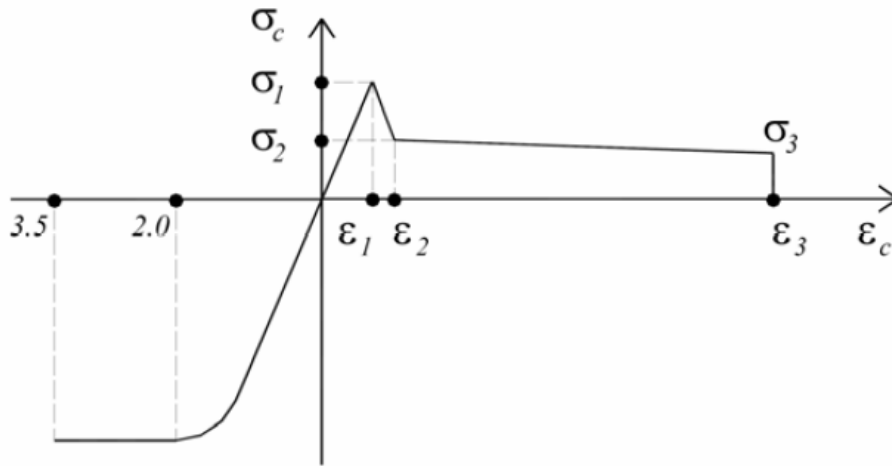


Figure 3.25 - Bi-linear approximation of the post-cracking behaviour of SFRC

The methods proposed by Vandewalle *et al.*, (2003) were used in approximating the uniaxial stress-strain tensile parameters based on the stress-deflection data established from these beam tests. The procedure undertaken is described below.

1. Find limit of proportionality, F_L , and residual flexural loads, F_{R1}, F_{R4} (Figure 3.24)

The limit of proportionality, F_L , is defined as the load directly following the linear-elastic response. However, if there is no clear end of the linear-elastic portion, then the limit of proportionality is defined as the maximum load sustained up to a displacement of 0.05 mm (Barros and Figueiras, 1999).

The residual flexural loads, F_{R1}, F_{R4} are defined as the loads that correspond to the beam deflections $\delta_1 = 0.46$ mm, and $\delta_4 = 3.00$ mm, respectively for a standard sized beam.

Parameter	Stress (MPa)	Corresponding Load (kN)
F_L	7.80	57.58
F_{R1}	9.00	66.43
F_{R4}	4.00	29.53

Table 3.6 - Limit of proportionality and residual flexural loads

2. Establish the flexural tensile strength, f_t , and residual flexural strengths f_{R1}, f_{R2}

The residual flexural tensile strength is determined from:

$$f_{Ri} = \frac{3F_{Ri}L}{2bh^2} \quad [\text{Eq. 3.5}]$$

Where f_{Ri} = residual flexural tensile strength (MPa), F_{Ri} = load recorded at specified displacement (kN), b = width of the specimen (mm), h = height of the specimen (mm), L = span of the specimen (mm).

The corresponding span, width, and height of the beam tests conducted were 450 mm, 150 mm, and 150 mm, respectively. By implementing the flexural loads from Table 3.6 into Eq.3.5, the following flexural parameters are deduced: $f_t = 11.51$ MPa, $f_{R1} = 13.28$ MPa and $f_{R4} = 5.90$ MPa.

3. Determine the size factor, k_h

The size factor can be found from:

$$k_h = 1.0 - 0.6 \frac{h-12.5}{47.5} \quad [\text{Eq. 3.6}]$$

Where k_h = size factor, h = height of the specimen $|12.5 \leq h \leq 60|$ (cm). The size dependant safety factor takes into account the test beam size and modifies the characteristic tensile behaviour accordingly. Given a 150 mm beam height, the corresponding size factor = 0.97.

4. Determine the tensile stress values $\sigma_1, \sigma_2, \sigma_3$

$$\sigma_1 = C_1 (1.6 - h) f_t \quad [\text{Eq. 3.7}]$$

$$\sigma_2 = C_2 f_{R1} k_h \quad [\text{Eq. 3.8}]$$

$$\sigma_3 = C_3 f_{R4} k_h \quad [\text{Eq. 3.9}]$$

Where σ_i = stress (MPa), C_i = stress coefficients, f_{Ri} = residual flexural tensile strength (MPa), h = height of the specimen (m), k_h = size factor, f_t = flexural tensile strength (MPa)

The stress coefficients are used to relate the stress-strain parameters and the experimentally determined flexural strengths. The stress coefficients used in this study

were taken from ACI 544 XXE (2008), and are as follows: $C_1 = 0.52$, $C_2 = 0.36$, $C_3 = 0.27$. These coefficients can be modified with inverse analysis of the experimental data, to achieve a better fitting tensile behaviour.

Implementing the previously calculated variables into Eq. 3.7-3.9, this yields the following tensile stress values, $\sigma_1 = 8.42$ MPa, $\sigma_2 = 4.63$ MPa, and $\sigma_3 = 1.54$ MPa.

5. Determine the modulus of elasticity E_c

The modulus of elasticity is determined from:

$$E_c = 9500(f'_c)^{\frac{1}{3}} \quad [\text{Eq. 3.9}]$$

Where E_c = modulus of elasticity (MPa), f'_c = compressive strength of concrete (MPa).

Given a 60 MPa concrete, the resulting modulus of elasticity is 37.2 GPa.

6. Determine tensile strain values, ε_1 , ε_2 , and ε_3

The tensile strain value, ε_1 , is obtained by using Hooke's law. The strain values ε_2 , and ε_3 are approximated using Vandewalle *et al.*, 2003.

$$\varepsilon_1 = \frac{\sigma_1}{E_c} \quad [\text{Eq. 3.7}]$$

$$\varepsilon_2 = \varepsilon_1 + 0.01\% \quad [\text{Eq. 3.8}]$$

$$\varepsilon_3 = 2.5\% \quad [\text{Eq. 3.9}]$$

The resulting approximation for the tensile stress-strain behaviour is shown in Figure 3.26.

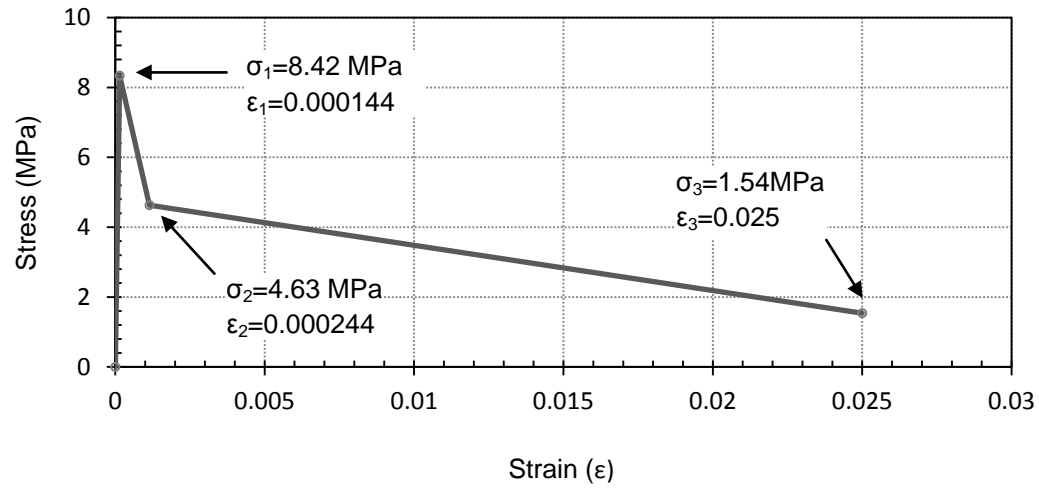


Figure 3.26 - Approximated SFRC tensile stress-strain behaviour

The uniaxial tensile stress-strain numerical input parameters are outlined in Table 3.7

Parameter	Input
σ_1 (MPa)	8.42
σ_2 (MPa)	4.63
σ_3 (MPa)	1.54
ϵ_1	0.000
ϵ_2	0.0001
ϵ_3	0.025

Table 3.7 - Tension stiffening stress-strain input parameters

3.7.4 Verification of Tensile Parameters

To validate the derived empirical tensile parameters, the experimental testing performed by TEC Services was modelled in ABAQUS, to attempt to reproduce the stress-displacement behaviour of the flexural beam tests. The model width, thickness and length were 150 mm, 150 mm and 500 mm, respectively. The loading and boundary conditions implemented in the finite element model replicated the experimental test setup as per ASTM C1609-10. At one end of the beam, a pin support was used by setting the allowable displacement, $U1=U2=U3=0$, limiting movement in all three directions. On the other end, a roller support was simulated with $U2=0$, preventing any vertical displacement (but allowing transverse movement). The loading was applied evenly on two surfaces spaced 150 mm apart as shown in Figure 3.27.

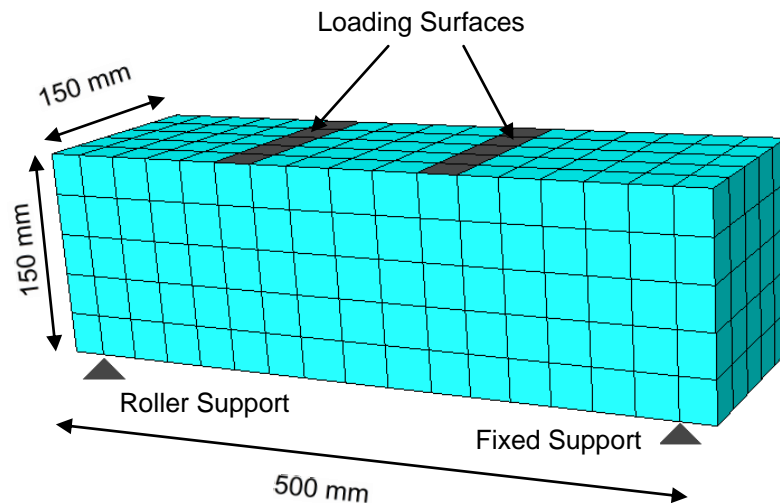
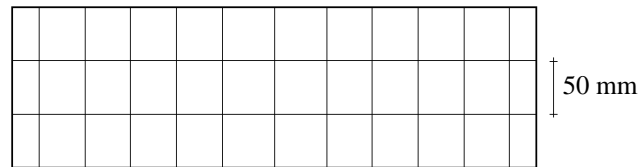


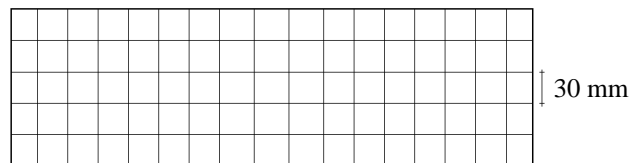
Figure 3.27 - Finite element beam test model (425 elements)

The main objective of performing the flexural beam tests was to characterize the tensile behaviour of the SFRC. It is desirable to accurately obtain the mechanical properties of SFRC from these tests and implement them into the ABAQUS finite element code to

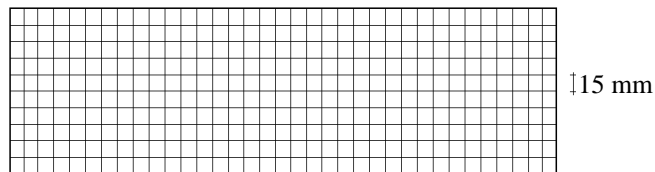
model the full-scale SFRC tunnel lining segments. However, for the derived material properties to be valid from one model to the other, a consistent mesh size must be used due to this element and crack width size dependency phenomenon. As such, a mesh sensitivity analysis was performed using three different sized meshes to ensure that the model was converging properly and that the mesh was appropriately refined. Furthermore, to minimize the computation time often associated with a highly refined mesh, local refinement was only attributed to the zone within the vicinity of the expected cracking location. Three-dimensional coarse, medium and fine meshes were produced having 108, 425, and 3500 elements respectively as shown in Figure 3.6.



Mesh (a) 108 elements



Mesh (b) 425 elements



Mesh (c) 3,500 elements

Figure 3.28 - Finite element model with (a) coarse, (b) medium, and (c) fine meshes

The stress-displacement response of the beam tests with the three mesh sizes is plotted in Figure 3.29. For all of the models, the initial response is linear-elastic, until a stress of approximately 7.5 MPa, where the specimen starts to experience strain hardening. Once the maximum stress of approximately 8.5 MPa is reached, the material begins to strain soften. It was found that the concrete damage plasticity model used in ABAQUS had some numerical convergence issues beyond a post-peak midspan deflection of approximately 33% of the total post-peak response, but still predicted the initial portion of the softening zone of the curve using the 30 mm mesh size.

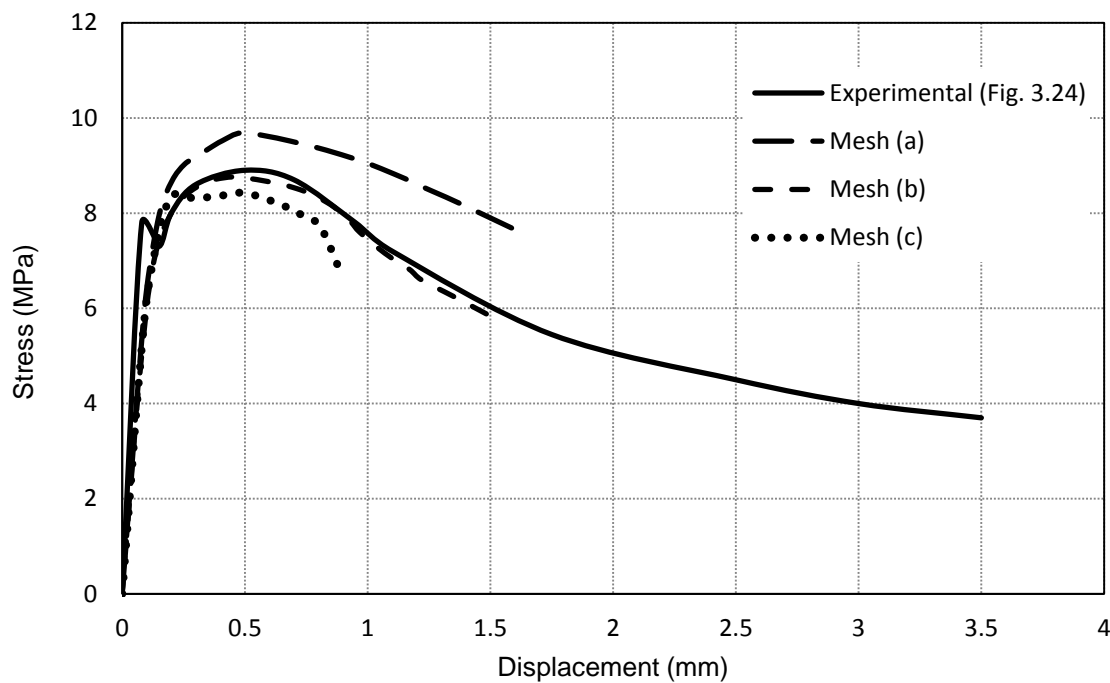


Figure 3.29 - Comparison of varying mesh size with experimental beam test behaviour

The finite element model using a medium sized mesh with 30 mm elements shows very good agreement with the experimental results and so it can be concluded that the uniaxial tensile stress-strain parameters approximated from Vandewalle *et al.*, (2003) are a good representation of the characteristic tensile properties of the SFRC. For modelling of the full-scale SFRC tunnelling lining segments, an equivalent mesh size of 30 mm (compared to flexure beam model) will be used and this assumes that the characteristic length scales of the crack in the beam (i.e. width) are approximately the same size as that in the full scale model.

3.7.5 Experimental Split Cylinder Tests

In addition to using flexural beam test methods to characterize the uniaxial tensile stress-strain properties of the steel fibre reinforced concrete, split cylinder tests were also carried out as per ASTM C496M-04 (Standard Test Method for Splitting Tensile Strength of Cylindrical Concrete Specimens) on three cores specimens retrieved at random locations of the key segment. The average splitting tensile strength was 7.96 MPa for the SFRC as summarized in Table 3.8. The average tensile strength determined from the core samples appears to be approximately 9% lower than that deduced from the flexural beam tests, suggesting lower strength concrete in the full-scale segments with respect to the flexure beams or differences between the two experimental approaches.

Specimens	Tensile strength (MPa)
T-1	7.66
T-2	8.06
T-3	7.37
Average	7.69

Table 3.8 - Tensile split cylinder strength results

3.8 Summary

A review of previous studies revealed that a uniaxial line load causing flexure represents one of the most critical loading cases for tunnel linings (Mashimo *et al.*, 2002) and proved to be a feasible method for evaluating the flexural response of full-scale tunnel lining segments. An experimental loading system was developed, comprising of a loading frame, two roller floor supports and a hydraulic actuator supported by two steel columns. The experimental method was used to study the load-displacement, load-strain, and crack propagation behaviour of steel fibre reinforced concrete tunnel liner segments subjected to uniaxial flexure loading conditions. Complementary standardized compressive and tensile cylinder and flexure beam tests were also performed to deduce the SFRC material properties in an attempt to replicate the segmented flexure tests with numerical methods. Additionally, computed tomography analysis techniques were employed to analyse and estimate the density fraction and fibre orientation of fibres in cored SFRC specimens. MicroView (3D image viewer software) was used in the visualization and analysis of the scanned cores, which used grey scale histogram profiles to capture the percentage of fibres in divided subsection. Finally, ABAQUS finite element models capable of analyzing the non-linear elasto-plastic behaviour of SFRC were investigated.

It was observed that the composition of SFRC has some variation in different locations of the tunnel segments. Hence a sufficient number of compressive and tensile tests must be done to accurately characterize the range of material properties. Additionally, it was of interest to numerically study the post-peak performance of SFRC tunnel lining segments and the concrete damage plasticity model in ABAQUS proved to be most appropriate model to do so, as the concrete smeared cracking model failed to converge past the peak

loading. Moreover, from uniaxial cylinder compression tests and flexural beam tests, the stress-strain relationship can be established and utilized as input parameters in numerical analyses. From the finite element analysis of the beam tests, it was found that the mesh size was important. Thus an identical mesh size will be needed to be used for the full-scale segment modelling, to ensure the deduced tensile properties of the material are valid.

EXPERIMENTAL RESULTS

4.1 Introduction

In this chapter, seven simply supported flexural tests performed on SFRC tunnel lining segments are described. The first test, SFRC-P, was a trial test to optimize the testing methodology and logistics. From this trial test it was expected to verify the loading rate, strain and displacement response from the test segments and the failure point of the segment. The following six flexural tests and supporting laboratory work had primary objectives: *(i)* to estimate the flexural capacity of SFRC tunnel linings by means of a three point bending test, *(ii)* to monitor the crack propagation and attempt to relate the loading applied to the crack mouth opening displacement magnitude, *(iii)* to characterize the toughness indices of the SFRC segment and compare the toughness and post-peak strain softening of the SFRC segments to other SFRC and plain concrete specimens, *(iv)* to use computed tomography scan imaging as a non-destructive analysis tool to determine internal steel fibre content and orientation and *(v)* to provide analysis and interpretation of the observed results.

4.2 Load-Deflection Response

4.2.1 Pilot Test (SFRC-P)

The first test, SFRC-P, was a pilot test done to optimize the testing methodology and logistics. From this trial test, the loading rate, strain and displacement responses from the test segments were verified. A load-controlled loading was used for the pilot test with a loading rate of rate of 5 kN/min. As seen in Figure 4.1, the load-displacement reaction followed a linear response up to an applied load of approximately 60 kN. The specimen began to yield from this point until it reached a maximum carrying capacity of 112 kN, failing abruptly. SFRC is known for its post-peak ductility and enhanced crack control, and it was proposed that the loading rate chosen was potentially too high to capture the post-peak softening branch. To achieve the desired full response of the segments, it was decided to change the loading to a displacement-controlled loading for the remainder of the tests.

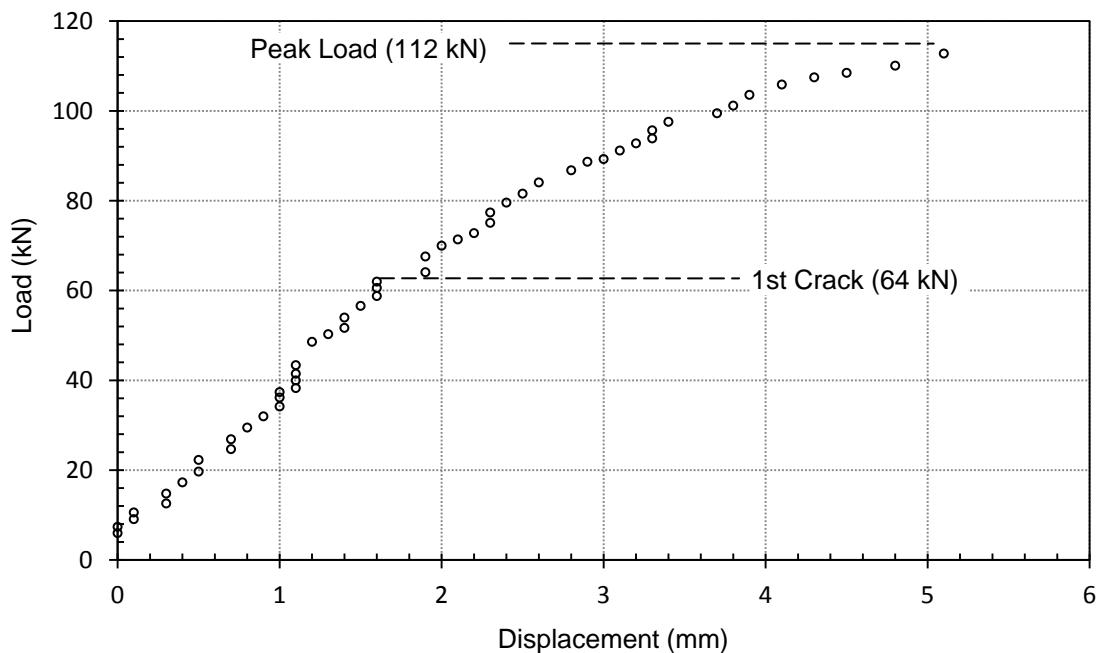
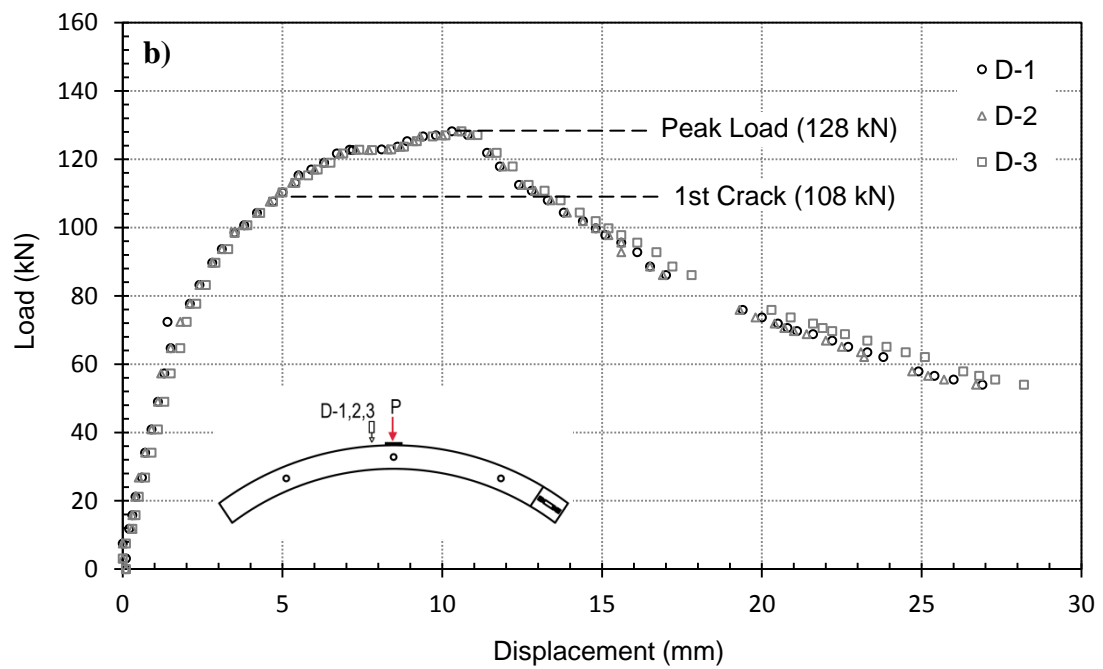
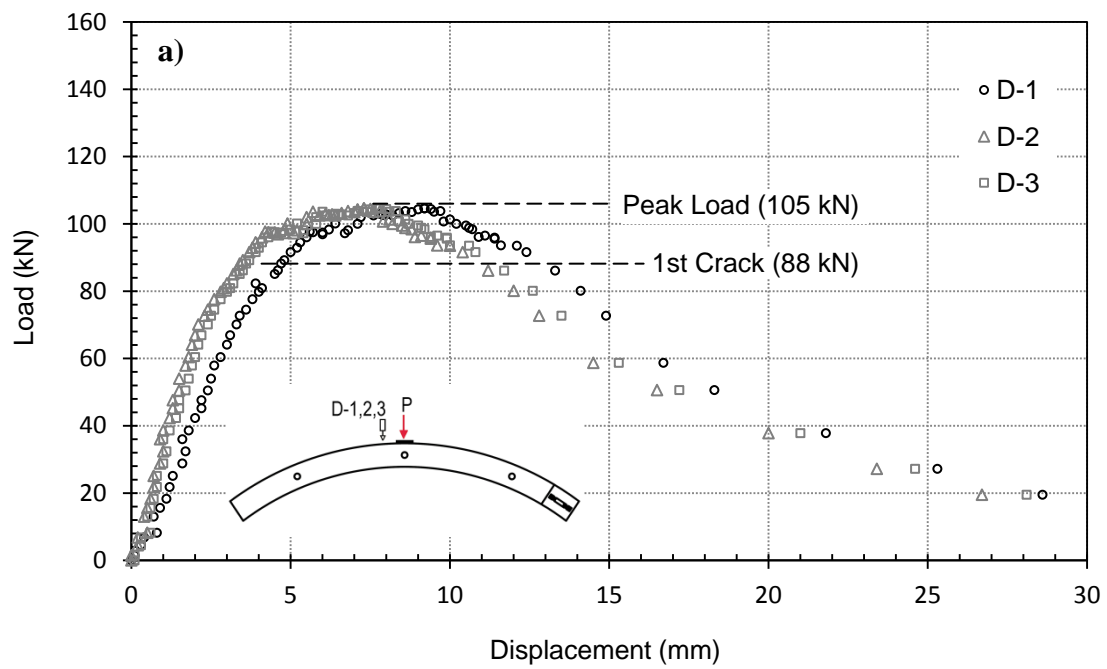
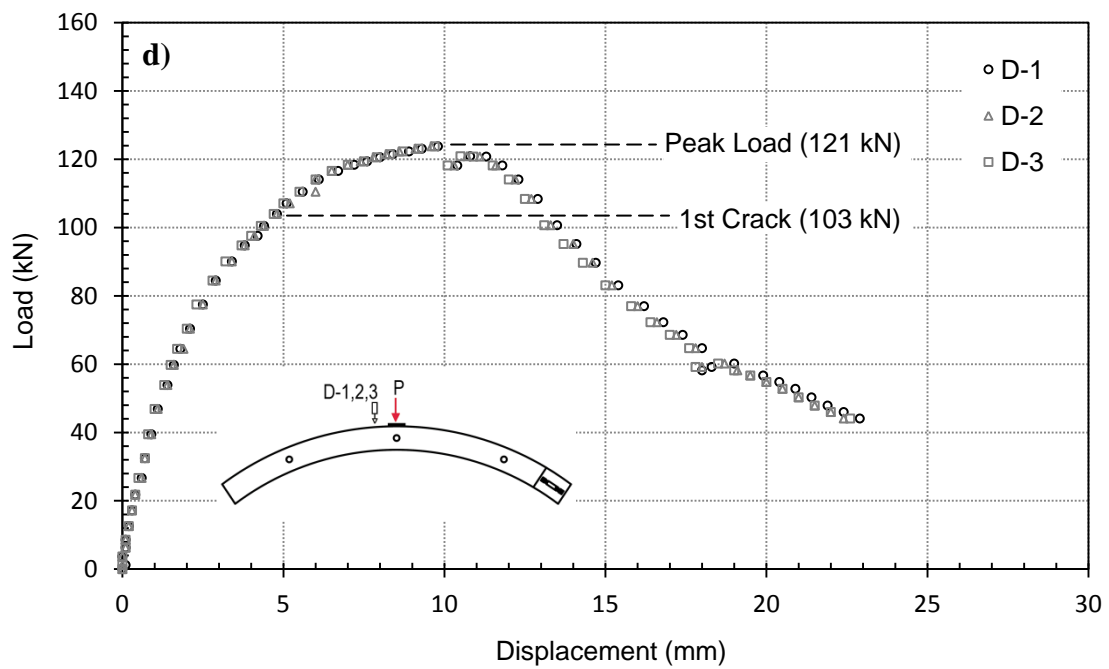
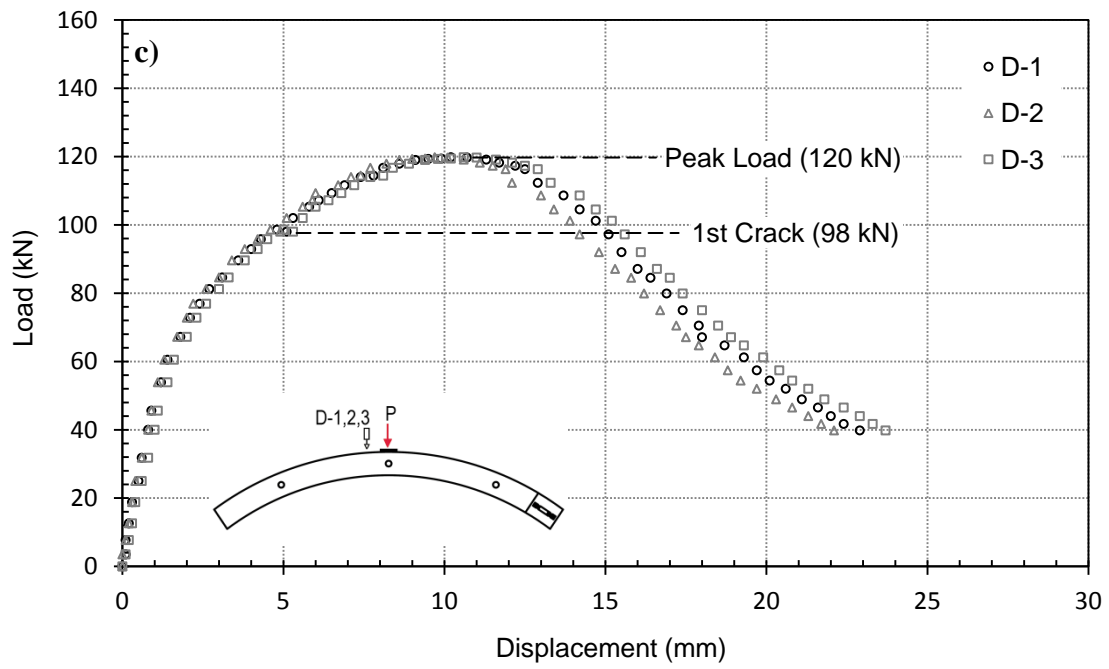


Figure 4.1 - Load-displacement response of pilot test SFRC-P

4.2.2 Tests SFRC-1 to SFRC-6

The load vs. midspan displacement diagrams of the flexural bending tests (SFRC-1 to -6) are presented in Figure 4.2(a) to Figure 4.2(f) for the central midspan LVDTs (D-1 to D-3). There is good agreement between LVDTs D-1 to D-3, which show very similar displacements, illustrating that no significant torsion was occurring. Each test illustrates an initial elastic behaviour similar to that of plain concrete. The displacements increased linearly with applied load as the segments began to yield and started deforming plastically. With sufficient plastic deformation, a hairline crack developed near the midspan of the segments, where stresses were highest. The material experienced a hardening effect, ultimately reaching a maximum compressive stress, followed by a softening branch. Previous research (De Waal, 1999; Banthia, 2001; Poh *et al.*, 2009) indicates that when the initial crack developed, the fibres begin to tense up as the concrete experiences non-linear strain hardening. Once the peak load was reached, the stress is supported by the fibres, which act as crack arresters, bridging the crack formation. The matrix was held together by the fibres as a long softening branch continued.





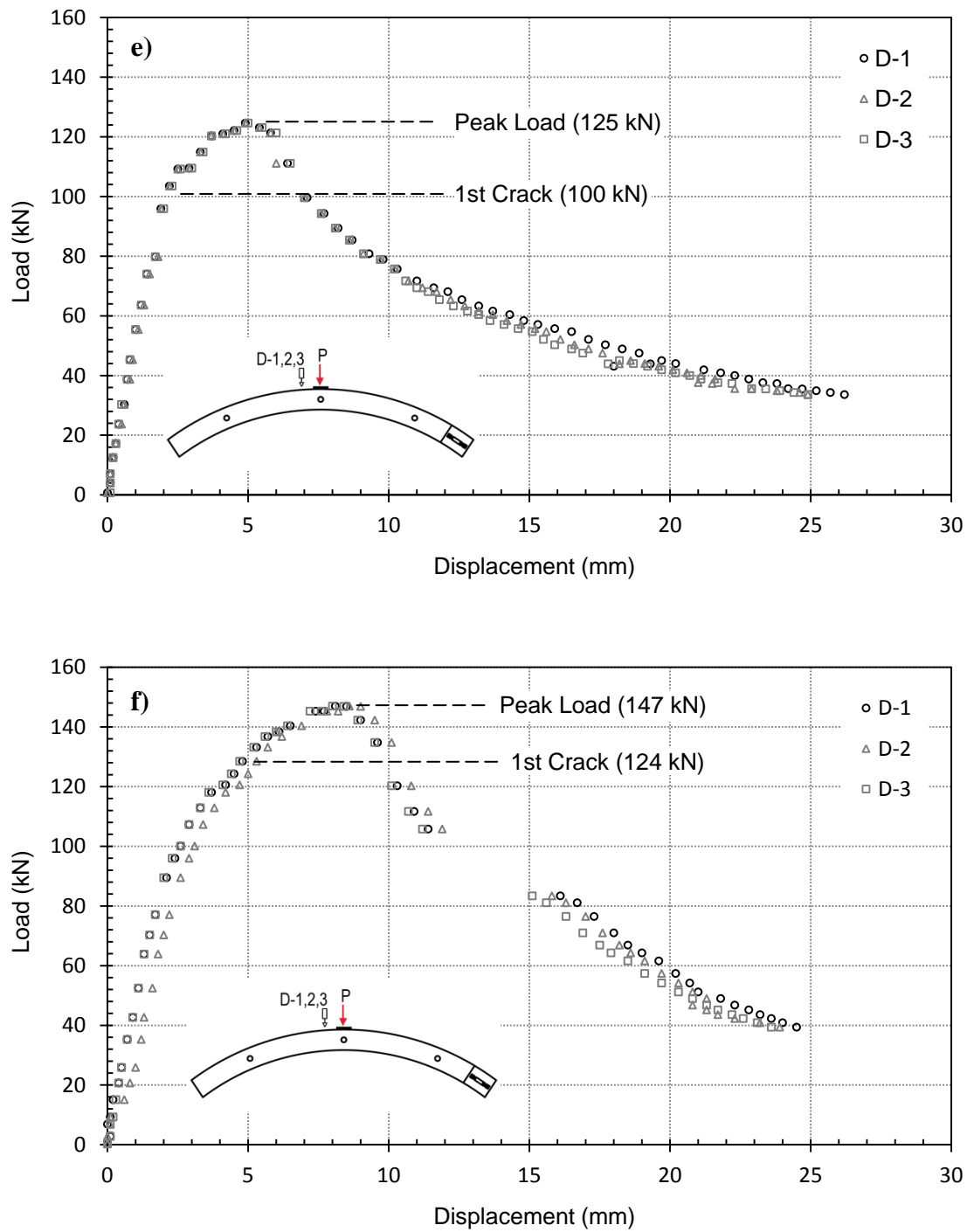


Figure 4.2 - Load-vertical deflection curves of the segments

a) SFRC-1, b) SFRC-2, c) SFRC-3, d) SFRC-4, e) SFRC-5, f) SFRC-6

The load vs. midspan deflection response of each test is summarized and compared in Figure 4.3, to illustrate the behavioural variations. Each segment experienced a similar type of behaviour; however there was a degree of variation with respect to first crack load and peak load. SFRC-1 experienced the lowest failure load of 105 kN with a corresponding 1st crack loading of 88 kN. SFRC-6 withstood the highest loading of 147 kN with a corresponding 1st crack load of 124 kN. A 40% variation in peak loading was present between SFRC-1 and SFRC-6. The 1st crack load to peak load ratio of all six tests was quite consistent, having a range of 80 – 85% of the peak load. It is significantly higher than that of conventionally reinforced concrete and this is thought to be due to the fibre crack arresting properties (Caratelli *et al.*, 2011; Moccichino *et al.*, 2006)

The average and standard deviation of the first crack load, displacement at first crack load, peak load, and displacement at peak load is summarized in Table 4.1 below. Generally speaking, an approximate variation of 10% is present with respect to the first crack load and peak load, and 19% with respect to the displacement at first crack load and displacement at peak load. From the average and standard deviation data, test SFRC-4 seems to approximately represent the average behaviour of the segments and is chosen as a representative test in future analyses.

	First Crack Load (kN)	Displacement at First Crack Load (mm)	Peak Load (kN)	Displacement at Peak Load (mm)
SFRC-1	88	4.6	105	9.2
SFRC-2	108	4.7	128	10.3
SFRC-3	98	4.7	120	10.2
SFRC-4	103	4.6	121	8.4
SFRC-5	100	2.4	125	5.4
SFRC-6	124	4.4	147	8.0
Average	103.50	4.23	124.33	8.58
Standard Deviation	10.98	0.83	12.46	1.66
S.D. / AVG.	10.6%	19.6%	10.1%	19.3%

Table 4.1 - Average and standard deviation of segment flexure test behaviour

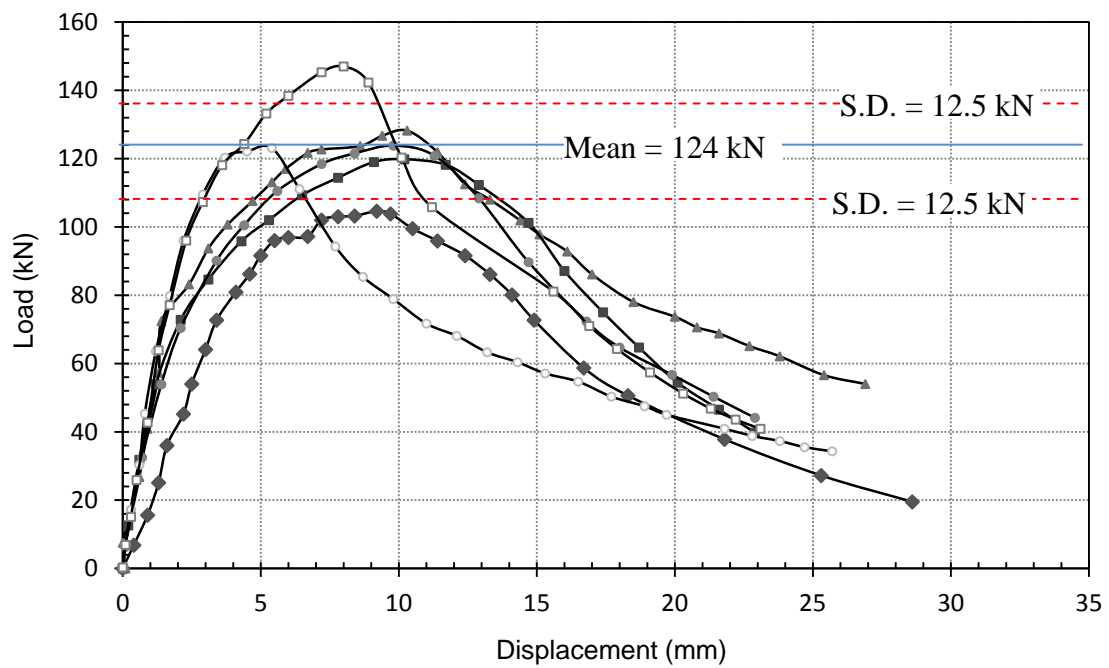
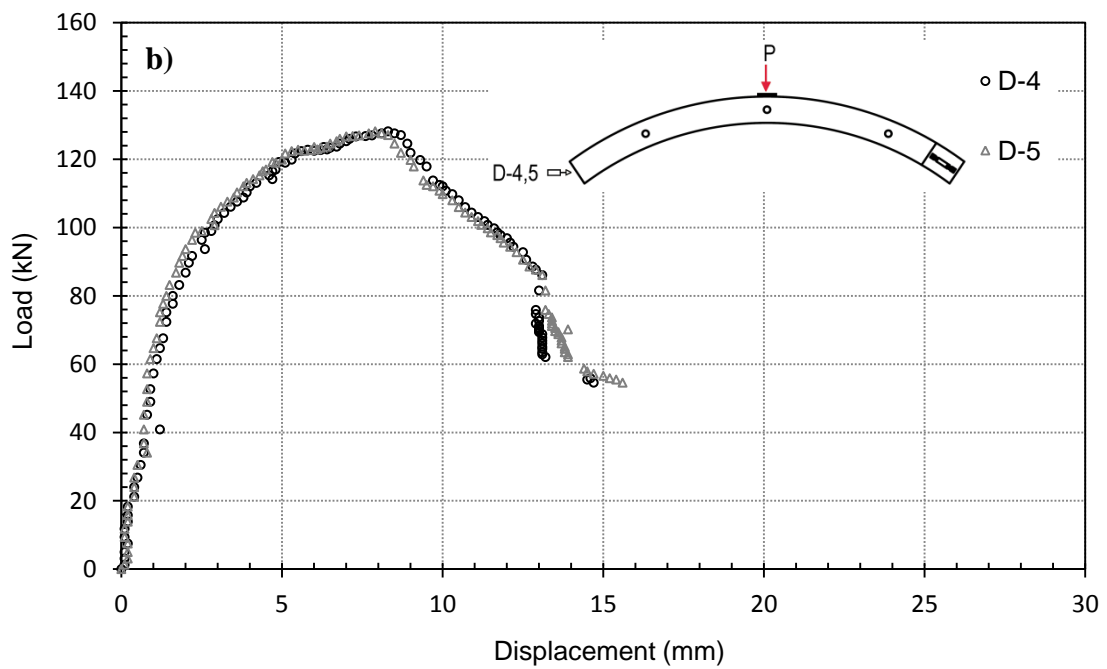
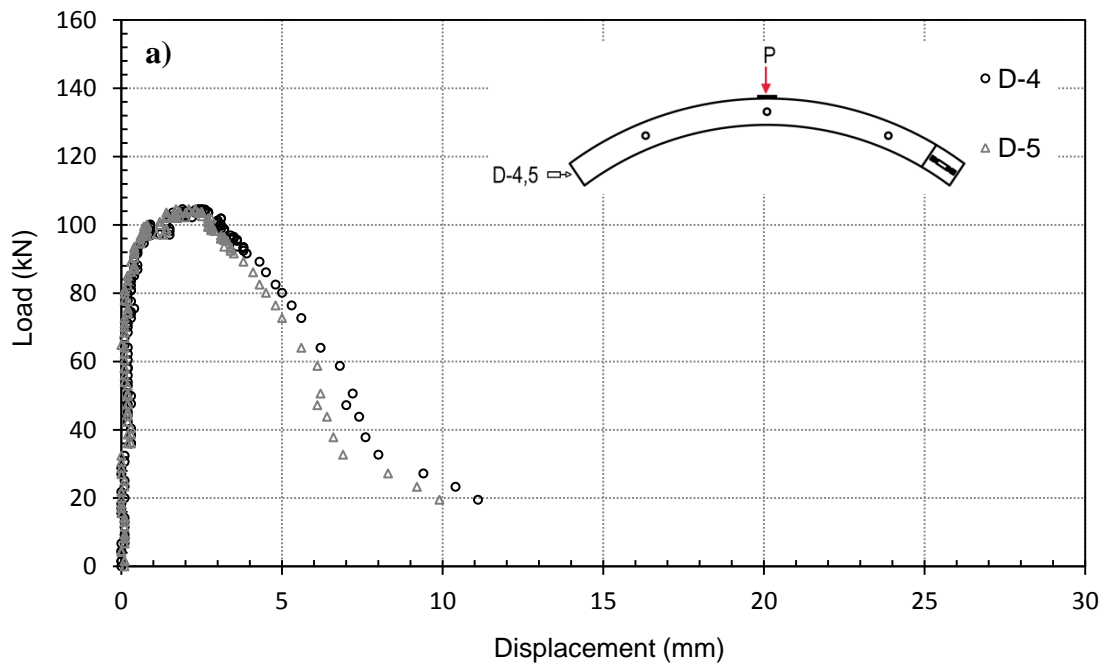
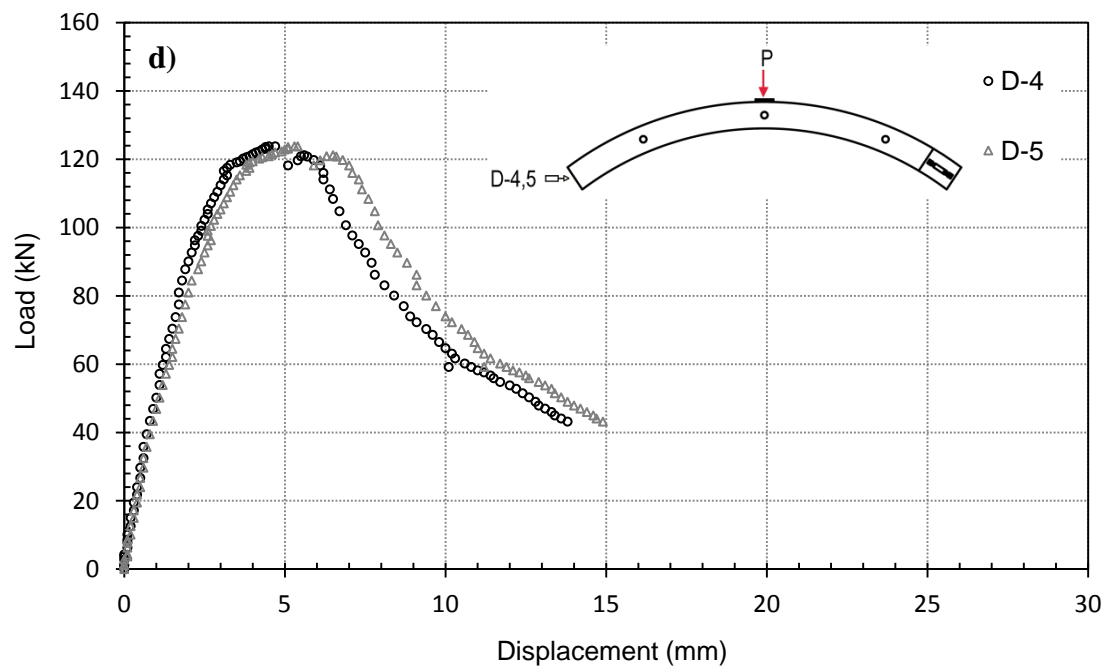
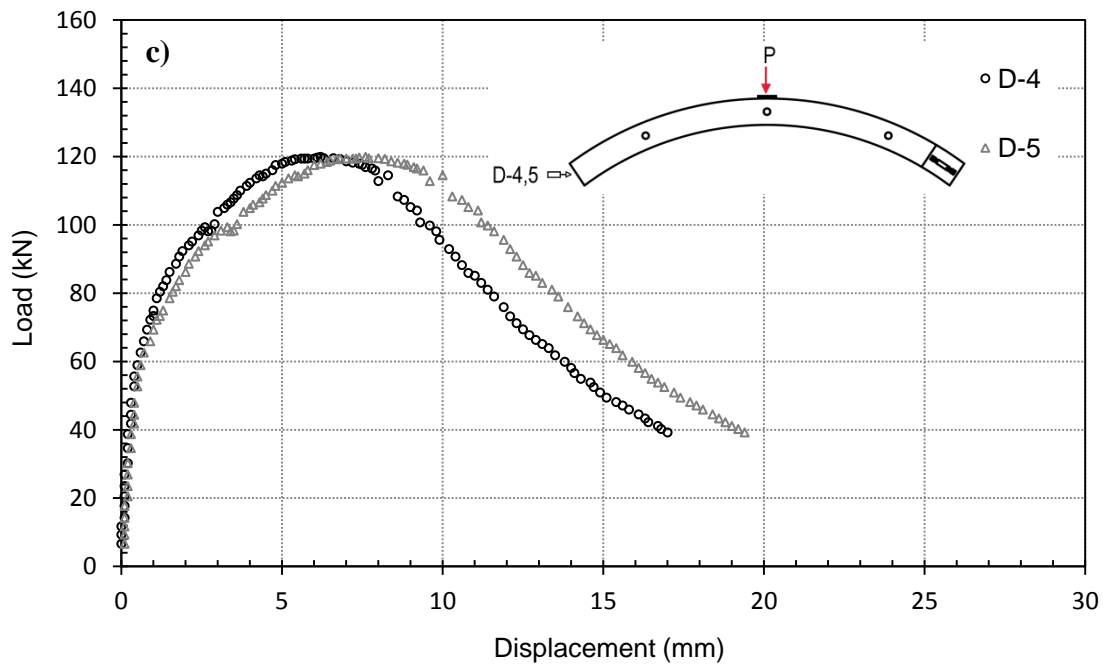


Figure 4.3 - A vertical displacement-load comparison for LVDT D-1 (central midspan)

Furthermore, it was observed that for each test, only one end of the segment moved horizontally; even though both ends were free to translate. Displacement gauges D-6 and D-7 experienced nearly zero movement throughout the test. This phenomenon can be attributed due to slight irregularities of the support reaction frames and the segments. For each test, the support of the translating end was that with the least resistance and therefore experienced movement alone. For the purpose of further analysis, the “fixed” end is assumed to have a pin connection. Figure 4.4 shows the horizontal displacement for two displacement gauges, D-4 and D-5. The similarity in displacement behaviour demonstrates that the segment was loaded symmetrically. Accordingly, it was confirmed that the testing methodology developed and the results obtained can be utilized as a benchmark to evaluate the load-carrying capacity. It is noted that for test SFRC-6, the segment moved slightly out of plane during loading due to improper placement of the lining on the support frame and may account for the higher flexural strength observed. As a result, gauge D-5 experiences higher translations compared to D-4 at a post-peak loading of approximately 80 kN.





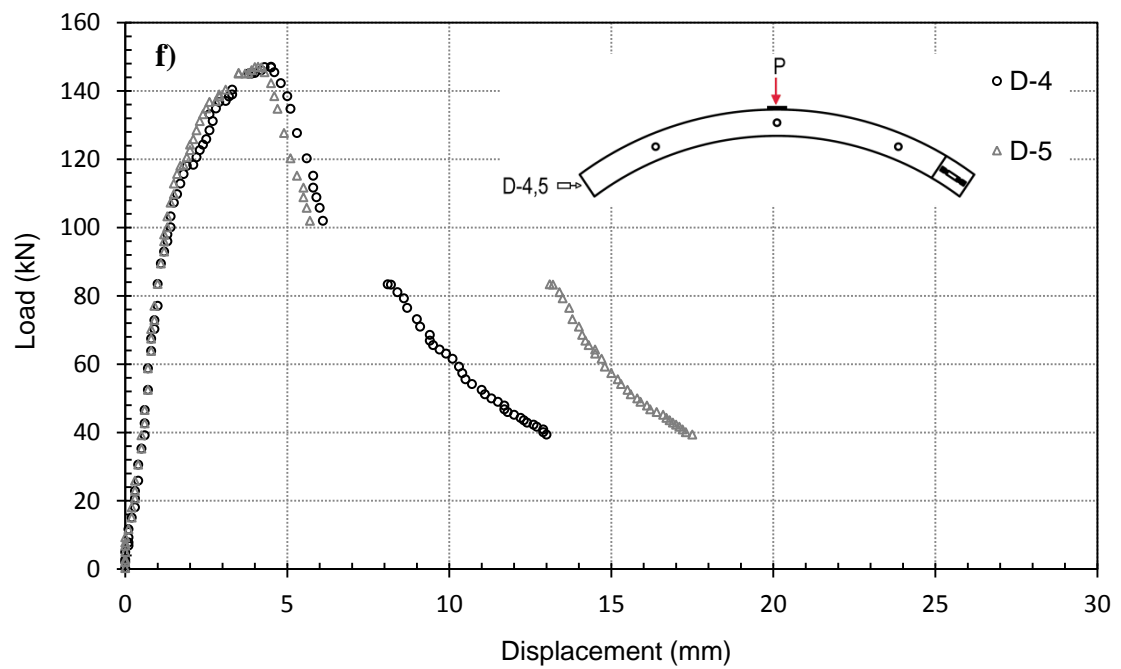
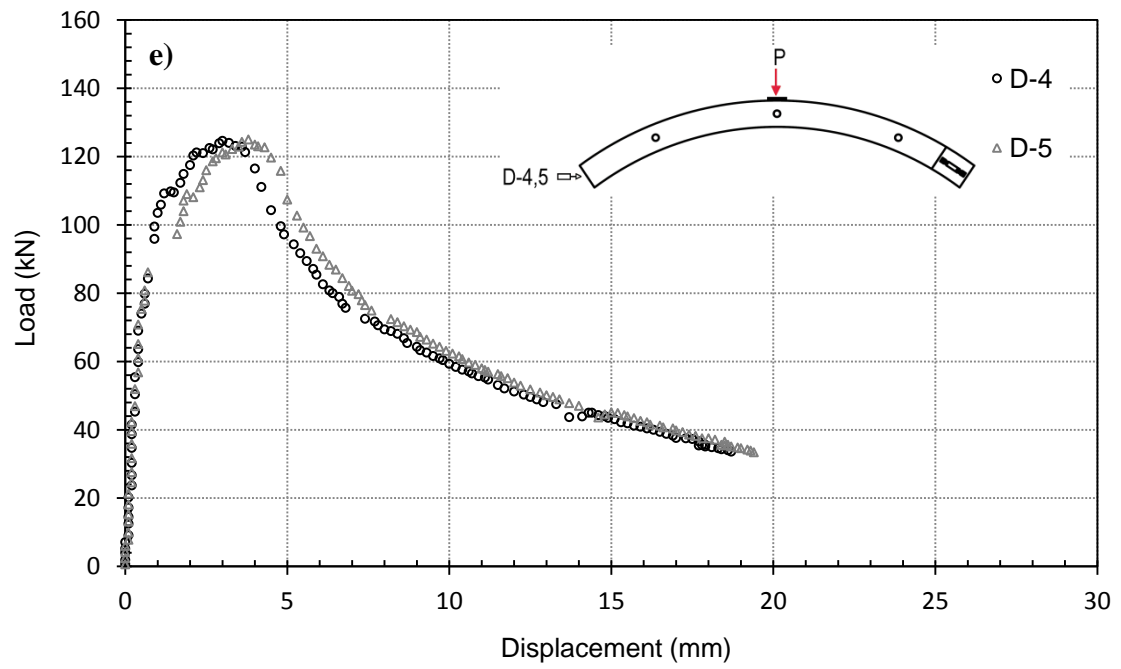


Figure 4.4 - Load-transverse deflection curves of the segments

a), SFRC-1, b) SFRC-2, c) SFRC-3, d) SFRC-4, e) SFRC-5, f) SFRC-6

4.3 Load-Strain Response

4.3.1 Pilot Test (SFRC-P)

The pilot test had two strain gauges mounted on the intrados surface of the segment to measure the tensile strain. Shortly after loading (approximately 50 kN), the gauges experienced very high strains, exceeding the strain capacity and provoking immediate failure of the strain gauges at a midspan deflection of approximately 1.3 mm (22.6 % of total deflection). Consequently, only the elastic tensile behaviour was captured and no useable data beyond that point was produced. Hence the remainder of the tests only consisted of six gauges on the extrados (compressive face).

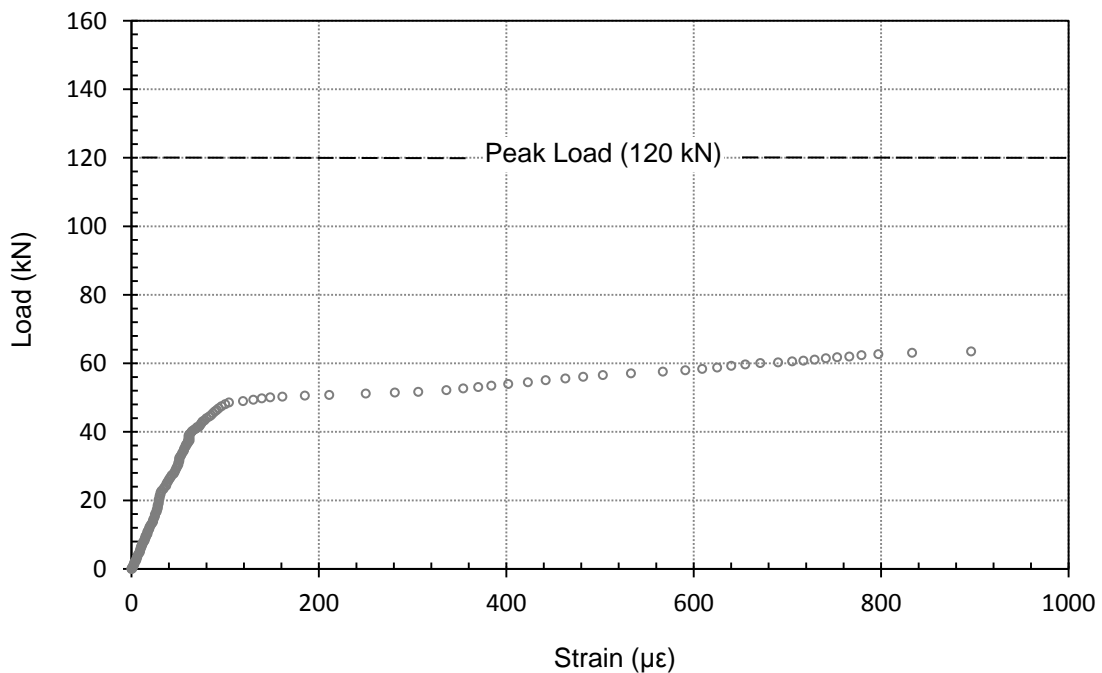
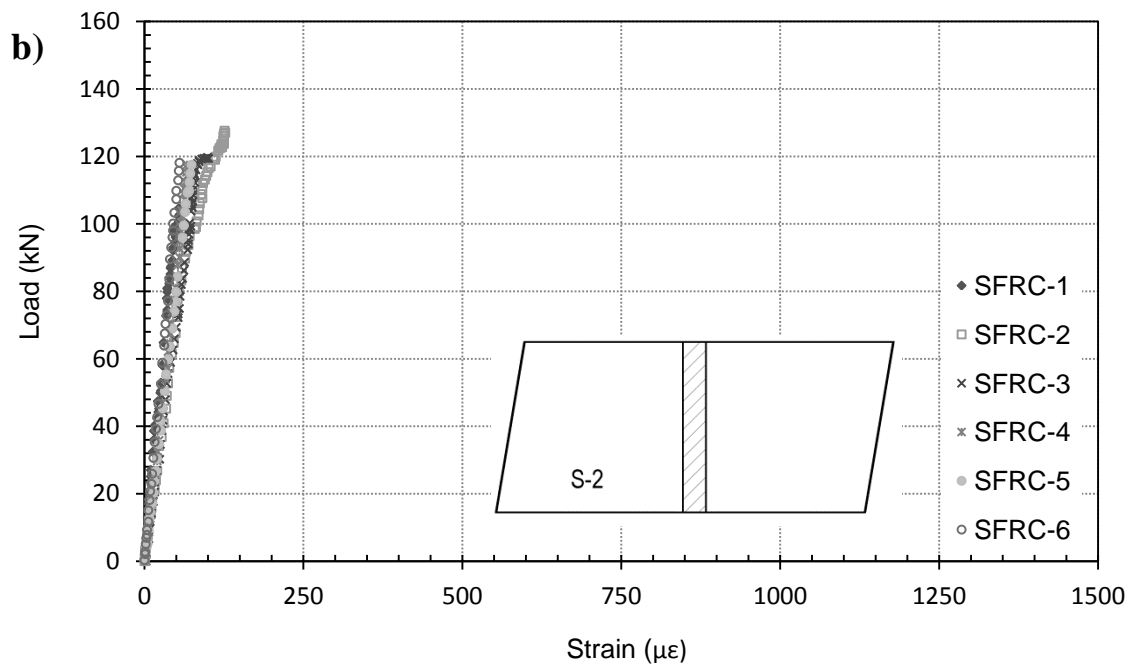
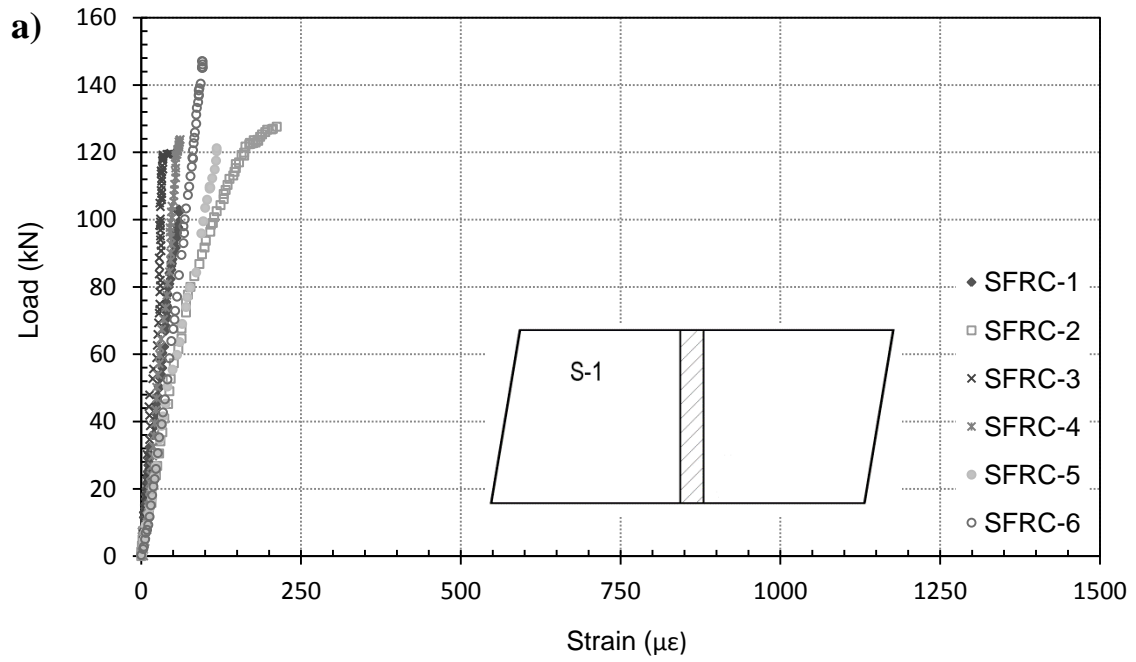


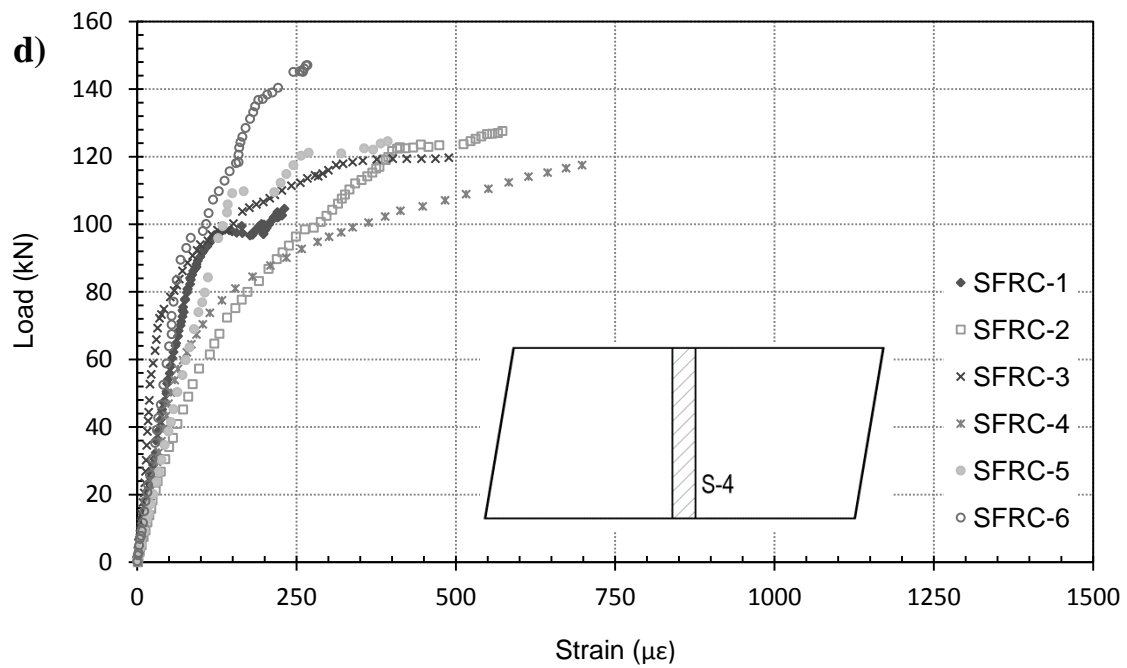
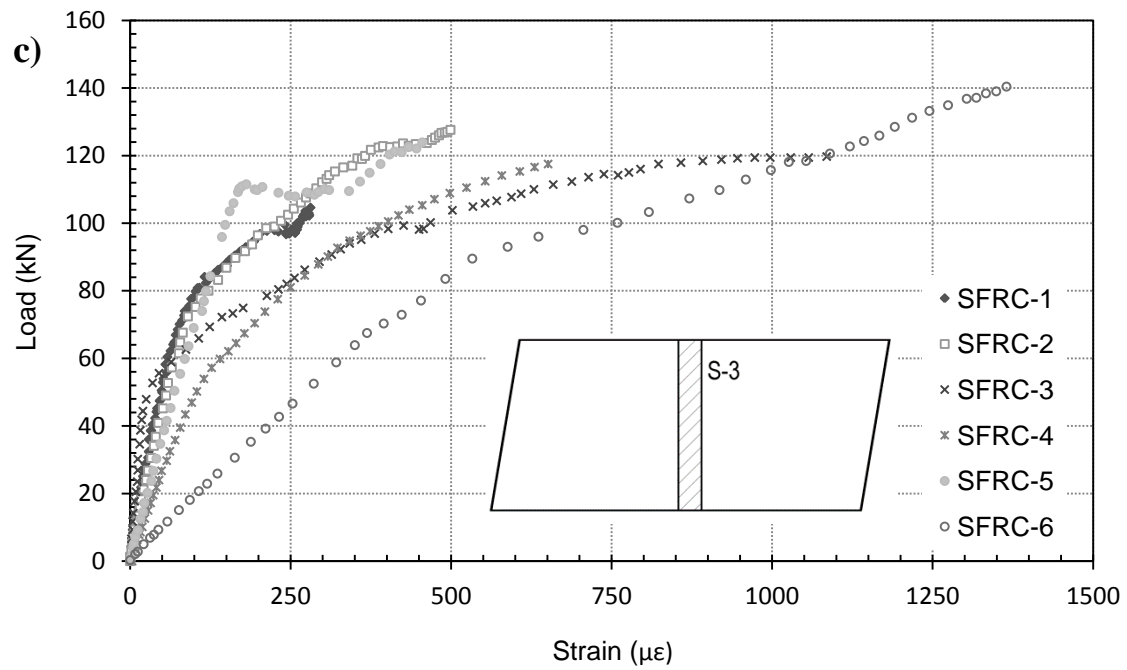
Figure 4.5 - Pilot test (SFRC-P) tensile strain vs. load

4.3.2 Tests SFRC-1 to SFRC-6

The load vs. strain data for test SFRC-1 to SFRC-6 is presented in Figure 4.6(a) to Figure 4.6(f). Strains measured at S-1, S-2, S-5, and S-6 showed very good consistency amongst all six tests. Gauges S-1 and S-5 in test SFRC-2, experienced slightly higher strain readings after a loading of 120 kN. Symmetrically, gauges S-1, S-5 and S-2,S-6 provide near identical readings, illustrating that uniform load distribution was applied and that stresses were distributed evenly within the segment.

Gauges S-3 and S-4 were located at the midspan of the segment and experienced much higher compressive strains due to the nature of the loading. Generally, the strain reading show fairly good consistency experiencing an average strain of 500 $\mu\epsilon$. Test SFRC-6 shows quite a bit of variability between two strain readings and this can be attributed to the possible uneven loading.





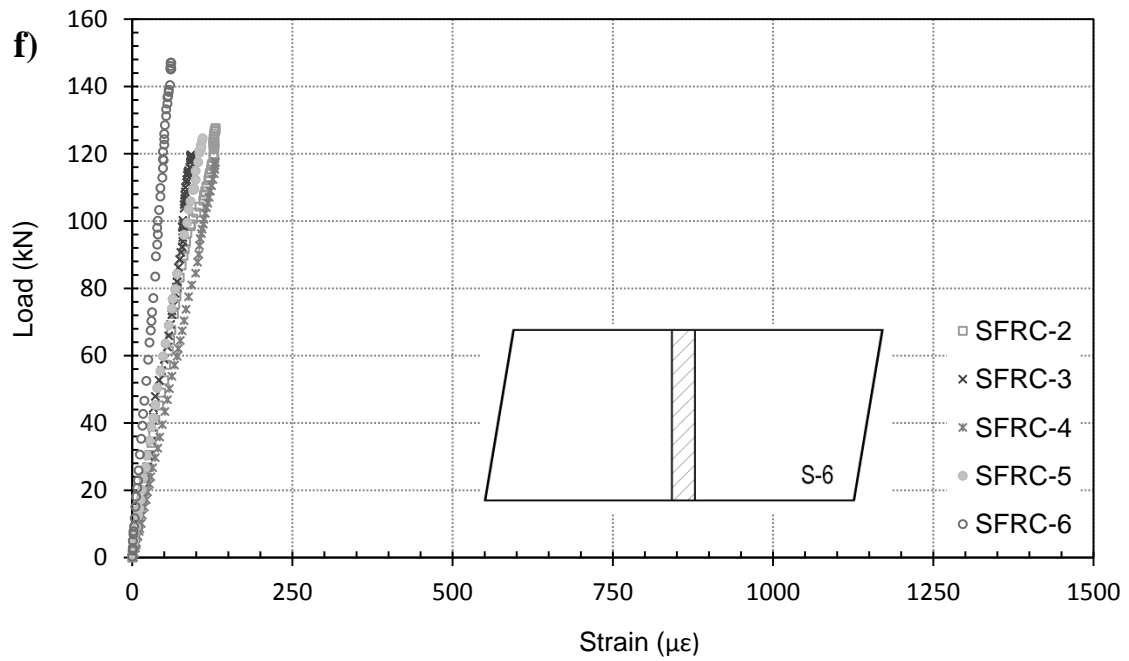
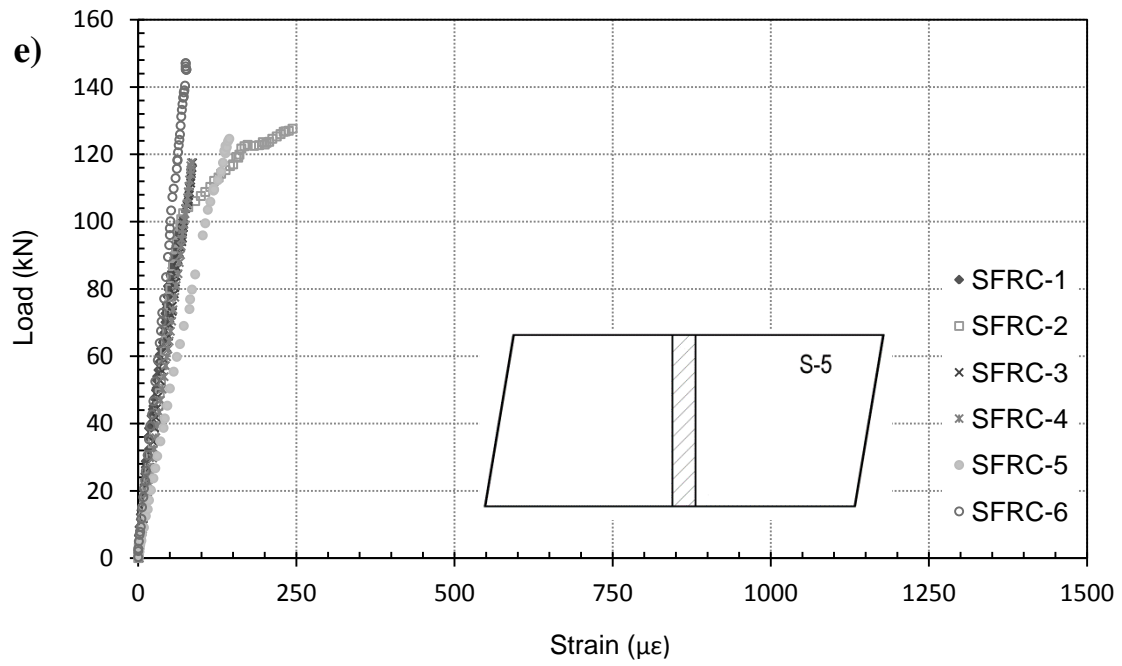


Figure 4.6 - Load-strain curves of the segments

a) S-1, b) S-2, c) S-3, d) S-4, e) S-5, f) S-6

4.4 Crack Propagation Analysis

The cracking pattern and crack propagation monitored for tests SFRC-5 and SFRC-6 is described in this section. Photographs of the crack movement during test SFRC-5 are presented in Figure 4.7 (a) to Figure 4.7 (f). At a loading of approximately 100 kN, a single hairline crack forms in the midspan of the segment and propagates upward in a near vertical line as the load is increased. The load vs. displacement curve with the corresponding images is shown in Figure 4.8.

The load vs. displacement and subsequent images for SFRC-6 are shown in Figure 4.9 and Figure 4.10, respectively. The segment lining for SFRC-6 withstood a peak load of approximately 22 kN higher than that of SFRC-5. Consequently, the first hairline crack is observed at a slightly higher load level of 124 kN. The crack originates at a distance of 10 cm away from the midspan of the segment and propagates inward at an angle of 60°. It is postulated that a lower percentage of fibres is distributed in this region, causing the crack to originate there.

The first crack is observed at 79% and 84 % of the peak load for SFRC-5 and SFRC-6, respectively. The delay in cracking can be attributed to the SFRC crack arresting properties. During loading, the steel fibres provide superior resistance to cracking and crack propagation. Once extensive cracking develops, the fibres hold the concrete matrix together, possessing increased extensibility and tensile strength (both at first and ultimate crack). A large strain softening zone post peak is typical in SFRC, which results in strong post cracking ductility (Burgers, 2006).

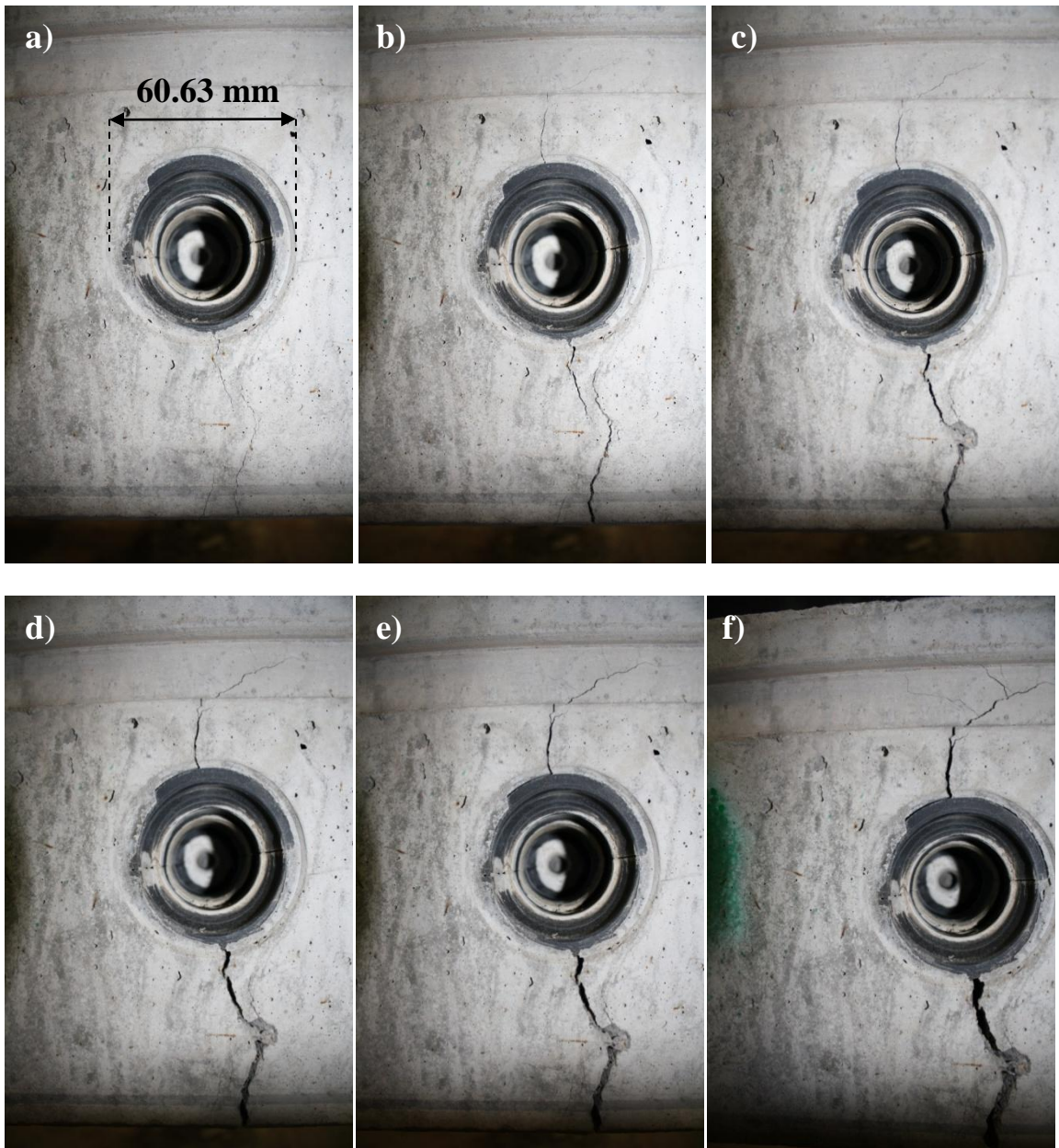


Figure 4.7 - Crack width propagation at midspan load deflection (SFRC-5)

a) 4.2mm, b) 6.7mm, c) 9mm, d) 12.5mm, e) 16.5mm, f) 24.4mm

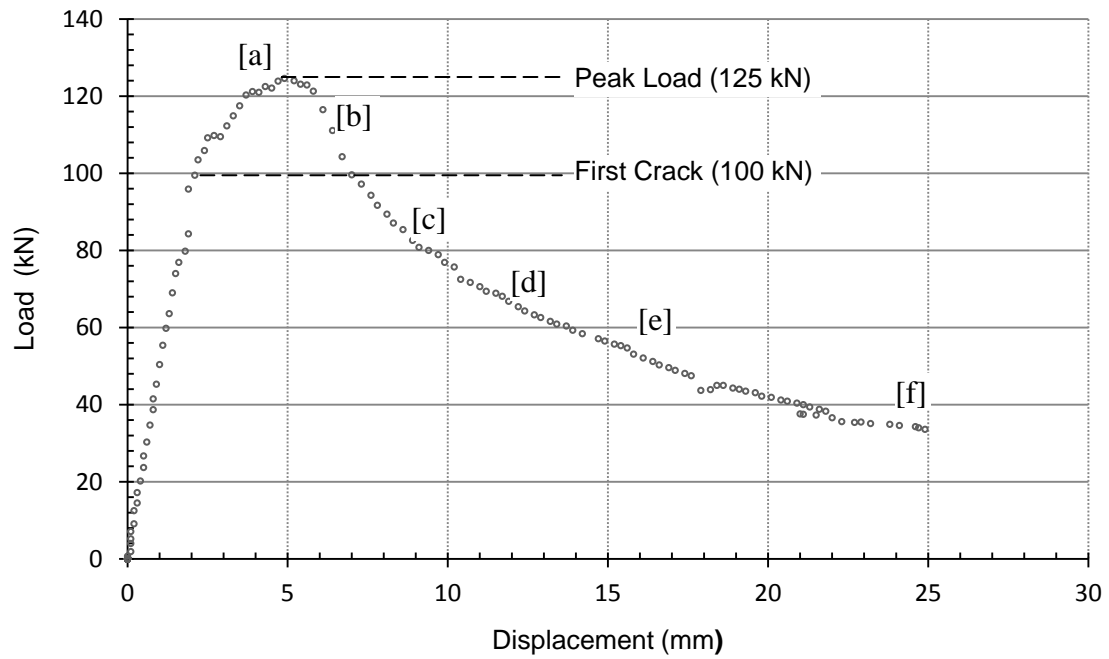


Figure 4.8 - Crack width at specified load-displacement (SFRC-5)

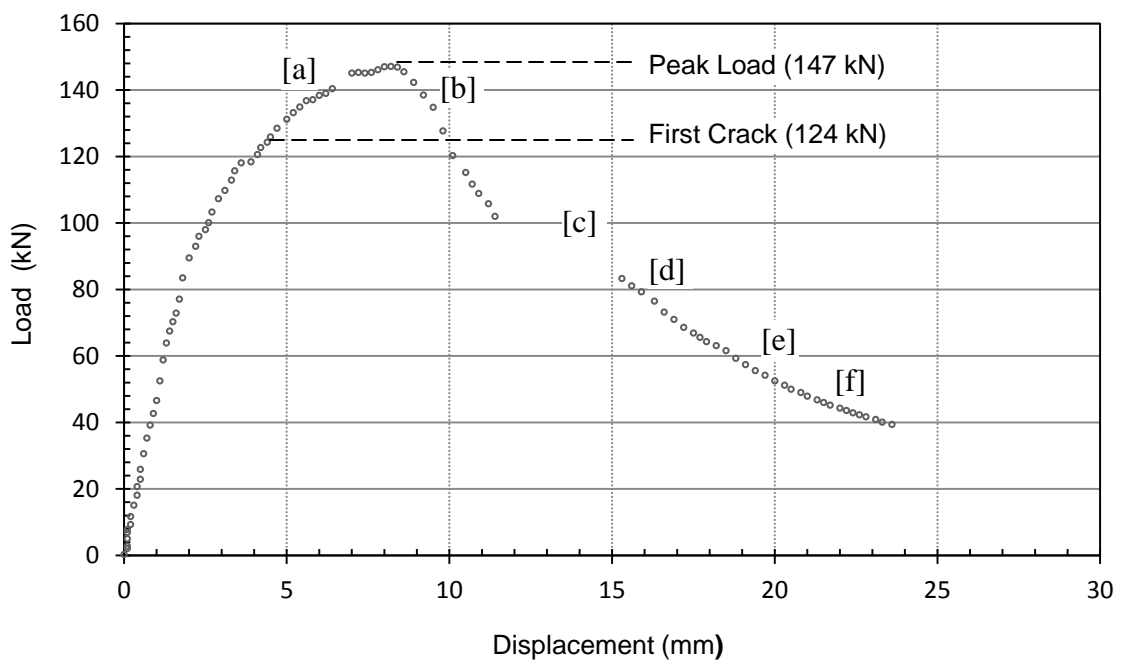


Figure 4.9 - Crack width at specified load-displacement (SFRC-6)

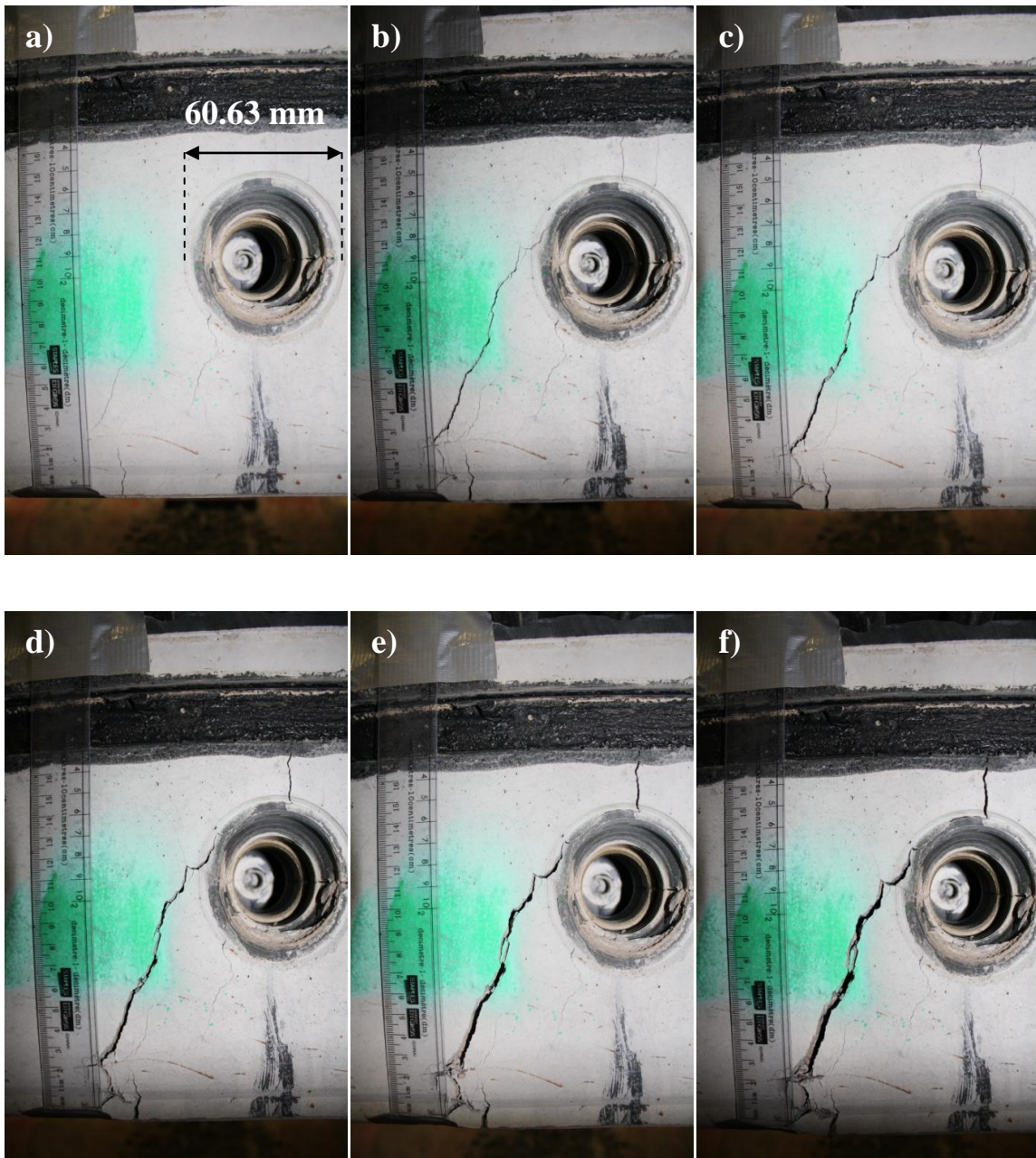


Figure 4.10 - Crack width propagation at midspan load deflection (SFRC-6)

a) 6.1mm, b) 9.8mm, c) 14.8mm, d) 16.6mm, e) 20.2mm, f) 23.1mm

Using Image J software analysis, the crack mouth opening displacement (CMOD) was determined at midspan displacements throughout the duration of both SFRC-5 and SFRC-6. The midspan downward displacement vs. the crack width is plotted in Figure 4.11 and presents an approximately linear correlation. Due to its higher load-carrying capacity, the cracking of segment SFRC-6 initiates at a larger displacement than that of segment SFRC-5.

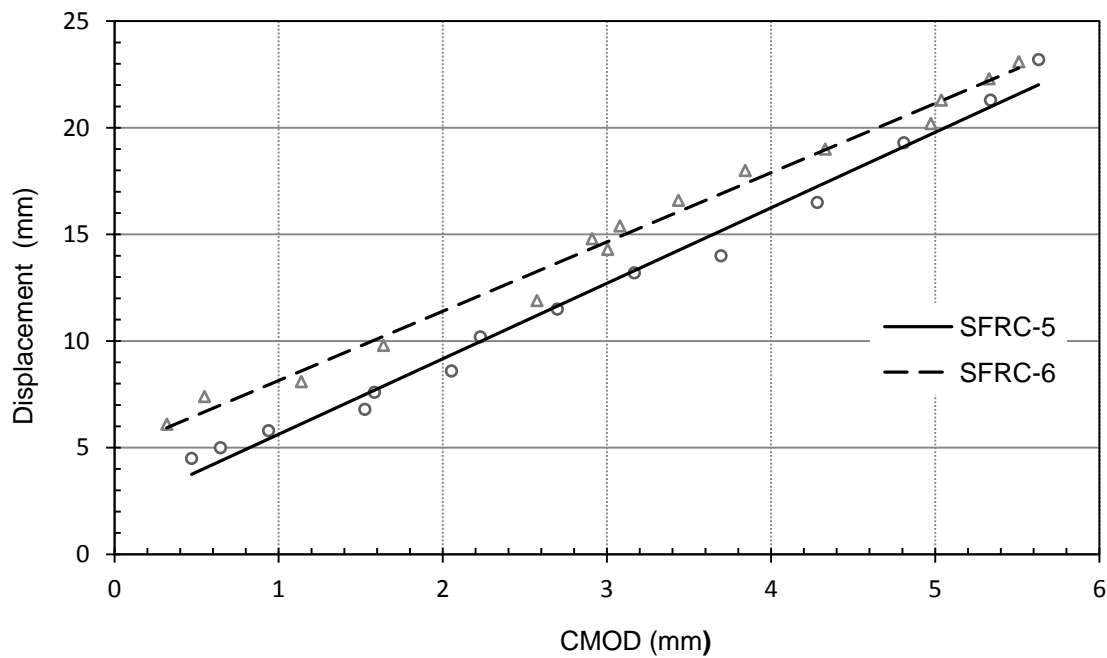


Figure 4.11 - CMOD vs. midspan deflection (SFRC-5 & 6)

4.5 Fracture Energy and Toughness Characterization

Toughness is defined as a material's ability to absorb energy, and deform plastically without fracturing. The toughness and post-peak strain softening of the concrete can be characterized by toughness indices I_5 and I_{10} following RILEM TC162-TDF (2000). The indices I_5 and I_{10} are calculated as ratios of the area under the load-crack mouth opening displacement curve up to 5, and 10 times the CMOD corresponding to its first peak load and divided by the area under the load-CMOD curve up to the CMOD with respect to the first peak load (Chen *et al.*, 2011). The toughness indices can also be determined from the load-deflection response, although previous studies supported several advantages of utilizing the load-CMOD response as a basis for toughness measurement (i.e. it is difficult to find the point of the limit of proportionality from the load deflection curves; Gopalaratnam *et al.*, 1991; Bryars *et al.*, 1994; Gopalaratnam and Gettu 1995; Barr *et al.*, 1995; Barr *et al.*, 1996).

Rather than using the CMOD to characterize the fracture energy of SFRC which is structure dependent (i.e. size, shape of specimen), the toughness indices are normalized to give an accurate representation of the effect of fiber reinforcement in enhancing the crack growth resistance of cementitious composites (Chen *et al.*, 2011).

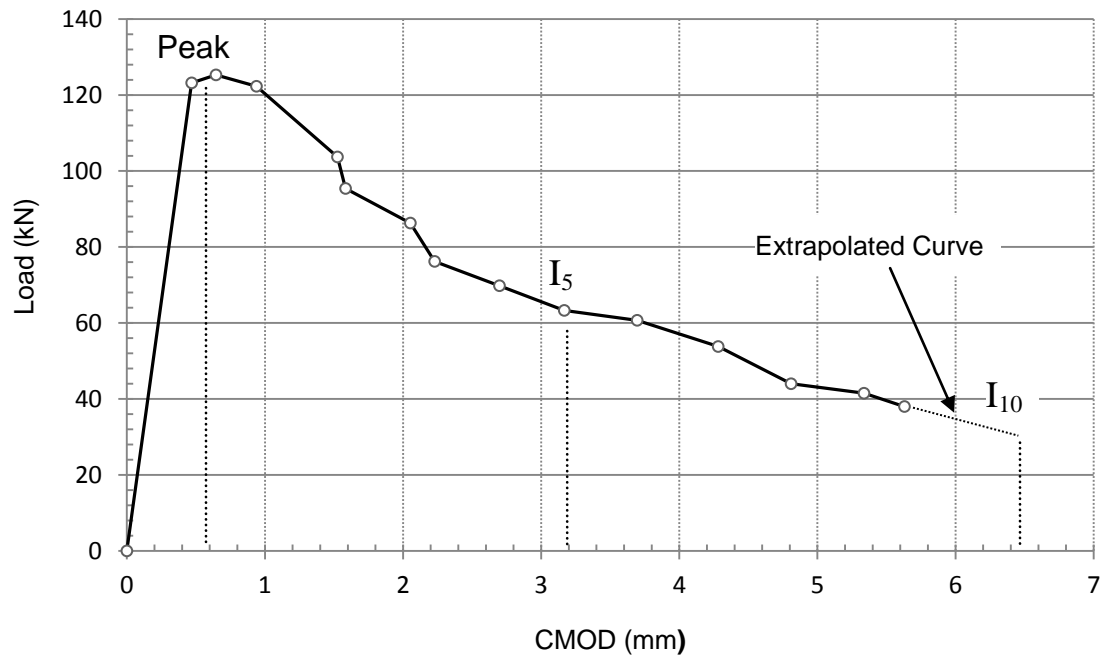


Figure 4.12 - Load-CMOD curve with toughness indices points (SFRC-5)

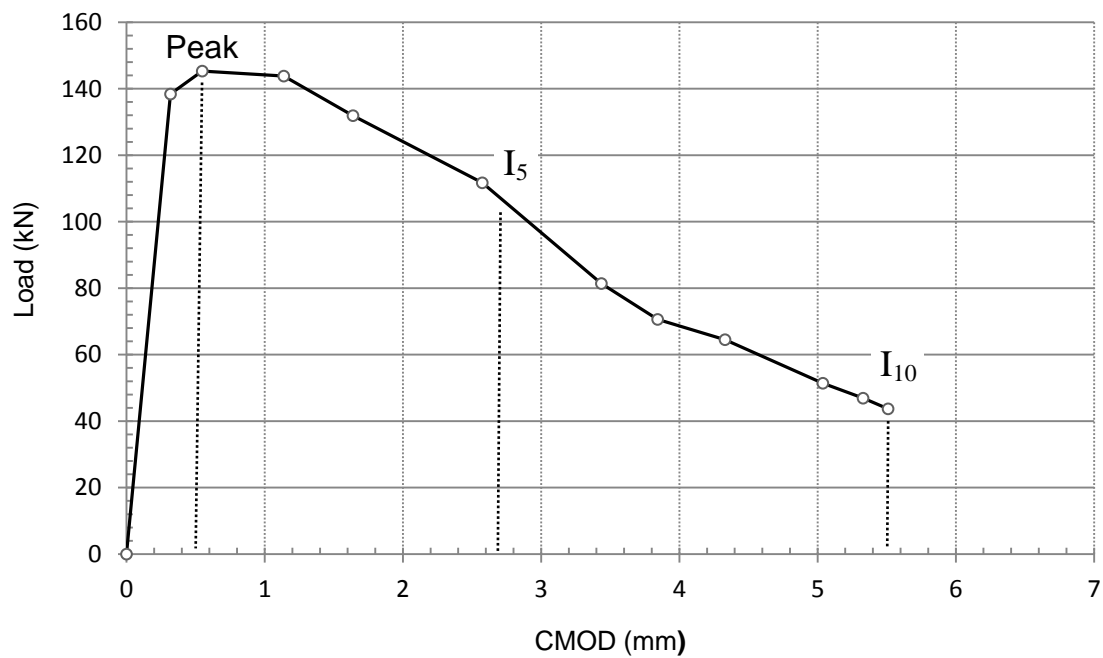


Figure 4.13 - Load-CMOD curve with toughness indices points (SFRC-6)

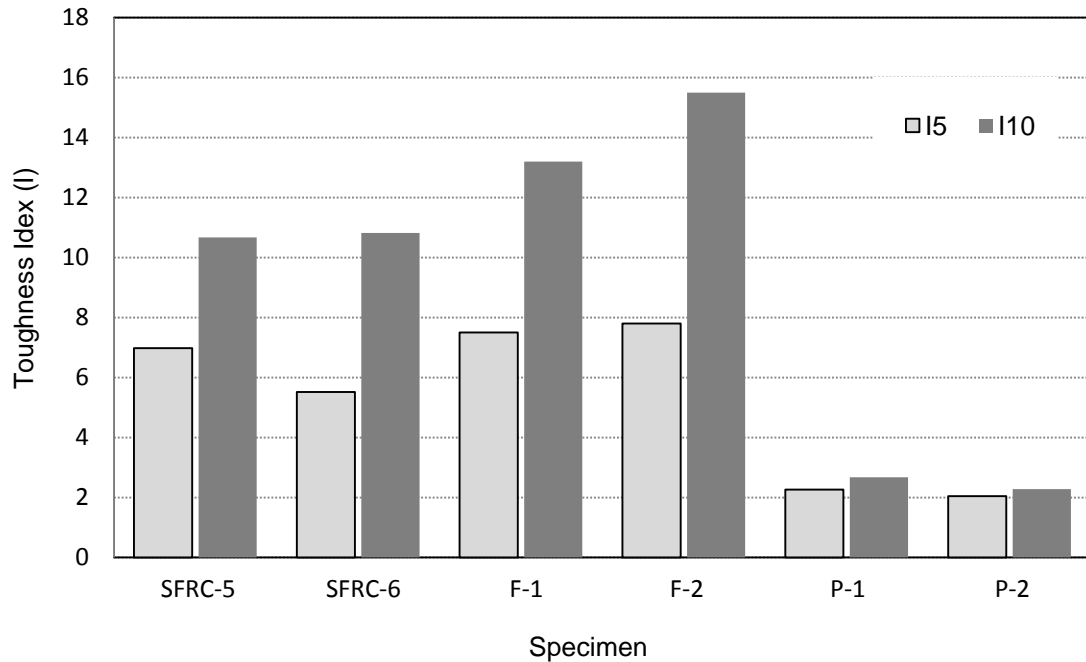


Figure 4.14 - Toughness indices of specimens (Deng *et al.*, 2006)

The load-CMOD curves used in the derivation of the toughness indices, I_5 and I_{10} for tests SFRC-5 and SFRC-6 are presented in Figure 4.12 and Figure 4.13, respectively. The test segment SFRC-5 failed just before reaching the necessary CMOD to determine the toughness index I_{10} (6.5 mm), hence the load-CMOD curve was extrapolated marginally.

According to a study done by Deng *et al.*, (2006), who experimentally investigated the toughness indices of plain and fibre reinforced concrete, it was found that the fibre reinforced concrete toughness index I_5 was 3.8 - 4.2 times and I_{10} was 5.8 - 6.8 times that of plain concrete. A comparison of the toughness indices between the experimental segment tests SFRC-5, SFRC-6 and results obtained from Deng *et al.*, (2006) on plain (P-1 and P-2) and fibre reinforced concrete (F-1 and F-2) is summarized in Figure 4.14.

As can be seen from the results, the steel fiber reinforced concrete specimens from both studies are distinguished from plain concrete by their superior toughness and ability to absorb large amounts of energy. Furthermore, for the SFRC specimens F-1 and F-2, with a similar volume fraction of fibres as the designed experimental segments (2%) appear to have slightly higher toughness indices. Once cracking has initiated, the cracks cannot extend without stretching and debonding the fibers from the concrete matrix. As a result, a large additional crack energy is absorbed before complete separation of the specimen occurs. Fibres with better bond characteristics (i.e. deformed fibres, or fibres with greater aspect ratio) give higher toughness values than do smooth, straight fibres at the same volumetric concentrations. Variation of fibre distribution and orientation will result in variable fibre volume concentrations and may also lower the material toughness.

4.6 Concrete Core Computed Tomography Scanning

The tensile behaviour of SFRC is greatly dependent on the fibre type, dosage, dispersion and orientation with respect to stress fields. The first two items can be controlled quite easily, however certain difficulties may arise when attempting to homogeneously distribute the fibres within the concrete matrix. Failure generally occurs at locations where stresses are either the highest, reinforcement is not sufficient, or a combination of both. When care is not taken during the casting phase, design specifications may not be met and structural failure can occur at much lower loads than anticipated. Given the observed variation of flexural response, it was of interest to examine the internal structure of select precast tunnel lining segments.

Figure 4.15 illustrates a comparison of fibre distribution and orientation between SFRC-1 and SFRC-2, along with the corresponding volume fraction of fibres per section. SFRC-2 shows a higher peak load, and larger tensile softening, than SFRC-1. It is interesting to note that in both segments there is a general increase in fibre volume fraction with distance from the extrados. Since the segments were constructed extrados up, there appears to be a gravity effect in their distribution and orientation as was also observed by De Waal (1999). It is also interesting that in core SFRC-2, there is a lack of any fibres in the top portion of the specimen (0%) suggesting excessive vibration techniques used during the casting phase. The use of self-consolidating concrete may be helpful in guaranteeing a more uniform dispersion of fibres, thanks to both its rheological stability and self-placability, which leads to the elimination of compaction by vibration (Ferrara *et al.*, 2008). Additionally, the orientation of fibres in core SFRC-2 appears to be angled downward at approximately 30° from the horizontal. This general orientation seems to be

in the tensile hoop stress direction of the segments and may improve the tensile resistance by activating the full pullout strength capacity of the fibres, perpendicular to the crack propagation direction.

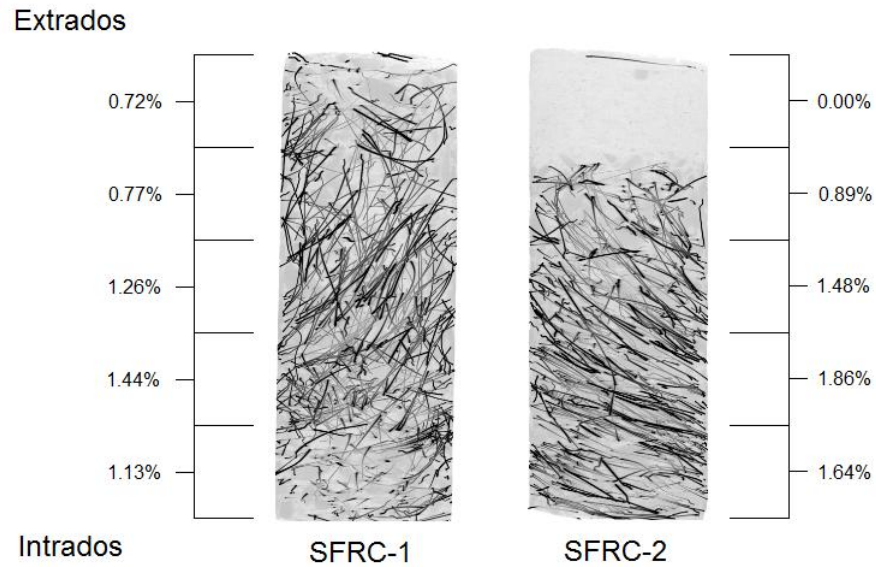


Figure 4.15 - Computed tomography fibre density (%) and orientation (SFRC-1 & -2)

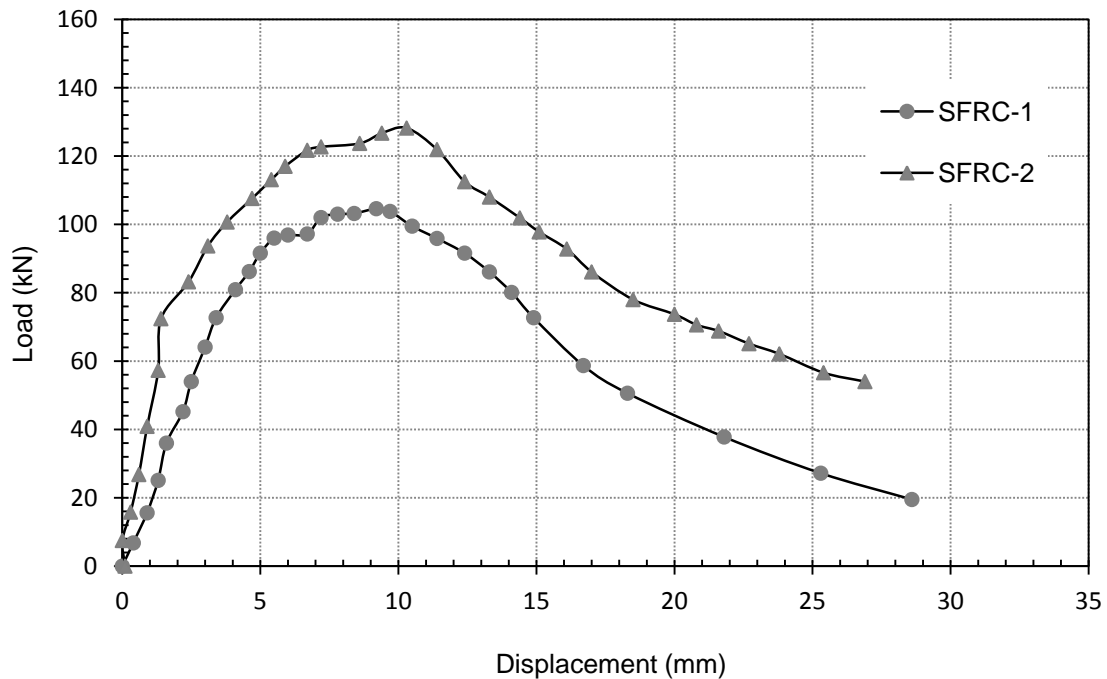


Figure 4.16 - Load-midspan displacement (SFRC-1 & -2)

4.7 Summary

In this chapter, the flexural behaviour of steel fibre reinforced concrete segments using a uniaxial line loading was evaluated. An initial pilot test, SFRC-P, was performed to optimize the testing methodology and logistics. From this trial test it was expected to verify the loading rate, strain and displacement response and failure point from the test segment. Using the optimized criteria developed from the pilot test, six additional flexure tests were performed and the load-displacement, load-strain and crack propagation behaviour was recorded. The crack propagation was monitored and recorded for flexure tests SFRC-5 and SFRC-6. Using Image J software analysis, the crack mouth opening displacement (CMOD) was determined and plotted against the corresponding load being applied. From this, toughness indices were obtained, which were used to characterize and compare the toughness and post-peak strain softening of the SFRC segments and other SFRC and plain concrete specimens. Finally, computed tomography scanning was used to examine the internal steel fibre content and orientation of select precast tunnel lining segments.

From the pilot test, SFRC-P, it was found that the rate dependency associated with a load-controlled loading caused the segment to fail in a brittle manner, preventing post-peak strain softening. Thus, displacement-controlled loading was used for tests SFRC-1 to SFRC-6 to capture the post-peak softening behaviour of the flexure tests. From the load-displacement and load-strain data collected during the testing program, it was concluded that the testing methodology developed (Chapter 3) for determining the flexural behaviour of steel fibre reinforced concrete tunnel segments was sufficiently well designed. Each segment was tested in a similar manner, yet variation in the peak loading

of 40% was present, suggesting possible non-uniformity in the material composition. Computed tomographic scan imaging of select precast tunnel lining segments revealed a variation of fibre distribution and orientation, verifying the effects of a possible gravity phenomenon present during the casting phase. Furthermore, an analysis of the toughness indices of test SFRC-5 and SFRC-6 revealed similar toughness characterisation between SFRC specimens from other studies and outlined its superior toughness performance in comparison to plain concrete.

FINITE ELEMENT MODELING

5.1 Introduction

This chapter explores the finite element analysis performed to simulate the flexural behaviour of steel fibre reinforced concrete tunnel lining segments. The experimental load-displacement and load-strain behaviour of the representative test SFRC-4 was compared to numerical results in an attempt to provide further insight into the behaviour and calibration of the constitutive model. ABAQUS, one of most powerful commercial finite element software tools available was chosen to perform the nonlinear analysis utilizing the concrete damage plasticity model (CDP) to simulate the inelastic mechanical behaviour. The compressive and tensile stress-strain material models deduced in Chapter 3 were used in the analysis.

Additionally, a modified model was generated to further analyse the non-homogenous fibre distribution, particularly the lack of fibres in the extrados region. The top $\frac{1}{3}$ extrados section was modelled as plain concrete (0% fibres), following the analysis performed on the core samples in Section 4.6 using computed tomography scanning techniques. Furthermore, a sensitivity analysis was conducted by varying the pertinent strength, elastic and tensile stress-strain parameters, and element mesh size to study the impact on the results.

5.2 Tunnel Lining Segment Response Predictions

The tunnel lining segments were modelled in ABAQUS with the material properties deduced from the uniaxial compressive cylinder and flexural beam tests in Chapter 3. Due to the mesh dependency phenomenon associated with non-linear finite element analysis, a brick element mesh size of 30 mm was used, identical to that of the flexure beam model from which the material properties were established. Furthermore, to minimize computation time, a coarser mesh was applied outside the cracking zone where mesh dependency is not as significant. The tunnel lining segment model consisted of 12,528 C3D8 linear brick elements. A mesh sensitivity analysis was performed and is shown in Appendix A to analyse the effects of mesh coarseness on the resultant peak loadings and displacements. The results demonstrate that as the number of elements increase and the mesh becomes finer, the model converges to a solution.

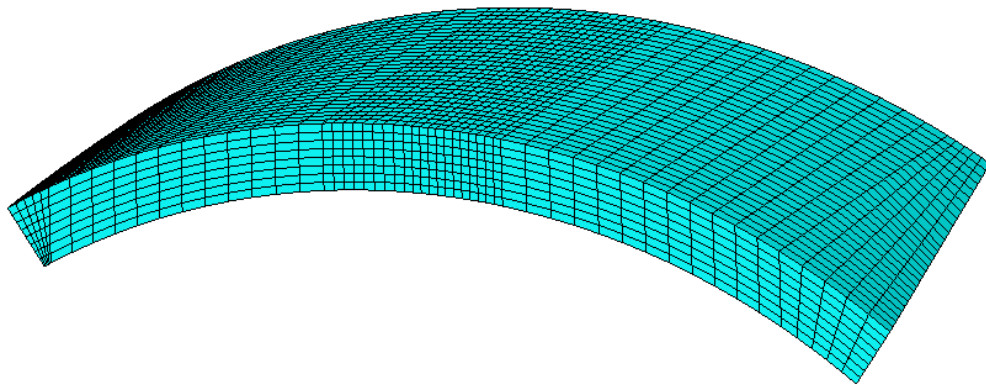


Figure 5.1 - Finite element lining segment model (12,528 elements)

FE results using ABAQUS were compared to the experimental results of a representative test SFRC-4 as shown in Figure 5.2 to Figure 5.4. Due to the geometric symmetry, the strains calculated at S-1, S-2, S-5, and S-6 along with strains at S-3 and S-4 showed

identical results. Thus, the displacements computed at D-1, and the strains calculated at S-2, and S-3, were compared with those measured from test SFRC-4. Additionally, the complete post-peak strain softening behaviour could not be predicted because the concrete damage plasticity finite element model calculations did not converge after a displacement of approximately 17 mm.

Figure 5.2 presents a comparison between the experimental and numerical load-deflection response at location D-1. The behaviour is similar in shape, but the finite element results in a 41% higher load carrying capacity in comparison to the representative experimental testing. This is thought to be due to differences in the expected and actual fibre distributions and orientation in the tunnel lining segments. The tensile parameters used in the FE model were deduced from the beam flexure tests, which were considered to have a higher quality control during casting. Furthermore, given no distinct curvature in the test beam geometry, the fibre gravity distribution phenomenon should not occur. Since the fibre distribution and orientation in the beams was potentially different to that of the segments, potentially higher material strength would be found.

The load vs. strain data is presented in Figure 5.3 and Figure 5.4. The FE results illustrate a much steeper slope, which indicates that the FE model is experiencing a stiffer response. The load vs. strain at the midpoint of the segment is linear elastic until a loading of approximately 120 kN, after which yielding occurs and segment failure follows. Lower strains are shown at an equivalent loading magnitude, revealing higher strength characteristics in the FE model. Due to the lack of uniform fibre distribution in the experimental tunnel lining segments, the steel fibre crack arresting performance in the numerical approximation is limited and thus larger strains result in the prediction.

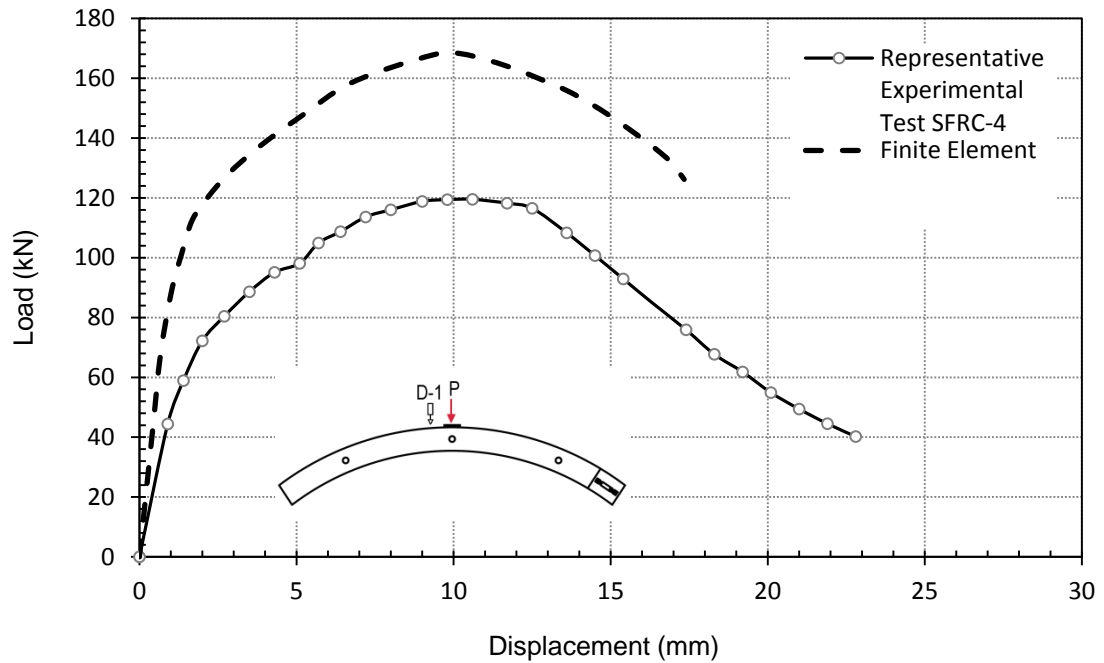


Figure 5.2 - A comparison between experimental and finite element results (at D-1)

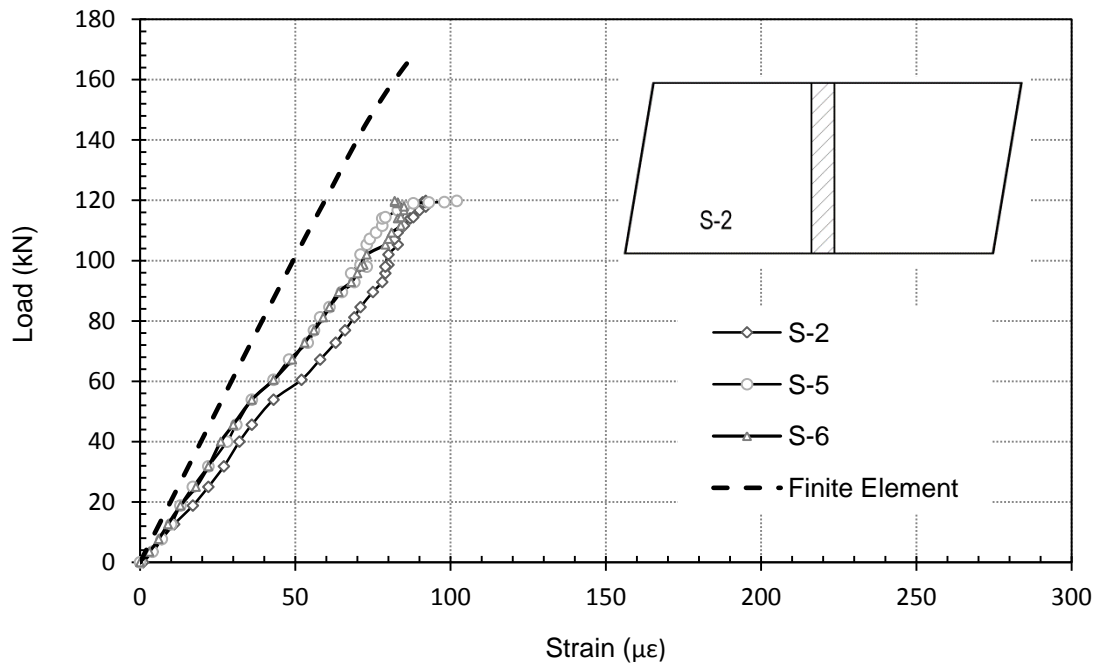


Figure 5.3 - A comparison between experimental and finite element results (at S-2)

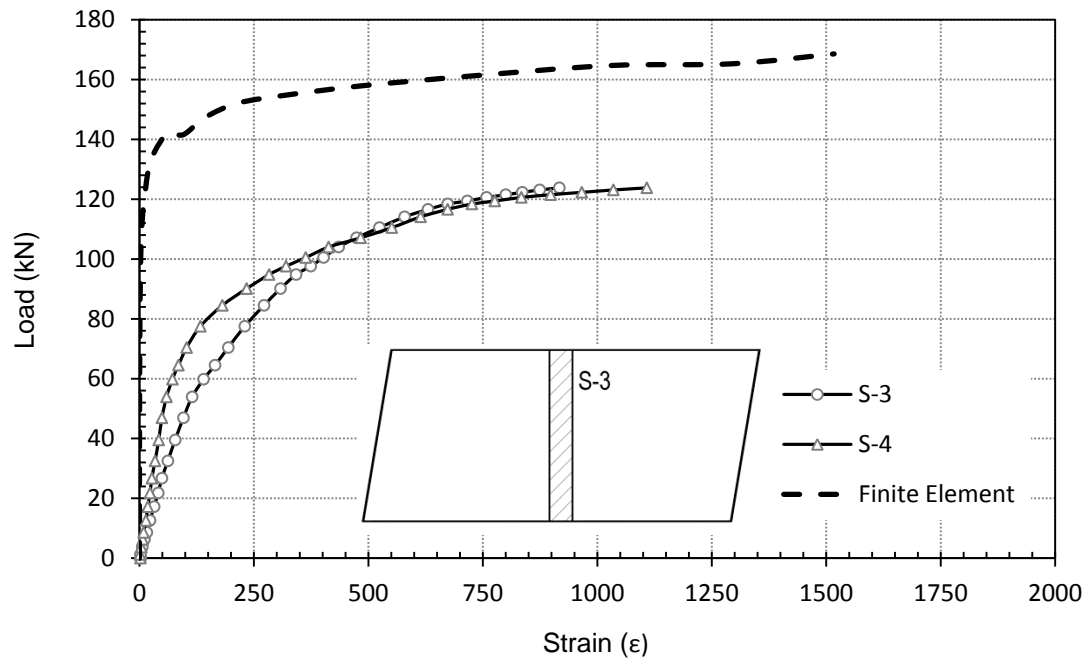


Figure 5.4 - A comparison between experimental and finite element results (at S-3)

5.3 Modified Analysis Study

Given the assumed variability in the distribution and orientation of the fibres in the segments, likely due to the influence of mixing or the compaction process, a modified study was performed to study these effects on the overall flexure capacity of segmented tunnel linings. A similar model was used in the numerical analysis as in the previous section, however the variation of fibre density with respect to depth was taken into account. With respect to the core samples taken, it was decided to model the top $\frac{1}{3}$ extrados thickness of the segment (78.3 mm) as plain concrete, representing a measure of 0% fibres as shown in Figure 5.5.

From the tensile stress-strain parameters deduced in Section 3.7.3, the SFRC had a maximum tensile strength of 8.42 MPa, after which a crack developed and the fibres began to hold the matrix together resulting in a strain softening behaviour. In plain concrete however, once the material cracks, it cannot carry any additional load and so failure occurs at the ultimate tensile strength of 8.42 MPa. Table 5.1 outlines the tensile stress-strain parameters used in modeling the plain concrete section.

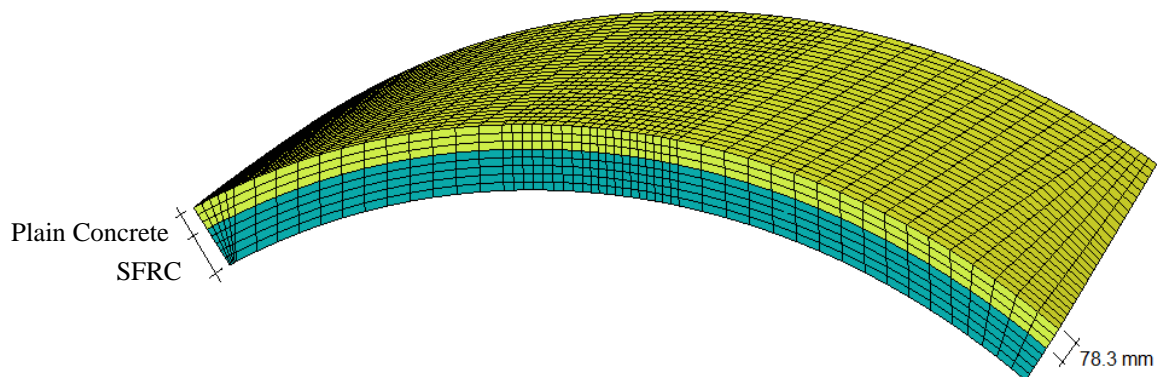


Figure 5.5 - Finite element lining model with top section modelled as plain concrete

Stress (MPa)	Strain (ϵ)
0	0
8.42	0.000144
0	0.000144

Table 5.1 - Tensile stress-strain parameters for plain concrete

Figure 5.6 presents a comparison between the experimental, numerical (original) and the numerical (modified) load-deflection response at location D-1. Similar to the original numerical modelling, the CDP finite element model calculations did not converge after a displacement of approximately 14 mm, failing to capture the entire post-peak strain softening behaviour.

The modified model follows a linear elastic behaviour up to a loading of approximately 70 kN, after which the material begins to yield, similar to the original numerical study. However, the load carrying capacity is 64% lower than that of the original numerical response, withstanding a peak load of 108 kN. After reaching a displacement of approximately 12.5 mm, the model experiences a sudden drop of load. It is thought that as cracking ensues, the neutral axis shifts up into the plain concrete zone, which can carry minimal tensile stress. The lack of reinforcement in the top section of the segment reduced the segment's load carrying capacity and diminished the post-peak performance.

In addition, the modified model shows very good agreement in comparison to the representative experimental test SFRC-4. The initial elastic response is somewhat stiffer and the peak-load is within 10% of that of the experimental testing. Hence, a lower modulus of elasticity is present in the experimental testing. By modelling the top $\frac{1}{3}$

extrados thickness as plain concrete with no fibre reinforcement, an overly conservative approach was taken. Nonetheless, it proves to be a good exercise in demonstrating the effects of inhomogeneous distribution of fibre reinforcement on the flexural behaviour of steel fibre reinforced concrete tunnel lining segments.

The load vs. strain data is presented in Figure 5.7 and Figure 5.8. The strain response at location S-2 appears to be softer than the original numerical analysis, however it shows very good agreement in comparison to the experimental testing. Similar behaviour is exhibited at the midspan strain gauge S-3.

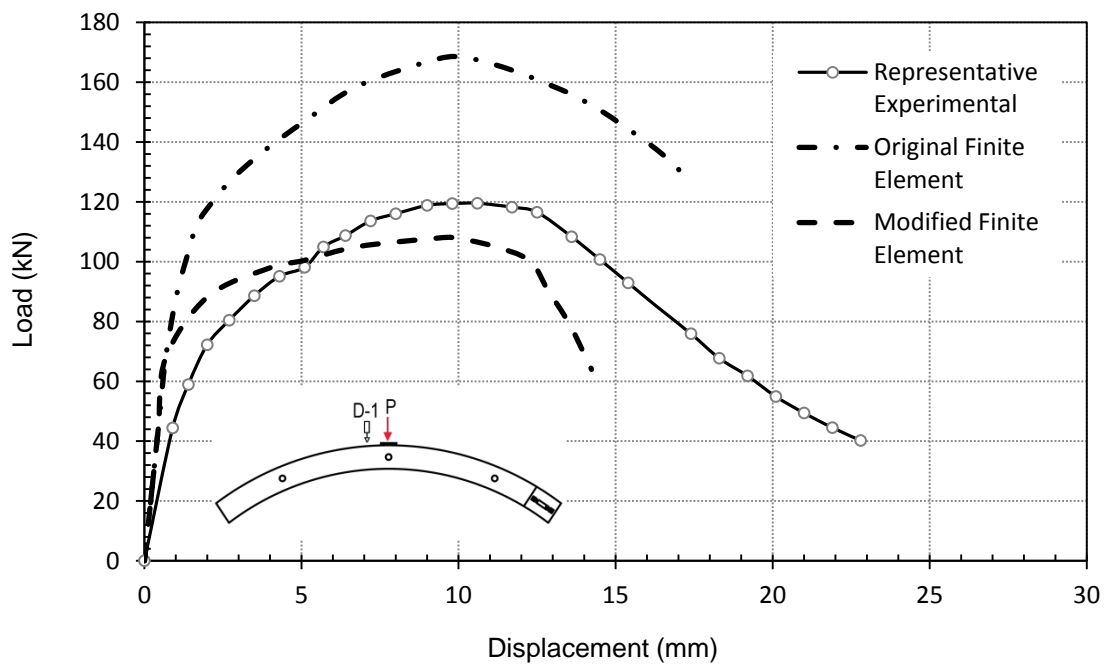


Figure 5.6 - A comparison between experimental, finite element and modified finite element results (at D-1)

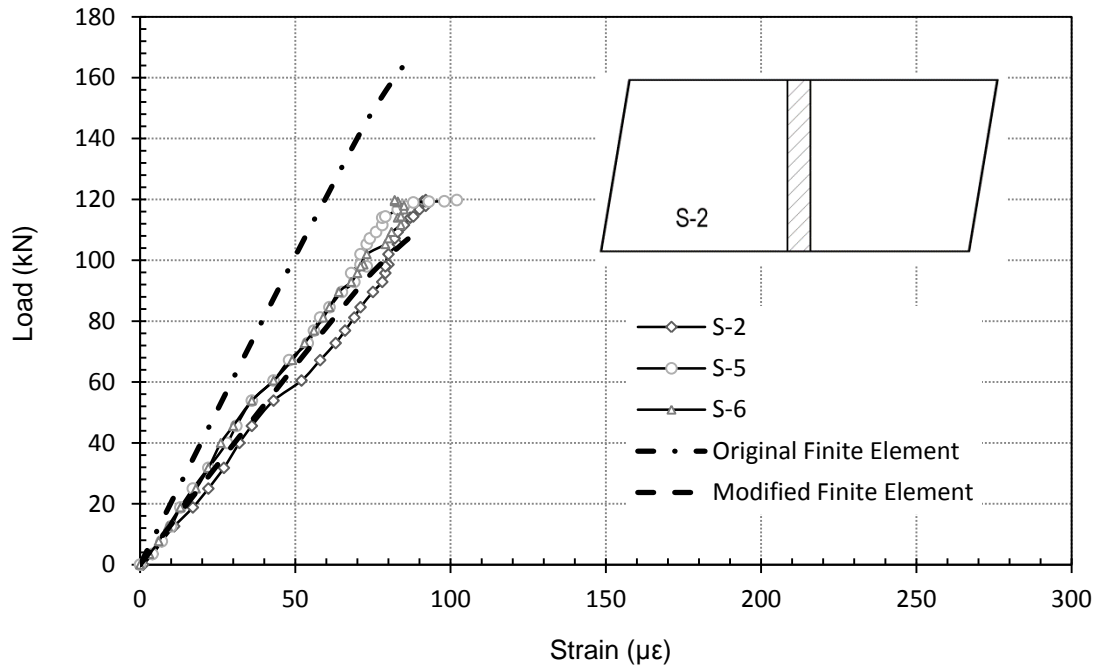


Figure 5.7 - A comparison between experimental, finite element and modified finite element results (at S-2)

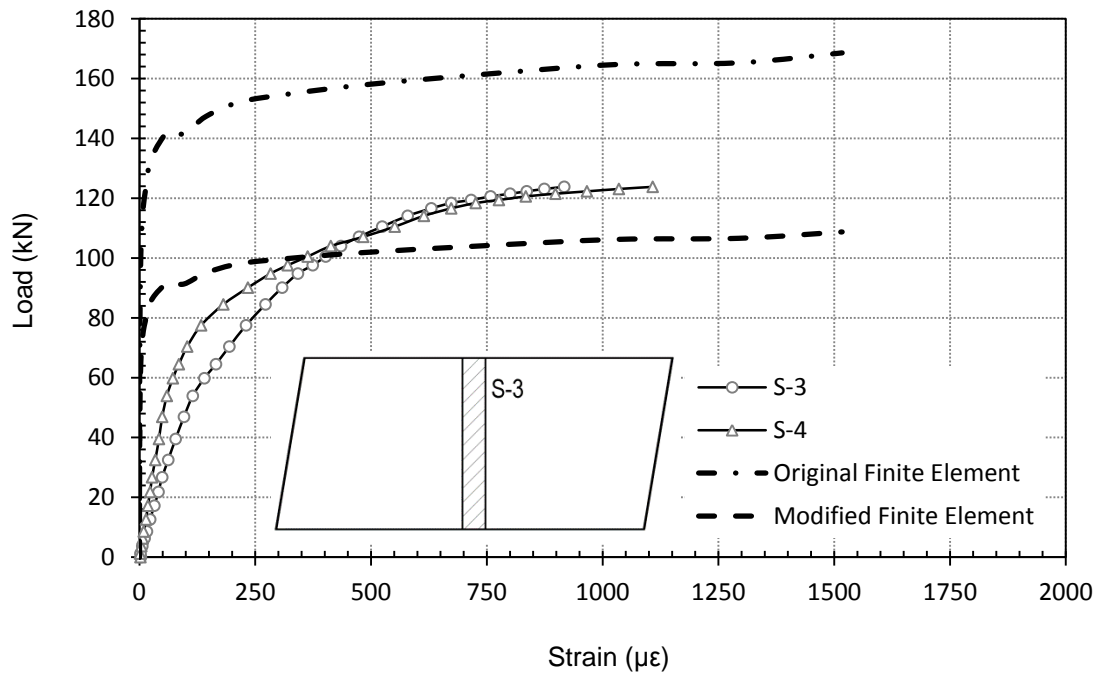


Figure 5.8 - A comparison between experimental, finite element and modified finite element results (at S-3)

5.4 Sensitivity Analysis

To ensure that a representative numerical model of the tunnel linings was developed, it is important to validate the model input parameters. Sensitivity analyses are often performed to quantify the effects that varying the material parameters of a numerical model have on the model outputs. Each of the material parameters included in the numerical model are listed in Table 5.2 below. These input parameters were varied as a means to gain insight into the model behaviour and to quantify their effects on the overall numerical response. Where possible the input parameters were varied in excess of the observed variations in the experimental tests, with typically a $\pm 30\%$ modification to the original values used for the modelling. The concrete damage plasticity model input parameters were not investigated in this study due to time constraints. From the numerical sensitivity analysis performed, it was established that the elastic modulus and the stress-strain tension stiffening parameters had the most significant impact on the model outputs. The other results of this exercise are shown in Appendix B.

Material Properties	Significant Impact?
Compressive Stress-Strain ³	✗
Tensile Stress-Strain ⁴	✓
Young's Modulus (E)	✓
Poisson's Ratio (ν)	✗
Density (ρ)	✗

Table 5.2 - Material parameter impact on the model output

³ Defined by 33 pairs of points from Figure 3.18

⁴ Defined by 4 pairs of points from Figure 3.26

5.4.1 Modified Modulus of Elasticity Parameter

From the comparison of experimental and numerical results in previous sections, it was found that the numerical behaviour showed a much stiffer initial response in comparison to the representative experimental test SFRC-4. Thus, it was of interest to study the variability in modelling output with a $\pm 50\%$ change in the modulus of elasticity. The modified parameters are summarized in Table 5.3 below.

Modification	Modulus of Elasticity (E_c)
- 50 %	18.6 GPa
Original	37.2 GPa
+ 50%	55.8 GPa

Table 5.3 - Modified modulus of elasticity input parameters

From Figure 5.9, it is shown that an increase in the modulus of elasticity by 50%, results in a stiffer initial elastic response of the segment. At a loading of 60 kN, the original finite element response results in a midspan displacement of approximately 0.6 mm. By decreasing or increasing the modulus of elasticity by 50%, the resultant midspan displacements are approximately 1.2 mm and 0.3 mm (or +50% and -50%), respectively. This stiffness continues up to a peak loading of approximately 171, kN after which the material experiences a post-peak strain softening behaviour similar to that of the original numeral response. By decreasing the modulus of elasticity by half, the load-displacement response follows a similar pattern, but with a softer response. The change in stiffness due to the modified modulus of elasticity input parameter can be validated by examining the output responses in the elastic region. The exercise demonstrates that in the elastic zone, the output behaviour is directly proportional to the modulus of elasticity

parameter. Furthermore, the variability of the uniaxial compressive cylinder strength in Section 3.6.2 results in a corresponding range of moduli of elasticity from 37.6 GPa and 41.9 GPa (11.4%) determined from Eq. 3.4. Based on the changes shown in the sensitivity analysis, it can be concluded that the observed experimental range of modulus of elasticity (given the compressive strength variability) has relatively small effects on the predicted outputs.

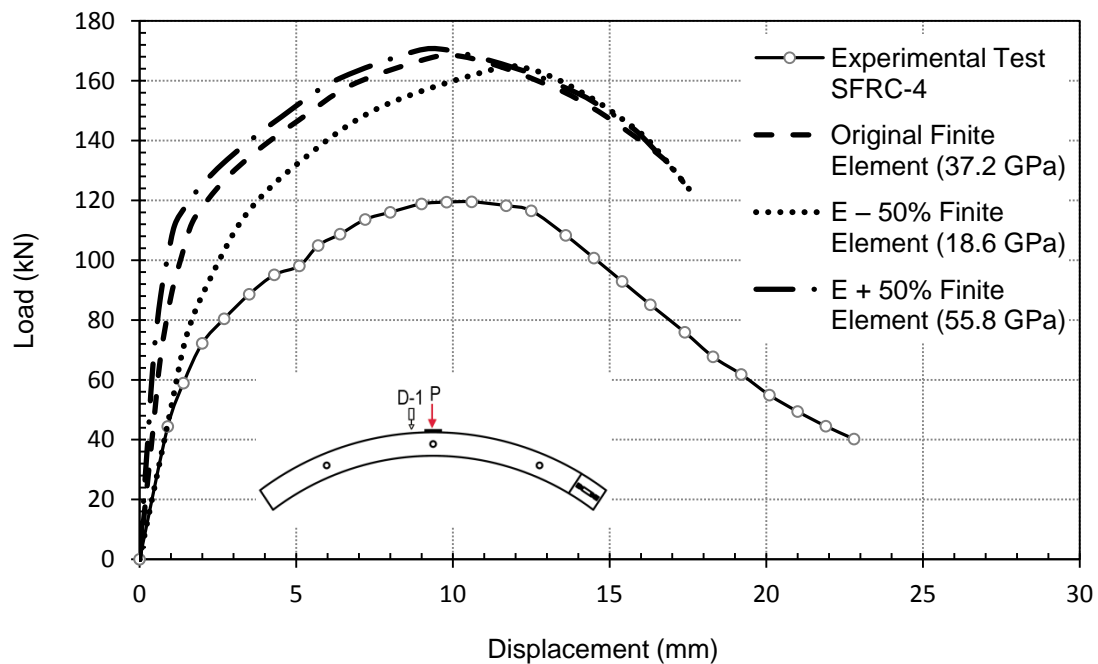


Figure 5.9 - Comparison between original and modified finite element analysis with input modulus of elasticity ($\pm 50\%$) at D-1

5.4.2 Modified Tensile Stress-Strain Parameters

The tensile stress-strain properties used in the numerical analysis of the tunnel segments were estimated from flexural beam test data. Due to the possible variability of material properties between the test beams and the full-scale tunnel segments, and potential errors in the approximation of the constitutive model, it is interesting to study the effects of modifying the tensile stress-strain input parameters to see the effects on the output responses of the numerical model. The stress component of the deduced tensile stress-strain parameters was modified by $\pm 30\%$ and the results are summarized in Figure 5.10 and Table 5.4.

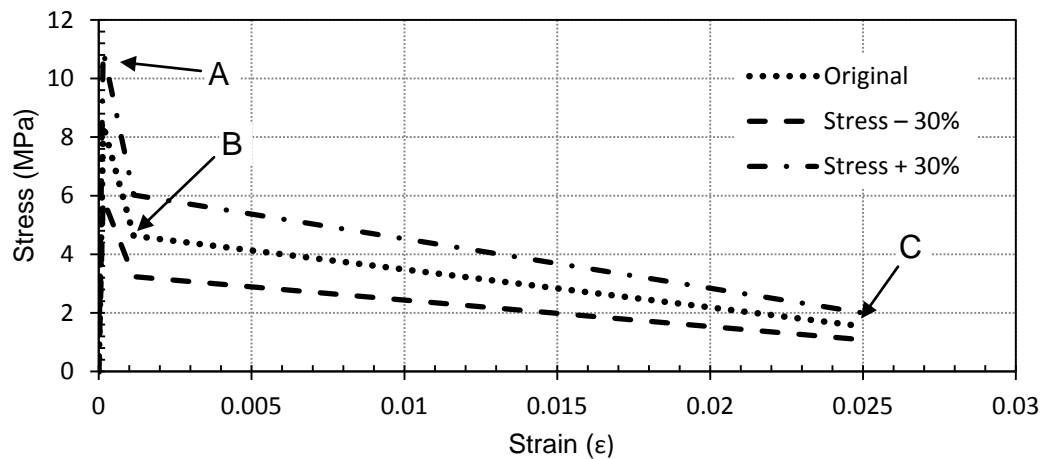


Figure 5.10 - Modified approximation of SFRC tensile stress input parameters

Parameter		- 30 %	Original	+ 30%
A	σ_1 (MPa)	5.89	8.42	10.95
B	σ_2 (MPa)	3.24	4.63	6.02
C	σ_3 (MPa)	1.08	1.54	2.00
	ϵ_1	0.000	0.000	0.000
	ϵ_2	0.0001	0.0001	0.0001
	ϵ_3	0.025	0.025	0.025

Table 5.4 - Modified tension stiffening stress numerical input parameters

The load-displacement behaviour from the modified tensile stress numerical results is plotted in Figure 5.11. The elastic region of the overall load-displacement curves remains unaffected by modifications done to the tension stiffening parameters, until crack formation initiates at a maximum tensile strength, f_t . Altering the stress component in the tensile stress-strain behaviour by $\pm 30\%$ directly correlates to the load where the non-linear plastic behaviour begins. Furthermore, the peak load is also increased or decreased from the initial numerical analysis by approximately $\pm 30\%$, respectively.

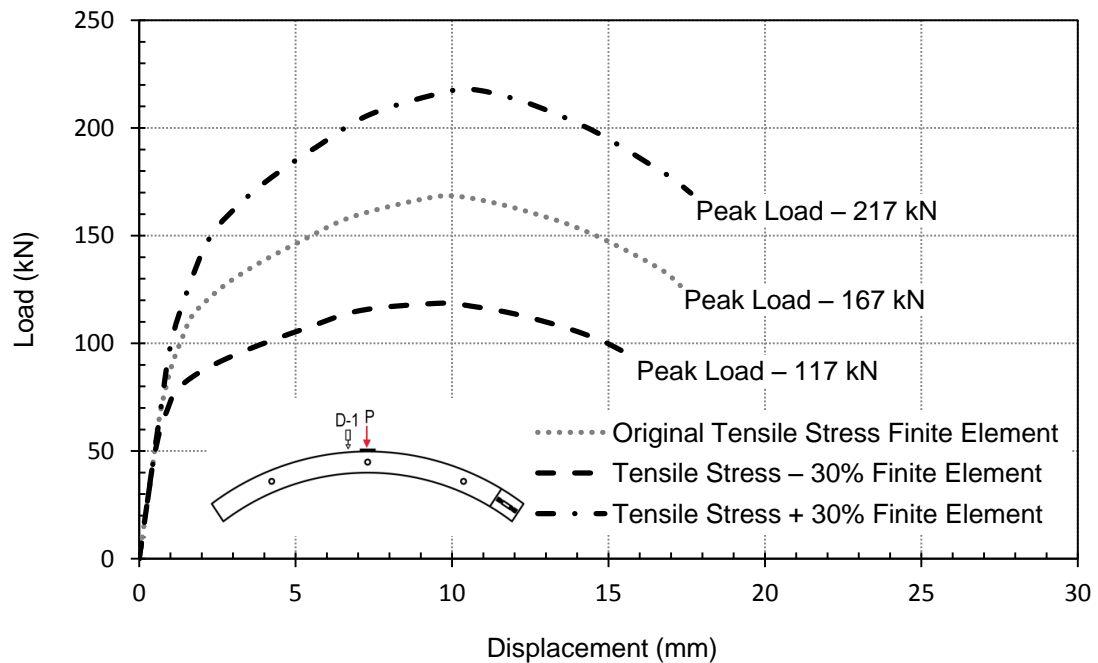


Figure 5.11 - Comparison between original and modified finite element results at D-1 with modified tensile softening stress ($\pm 30\%$)

Additionally, the strain component of the deduced tensile stress-strain parameters was modified by $\pm 30\%$ and is summarized in Figure 5.12 and Table 5.5.

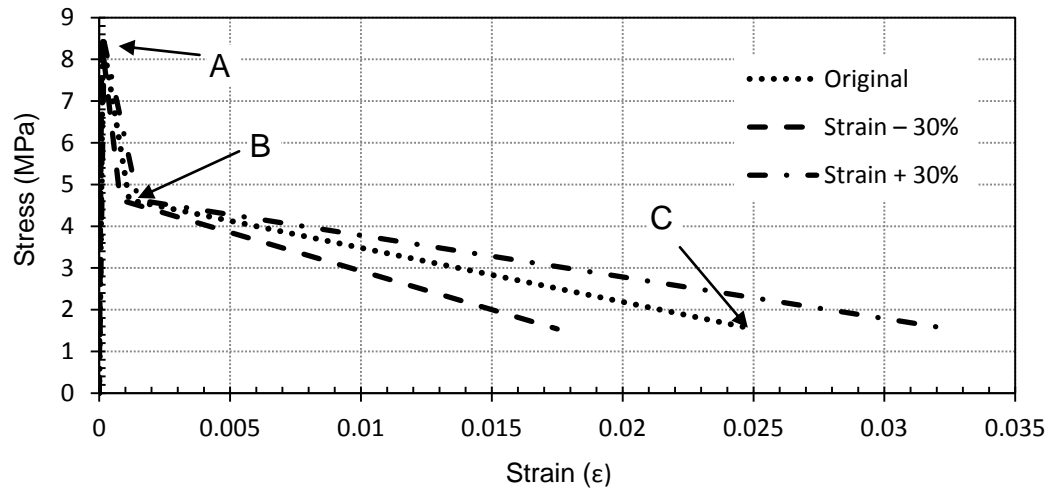


Figure 5.12 - Modified approximation of SFRC tensile strain input parameters

	Parameter	- 30 %	Original	+ 30%
A	ϵ_1	0.000	0.000	0.000
B	ϵ_2	0.0007	0.0001	0.0013
C	ϵ_3	0.0175	0.025	0.0325
	σ_1 (MPa)	8.42	8.42	8.42
	σ_2 (MPa)	4.63	4.63	4.63
	σ_3 (MPa)	1.54	1.54	1.54

Table 5.5 - Modified tension stiffening strain numerical input parameters

The load-displacement behaviour from the modified tensile strain numerical results is plotted in Figure 5.13. Similar to the modified tensile stress results, the initial elastic behaviour remains unaffected up to the maximum tensile strength, f_t . By altering the strain component in the tensile stress-strain behaviour by $\pm 30\%$ the yield and failure surface is correspondingly affected. Smaller strain inputs indicate that the material reaches its maximum tensile capacity at lower strains and thus begins to fail at lower deformations. This represents a diminished crack arresting capacity of steel fibres as cracks begin to propagate at lower stress values.

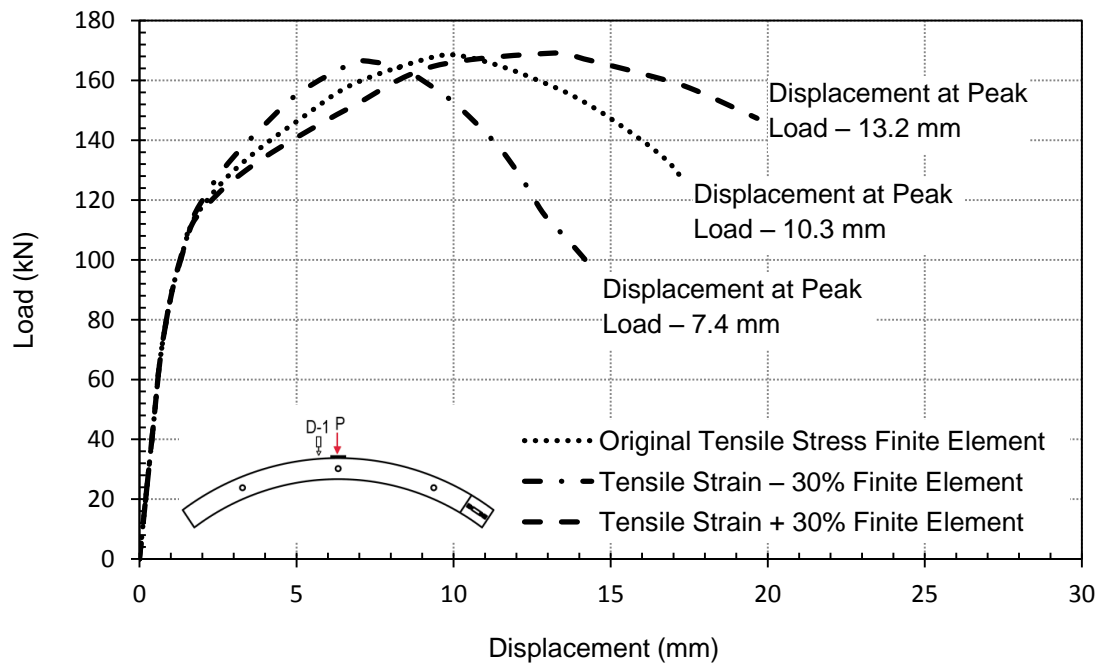


Figure 5.13 - Comparison between the original and finite element results at D-1 with modified tensile softening strain ($\pm 30\%$)

It is also of interest to study the effect of the slope of the tensile stress-strain relationship, since this controls the rate of the material's strain softening. The initial slope of the bi-linear approximation (AB) was modified by $\pm 30\%$ and this is summarized in Figure 5.14 and Table 5.6.

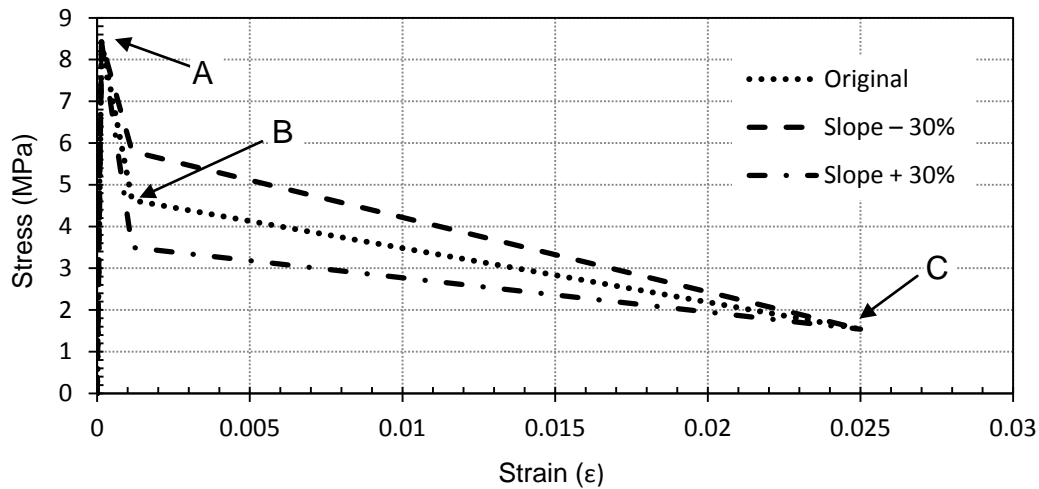


Figure 5.14 - Modified approximation of SFRC tensile stress-strain slope (AB) input parameters

	Parameter	- 30 %	Original	+ 30%
A	σ_1 (MPa)	8.42	8.42	8.42
B	σ_2 (MPa)	5.80	4.63	3.50
C	σ_3 (MPa)	1.54	1.54	1.54
	ϵ_1	0.000	0.000	0.000
	ϵ_2	0.0001	0.0001	0.0001
	ϵ_3	0.025	0.025	0.025

Table 5.6 - Modified tension stiffening slope (AB) numerical input parameters

The numerical predictions of the load-displacement behaviour from the modified tensile stress-strain slopes are plotted in Figure 5.15. By altering the slope (AB) of the tensile stress-strain relationship, the tensile yield surface of the material is consequently changed. This alters to material's ability to resist peak stresses with continued strain and

provides a different post-peak strain softening behaviour. With more material softening, the post-peak brittleness increases and the material more quickly fails to resist the stress acting on the specimen after the peak loading and loses strength with greater displacement.

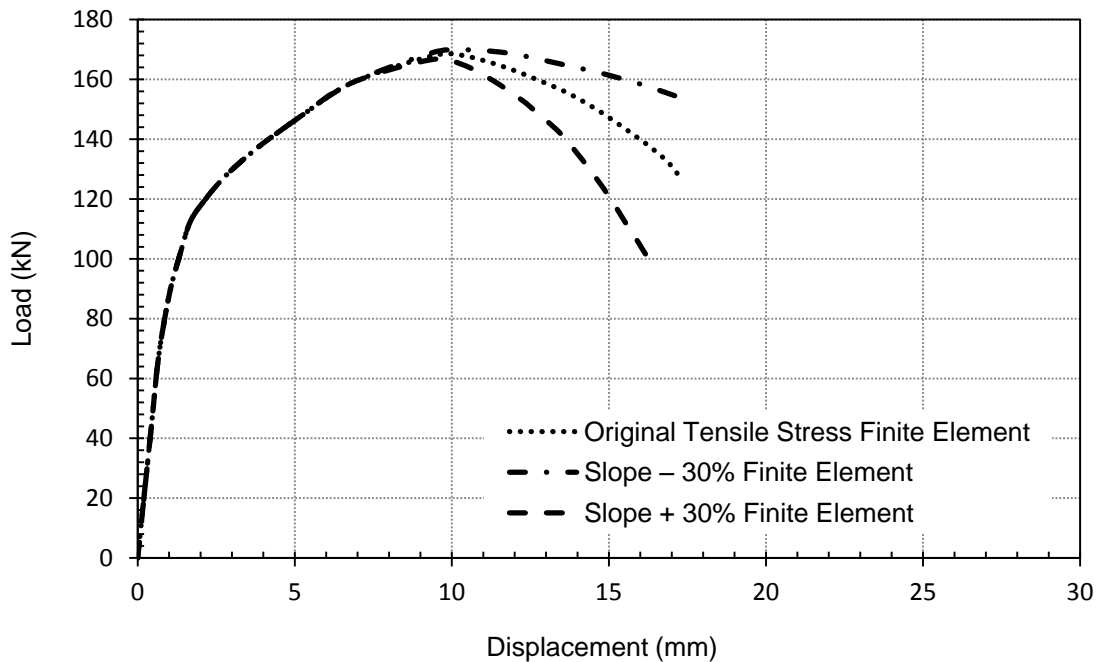


Figure 5.15 - Comparison between the original and modified finite element results at D-1 with modified tensile stress strain slope (AB) ($\pm 30\%$)

From the sensitivity analysis, it is shown that alterations of the tensile stress-strain input parameters can have a pronounced effect on the predicted structural behaviour of the steel fibre reinforced concrete tunnel linings. It is therefore suggested that the concrete material mixture and casting conditions be as close as possible in the flexure beam tests (from which the tensile parameters are deduced), as in the full-scale specimens that are being numerically modelled and that extreme care is taken during the derivation of the tensile stress-strain relationship.

5.5 Location of the Neutral Axis

The neutral axis is defined as the axis where the transition of tensile to compressive stress or strain is located due to bending (Caratelli *et al.*, 2011). From the SFRC stress block diagrams presented in Section 2.2.2, the neutral axis can be visually determined by the location of the crack tip as it propagates with increased loading. Using the Image J software analysis, the crack tip location was determined from various midspan displacements throughout the duration of test SFRC-5. The modified numerical study (varying fibre density with depth of the segment) was also used to determine the location of the neutral axis. By examining the change from tensile to compressive strain (in plane) at specific points during the analysis, the location of the neutral axis was determined. A comparison between the experimental and modified finite element neutral axis movement at the midspan of the tunnel lining segment is presented in Figure 5.17 and in Appendix C.

Although the numerical and experimental results presented have some potential errors the results shown give quite good agreement. Initially, the neutral axis is approximately located at the centroid of the tunnel segment prior to being subjected to any additional stresses. As the tunnel segment is loaded, cracking initiates in the tensile region and the crack begins to propagate towards the extrados of the segment. Once the crack tip reaches the initial location of the neutral axis, the neutral axis begins to shift upward into the compression zone and closer to the extrados of the segment. The quality of this comparison suggests that the numerical modelling is producing strain-softening and tensile behaviour in the correct zones during loading and provides further confirmation of the approach.

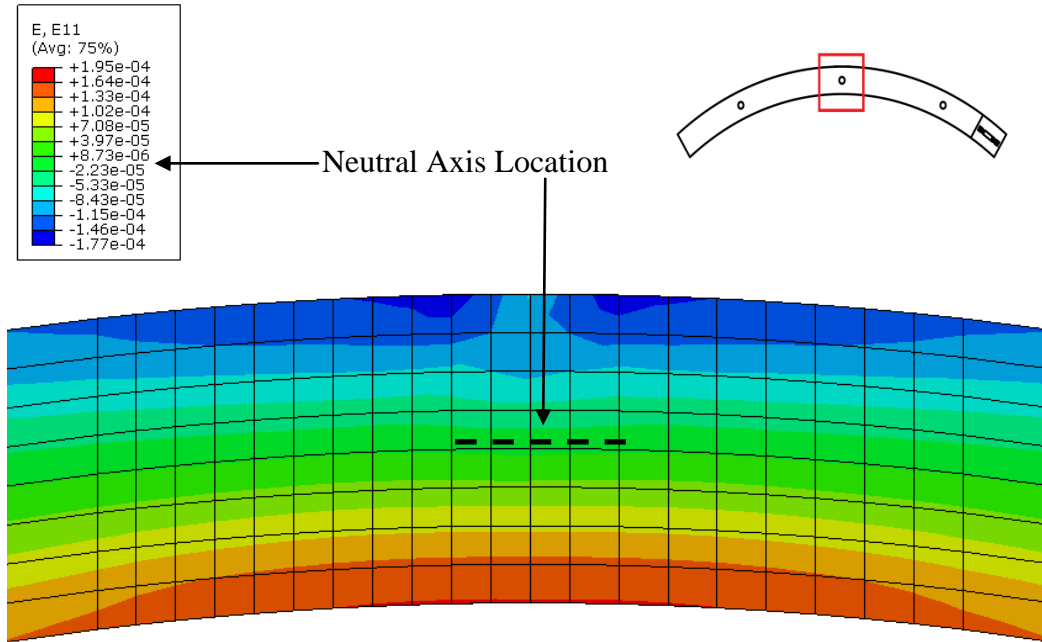


Figure 5.16 - Finite element tensile and compressive strain plot

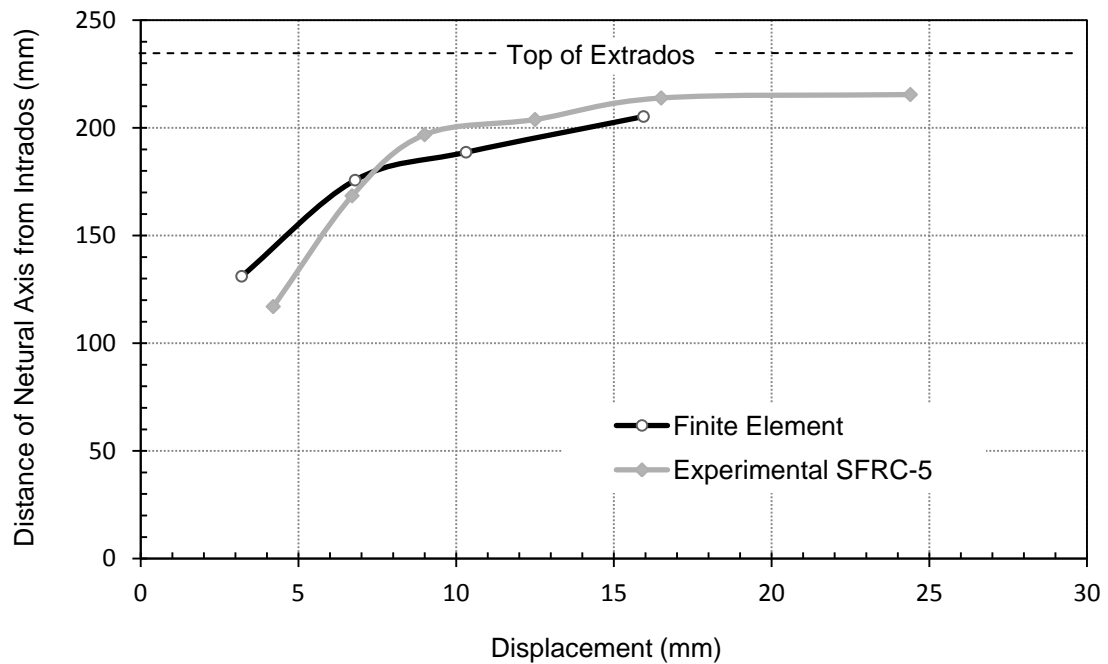


Figure 5.17 - Comparison between the experimental and modified finite element neutral axis movement at the midspan of the tunnel lining segment

5.6 Summary

A non-linear elasto-plastic finite element analysis was conducted to compare the load-displacement and load-strain behaviour of SFRC tunnel segments with the measured experimental data from a full-scale representative test SFRC-4. The concrete damage plasticity model available in software ABAQUS was used in the analysis utilizing the compressive and tensile stress-strain models deduced in Chapter 3 as input parameters. Additionally, a modified model was generated to analyse the effects of non-homogenous fibre distribution, particularly the lack of fibres in the extrados region. The top $\frac{1}{3}$ extrados section was modelled as plain concrete (0% fibres), following the analysis performed on the core samples in Section 4.6 using computed tomography scanning techniques. Furthermore, in an attempt to quantify the effects that variability of the parameters in the CDP numerical model have on the model output, a sensitivity analysis was conducted by varying the modulus of elasticity by $\pm 50\%$ and the tensile stress-strain parameters by $\pm 30\%$.

It was observed that the original numerical model predicted a higher strength capacity with respect to the experimental results, suggesting that the beam tests from which the uniaxial tensile stress-strain parameters were deduced had higher strength and stiffness characteristics. By modelling the inhomogeneous fibre distribution in the extrados section of the segment, it was found that the modified numerical results underestimated the experimental response, however it demonstrated much better agreement in comparison to the original numerical analysis. Thus for the finite element numerical tool to accurately predict “real life” structural behaviour, there is a need for realistic material composition to be replicated in the model.

Furthermore, varying the modulus of elasticity (E_c) by $\pm 50\%$, had little effect on the overall flexural behaviour of steel fibre reinforced concrete tunnel linings. Examining the range of E_c of the segments (11.4%) deduced from experimental cylinder compression tests, it was concluded that the variability of E_c had a negligible effect on the numerical output, based on the minor changes experienced from the sensitivity analysis. In comparison, the numerical model is highly sensitive to changes in the tensile stress-strain input parameters, and so great care must be taken when deducing these material properties from representative flexural beam tests.

SUMMARY AND CONCLUSIONS

6.1 Summary

The usage and range of applications of steel fibre reinforced concrete (SFRC) have recently increased in civil infrastructure due to a greater appreciation of the enhanced tensile behaviour, increased toughness and better crack arrestment properties. In Chapter 2, the state-of-the-art literature for SFRC technology used in segmented tunnel linings was discussed. Tunnel lining tests and design methods were also evaluated to identify areas of interest.

In Chapter 3, a method was developed to study the load-displacement, load-strain, and crack propagation behaviour of SFRC tunnel lining segments subjected to uniaxial flexure loading conditions using three-point bending tests. Standardized compressive cylinder and flexure beam tests were performed to deduce the SFRC material properties and to aid replication of the segmented flexure tests using numerical methods.

Chapter 4 presents the experimental results from flexure tests performed on the tunnel lining segments. Image analysis software was used to determine the crack initiation and propagation and computed tomography scanning was used to establish the internal fibre structure of the concrete mix, resulting from the casting process.

Chapter 5 describes the non-linear elasto-plastic finite element model used to estimate the structural response of the experimental flexure testing of the tunnel lining. A modified study was performed to study the effect of inadequate fibre distribution in the lining

segment on the overall flexural behaviour. Furthermore, a sensitivity analysis was conducted by varying the modulus of elasticity and the tensile softening stress-strain parameters to quantify the effects that variability of the parameters in the numerical model have on the model outputs.

From this study, the following conclusions were made:

- i. A uniaxial line load was found to be an appropriate method for evaluating the flexural response of full-scale segmented concrete tunnel linings.
- ii. Displacement-controlled loading is the optimal loading condition for capturing the post-peak ductility of SFRC segments in flexural loading.
- iii. For a lining with an internal diameter of 5400 mm, thickness of 235 mm, width of 150 mm, and a volumetric fraction of fibres = 2%, the mean value of the first crack load and peak load was 103.5 kN and 124.3 kN respectively, with standard deviations of 10.9 kN and 12.4 kN. The mean value of displacement at first crack load and displacement at peak load was 4.23 mm and 8.58 mm respectively, with standard deviations of 0.83 mm and 1.66 mm.
- iv. Unconfined compression tests were performed on eight SFRC core cylinders resulting in mean values of standard cured cylinder strength of 72.41 MPa with a standard deviation of 7.34 MPa. Split cylinder tests were performed on three core specimens resulting in a mean value of tensile strength of 7.69 MPa.

- v. Computed tomography scanning verified that the variation of fibre distribution in the SFRC segments ranged from 0% to 1.86 %, with the majority of fibres being located at the intrados of the segments.
- vi. A gravity distribution phenomenon appears to be present in the casting of tunnel lining segments due to its geometric curvature, concrete placement or vibratory methods.
- vii. The concrete damage plasticity model in the finite element software ABAQUS seems to be an appropriate model for the analysis of steel fibre reinforced concrete tunnel liners, enabling the capture of the majority of the post-peak performance.
- viii. The concrete damage plasticity finite element model is mesh dependent; an appropriate mesh size needs to be used in the segment modelling based on the derivation of tensile properties from a flexural beam model.
- ix. The numerical model of the segments initially predicted higher strength characteristics with respect to the experimental results, suggesting that the numerical model required some modification to account for the actual distribution of the reinforcing fibres through the segment depth.
- x. The numerical model of the tunnel linings (and SFRC models in general) are highly sensitive to changes in the tensile stress-strain input parameters and great care must be taken when deducing these material properties from representative flexural beam tests.

6.2 Recommendations for Future Work

The following is a list of recommendations for further research:

- i. Further analysis of the spatial distribution and orientation of fibres in tunnel lining segments by means of core CT scanning to properly characterize the pouring and compaction phenomenon effect on fibre dispersion.
- ii. Analyse the internal structure and fibre distribution of the flexure beam tests from which the uniaxial tensile stress-strain parameters are deduced and compare to the full-scale segment specimens.
- iii. Numerical modelling of the spatial distribution of steel fibre volume percentages should be performed to more accurately analyse the effects of fibre variation from the gravity distribution phenomenon.
- iv. Better measurement and characterization of the tensile properties of SFRC from the load-crack mouth opening displacement relationships and development of associated constitutive models.
- v. Improved mesh dependent fibre concrete stress-strain constitutive models and improved numerical discretization schemes that regulate mesh dependency effects for strain-softening problems.
- vi. Study the damage and micro-cracking of tunnel lining segments caused by long-term storage and transportation and in-situ loading.

REFERENCES

- ABAQUS *Analysis User's Manual* (2007).
- Abramoff, M.D., Magelhaes, P.J., Ram, S.J. 2004. Image Processing with ImageJ. *Biophotonics International*, 11(7): pp. 36-42.
- ACI Committee 544.1R-96. 1996. State-of-the-Art Report on Fiber Reinforced Concrete. *American Concrete Institute*, Farmington Hills, Michigan.
- ACI Committee 544.3R-93. 1998. Guide for Specifying, Proportioning, Mixing, Placing and Finishing Steel Fiber Reinforced Concrete. *American Concrete Institute*, Farmington Hills, Michigan.
- ACI Committee 544.XXE-08. 2008. Indirect Method for Obtaining a Model Stress-Strain Curve of Strain Softening FRC. *American Concrete Institute*, Farmington Hills, Michigan.
- Ahn, T. 2011. Thermal and Mechanical Studies of Thin Spray-On Liner (TSL) for Concrete Tunnel Linings. *Ph.D Thesis*, University of Western Ontario, Canada
- Aruga, T., Arai, Y., and Tsuno, K. 2007. Non-Linear Stiffness Behavior and Analysis of Tunnel Lining with Reinforcing Bars. *Quarterly Report, Railway Technical Research Institute*, 48(1): pp. 44-49.
- ASTM Standards A820/A820M-06. 2006. Standard Specification for Steel Fibres for Fibre-Reinforced Concrete. *ASTM International*, West Conshohocken, PA, DOI: 10.1520/A0820_A0820M-06.www.astm.org
- ASTM Standards C39/C39M-10. 2010. Standard Test Method for Compressive Strength of Cylindrical Concrete Specimens. *ASTM International*, West Conshohocken, PA, DOI:10.1520/C0039_C0039M-10. www.astm.org

- ASTM Standards C78/78M-10. 2010. Standard Test Method for Flexural Strength of Concrete (Using Simple Beam with Third Point Loading) *ASTM International*, West Conshohocken, PA, DOI:10.1520/C0078_C0078M-10. www.astm.org
- ASTM Standards C496/C496M-04. 2004. Standard Test Method for Splitting Tensile Strength of Cylindrical Concrete Specimens. *ASTM International*, West Conshohocken, PA, DOI:10.1520/C0496_C0496M-04. www.astm.org
- ASTM Standards C617-10. 2010. Standard Practice for Capping Cylindrical Concrete Specimens. *ASTM International*, West Conshohocken, PA, DOI:10.1520/C0617-10. www.astm.org
- ASTM Standards C1609/C1609M-10. 2010. Standard Test Method for Flexural Performance of Fiber-Reinforced Concrete. *ASTM International*, West Conshohocken, PA, DOI: 10.1520/C1609_C1609M-10. www.astm.org
- Banthia, Nemkumar. 2001. Fiber Reinforced Cements and Concretes. *Canadian Journal of Civil Engineering*, 28(5): pp. 879-880.
- Barros, J.A.O. & Figueiras, J. 1999. Flexural Behaviour of Steel Fibre Reinforced Concrete: Testing and Modelling. *Journal of Materials in Civil Engineering*, 11(4): pp. 331-39.
- Bencardino, F., Rizzuti, L., Spadea, G. & Swamy, R.N. 2007. Stress-Strain Behaviour of Steel Fibre Reinforced Concrete in Compression. *ASCE Journal of Materials in Civil Engineering*, 20(3): pp. 255-263.
- Brekke, T.L., Ripley, B.D. 1987. Design Guidelines for Pressure Tunnels and Shafts. *EPRI Research Project AP-5273*, University of California at Berkeley.
- Caliskan, S. 2007. Examining Concrete Cores by Non-destructive Techniques. *4th Middle East NDT Conference and Exhibition*, Kingdom of Bahrain, Dec 2007

- Caratelli, A., Meda, A., Rinaldi, Z., Romualdi, P. 2011. Structural Behaviour of Precast Tunnel Segments in Fiber Reinforced Concrete. *Tunneling and Underground Space Technology*, 26: pp. 284-291.
- Carreira, D.J., Chu, K.H. 1985. Stress Strain Relationship for Plain Concrete in Compression. *American Concrete Institute*, 83(6): pp. 797-804.
- Chanh, Nguyen Van. 1999. Steel Fibre Reinforced Concrete. *Faculty of Civil Engineering*, Ho Chi Minh City University of Technology, pp. 108-116.
- Chen, B., Liub, J. 2004. Residual Strength of Hybrid-Fibre-Reinforced High-Strength Concrete after Exposure to High Temperatures. *Cement and Concrete Research*, 34: pp. 1065-1069.
- Chen, Y., Qiao, P. 2011. Crack Growth Resistance of Hybrid Fiber-Reinforced Cement Matrix Composites. *Journal of Aerospace Engineering*, 24: pp. 154-161.
- Deng, Z.C., Deng, H.L., Li, J.H., Liu, G.D. 2006. Flexural Fatigue Behaviour and Performance Characteristics of Polyacrylonitrile Fiber Reinforced Concrete. *Key Engineering Materials*, 302-303: pp 572-583.
- El Naggar, H., Hinchberger, S.D. 2008. An Analytical Solution for Jointed Tunnel Linings in Elastic Soil or Rock. *Canadian Geotechnical Journal*, 45: pp. 1572-1593.
- Edgington, J. and Hannant, D.J. 1972. Steel Fibre Reinforced Concrete: The Effect on Fibre Orientation of Compaction by Vibration. *Materials and Structures*, 5(25): pp. 41-44.
- Ezeldin, A. & Balagurur, P. 1992. Normal-High Strength Fibre Reinforced Concrete Under Compression. *Journal of Materials in Civil Engineering*, 4(4): pp. 415-29.

- Ferrara, L., Park, Y.D., Shag, S.P. 2008. Correlation Among Fresh State Behaviour, Fiber Dispersion, and Toughness Properties of SFRCs. *Journal for Material Civil Engineering*, 20: pp. 493-501.
- Gettu, R., Gardner, D.R., Saldivar, H., Barragan, B.E. 2004. Study of the Distribution and Orientation of Fibres in SFRC Specimens. *Materials and Structures*, 38(1): pp. 31-37.
- Ghaffar, A.M., Leahy, R.M., Masri, S.F., Synolakis, C.E. 1992. A Feasibility Study for a Concrete Core Tomographer. *Nondestructive Testing of Concrete Elements Elements and Structures*, ASCE, pp. 37-38.
- Ghoraishi, M.S., Zadhoush, A., Ghareh , A. 2011. Effect of Shape and Orientation of Carbon Steel Fiber on the Modulus of Epoxy-Based Composite. *Journal of Applied Polymer Science*, 121: pp. 469–474 .
- Hansel, D., Guirguis, P. 2011. Steel Fibre Reinforced Segmented Linings: State of the Art and Completed Projects. *Tunnel 1/2001*.
- Jankowiak T., Lodygowski T. 2005. Identification of Parameters of Concrete Damage Plasticity Constitutive Model. *Foundations of Civil and Environmental Engineering*, 6(5): pp. 960-975.
- Jones P.A., Austin S.A., Robins P.J. 2008. Predicting the Flexural Load–Deflection Response of Steel Fibre Reinforced Concrete from Strain, Crack-Width, Fibre Pull-Out and Distribution Data. *Materials and Structures*, 41: pp. 449-463
- Mashimo, H., Isago, N., Yoshinaga, S., Shiroma, H., and Baba, K. 2002. Experimental Investigation on Load Carrying Capacity of Concrete Tunnel Lining. *28th ITA General Assembly and World Tunnel Congress*.
- MicroView v.2.1.2. 2000-2006. *GE Healthcare*.
- Moccichino, M., Romualdi, P., Perruzza, P., Meda, A. and Rinaldi, Z. 2006. Experimental Tests on Tunnel Precast Segmental Lining with Fibre Reinforced Concrete. *World Tunnel Congress ITA-AITES*, Seoul.

- Murray, Y.D., Odeh, A.A., and Bligh, R. 2007. Evaluation of LS-DYNA Concrete Material Model 159. *Texas Transportation Institute*, Report No. FHWA-HRT-05-063
- Nataraja, M., Dhang, N. & Gupta, A., 1999. Stress-Strain Curve for Steel Fibre Reinforced Concrete Under Compression. *Cement and Concrete Composites*, 21: pp. 383-90.
- Noel J., Datoussaid S., Dargain F. 2012. Potential Interest of the Barcelona Model for Predicting the Efficiency of a Tool Set Configuration in Geo-Material Cutting. *9th National Congress on Theoretical and Applied Mechanics*, May 9th 2012.
- Pevsner, P., Levy, R., Nsieri, E., and Rutenberg, A. 2005. Benchmark II: Numerical Analyses for Masonry Vault. *Israel Institute of Technology*, Haifa, Israel.
- Poh, J., Tan, K. H., Peterson, G. L., and Wen, D. 2009. Structural Testing of Steel Fibre Reinforced Concrete (SFRC) Tunnel Lining Segments in Singapore. *Land Transport Authority*, Singapore.
- Puso, M. A., Soldberg, J. 2006. A Stabilized Nodally Integrated Tetrahedral. *International Journal for Numerical Methods in Engineering*, 67(6):, pp. 841-867
- Rancourt, A.J. and Mitri, H.S. 2007. Hydraulic Testing for the Design of Unlined Pressure Tunnels. *Canadian Tunnelling Magazine*, pp. 32-37.
- RILEM TC 162-TDF. 2000. Test and Design Method for Steel Fibre Reinforced Concrete: Recommendations for Bending Test. *Materials and Structures*, 35(225): pp. 3-5.
- Shayanfar M. A., Kheyroddii A., Mirza M.S. 1997. Element Size Effects in Nonlinear Analysis of Reinforced Concrete Members. *Computers and Structures*, 62(2): pp. 339-352.

- Sorelli, L., Toutlemonde, F. 2005. On the Design of Steel Fibre Reinforced Concrete Tunnel Lining Segments. *11th International Conference on Fracture*, Turin, Italy, March 20-25, 2005.
- Soroushian, P. and Lee, C.D. 1990. Distribution and Orientation of Fibers in Steel Fiber Reinforced Concrete, *ACI Materials Journal*, 87(5): pp. 433-439.
- Stroeven, P., 1977. The Analysis of Fibre Distributions in Fibre Reinforced Materials. *Journal of Microscopy*, 111: pp. 283-295.
- Stroeven, P. 1979. Morphometry of Fibre Reinforced Cementitious Materials, Part II: Inhomogeneity, Segregation and Anisometry of Partially Oriented Fibre Structures. *Materials and Structures*, 12: pp. 9-20.
- Toutanji, H. and Bayasi, Z., 1998 Effect of Manufacturing Techniques on the Flexural Behaviour of Steel Fiber Reinforced Concrete. *Cement and Concrete Research*. 28(1): pp. 115-124.
- Vandewalle, L., et al., Recommendations of RILEM TC162-TDF: Test and Design Methods for Steel Fibre Reinforced Concrete (final recommendation). *Material and structures*, 36: pp. 560-567.
- Venkatesh, M., Jeter, P. 2006. Guideway Steel Fibre Reinforced Concrete Hybrid Girder Design. *The 19th International Conference on Magnetically Levitated Systems and Linear Drives*, Dresden, Germany.

APPENDIX A – Mesh Sensitivity Analysis

A finite element mesh sensitivity analysis was performed to analyse the effects of generating a coarser mesh on the resultant peak loading. The tunnel lining segment modelled in Section 5.2 consisted of 12,528 C3D8 linear brick elements. Due to the mesh dependency phenomenon associated with non-linear finite element analysis, a brick element mesh size of 30 mm was used in the analysis, identical to that of the flexure beam model from which the material properties were established.

The effects of coarser meshes with a smaller number of elements were analysed and the results are plotted in Figure A.1. It was found that as the number of elements increase, and the mesh becomes finer, the model converges to a solution of approximately 168 kN. Given the converging solution, the long computation time (3-6 hours) and lack of high ram computer equipment, further refinements of the mesh was not attempted.

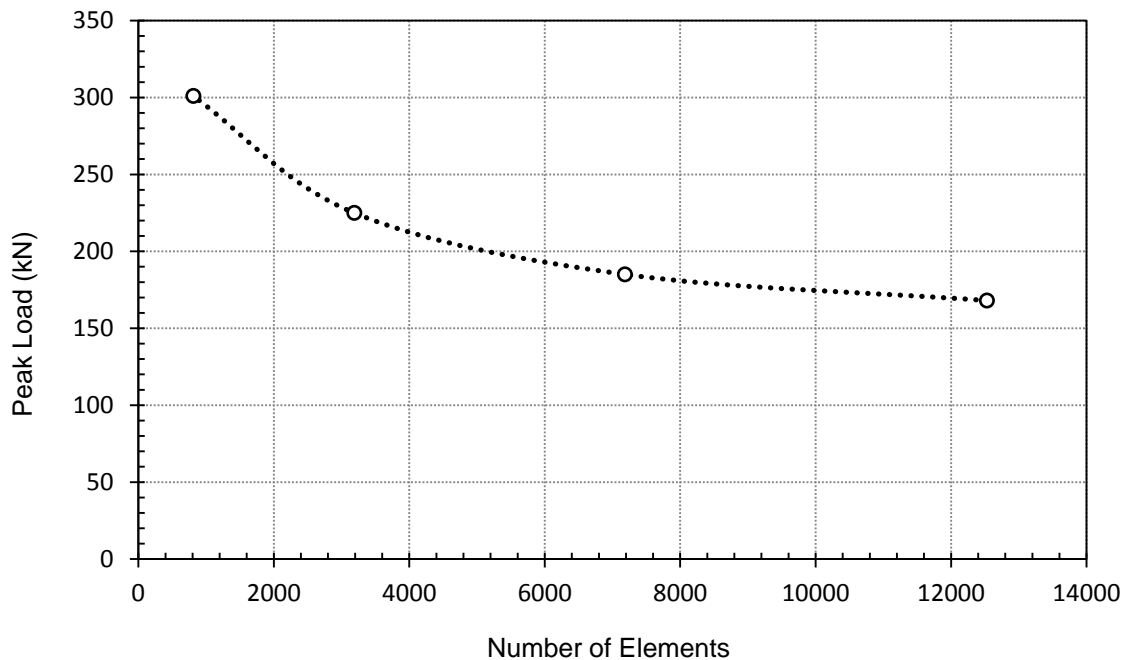


Figure A.1 - Number of mesh elements vs. peak numerical load

APPENDIX B – Input Parameter Sensitivity Analysis

In any finite element analysis, certain parameters can have significant or minor impacts on the output behaviour of the numerical model. A sensitivity analysis was performed on the concrete damage plasticity input parameters to quantify their impact on the flexural behaviour of the steel fibre reinforced concrete tunnel liners. Each material parameter was analysed and a summary of its impact on the output model is presented in Table B.1.

Material Properties	Significant?
Compressive Stress-Strain	✗
Tensile Stress-Strain	✓
Young's Modulus (E)	✓
Poisson's Ratio (ν)	✗
Density (ρ)	✗

Table B.1 - Parameter impact on the model output

Compressive Stress-Strain

The compressive strength of concrete from which the compressive stress-strain relationship is deduced was modified by $\pm 50\%$. By increasing the compressive strength by 50%, it was shown that the model failure was governed by tensile cracking due to the flexural nature of the loading and that an increase in compressive strength had no bearing on the failure. By decreasing the compressive strength of the concrete by 50%, a similar behaviour is experienced up to the peak loading. Post-peak, the low compressive strength causes the segment to fail in a combination of tensile cracking and compressive crushing of the material. In comparison to the observed compressive strength from the laboratory tests with a corresponding standard deviation of 7.34 MPa, the alteration of the compressive stress-strain has little impact on the output behaviour of the model.

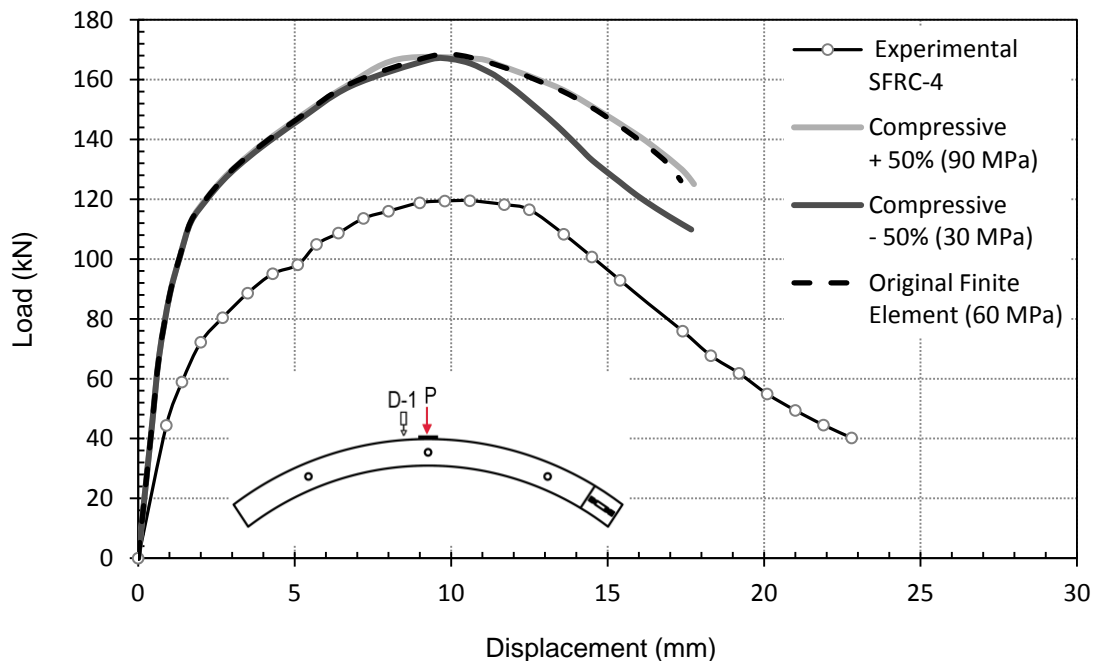


Figure B.1 - Comparison between experimental and finite element results at D-1 with modified compressive stress-strain relationship ($\pm 50\%$)

Poisson's Ratio

The Poisson's ratio is an elastic constant that is a measure of the compressibility of a material perpendicular to the applied stress, or the ratio of latitudinal to longitudinal strain. Typically the Poisson's ratio for concrete ranges between 0.1 – 0.2 (Bencardino *et al.*, 2007), hence 0.15 was chosen as the representative value. Figure B.2 demonstrates that modification of the Poisson's ratio ranging from 0.1 to 0.2 had no impact on the output behaviour of the model.

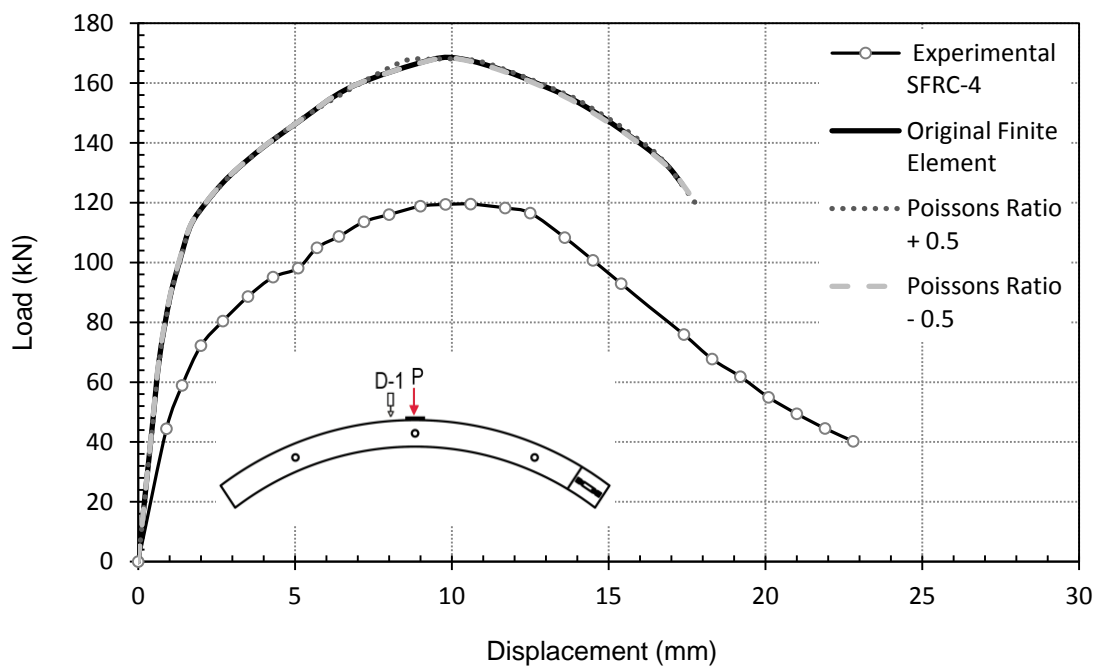


Figure B.2 - Comparison between experimental and finite element results at D-1 with modified Poisson's ratio (± 0.5)

Steel Fibre Reinforced Concrete Density

The structural capacity of the steel fibre reinforced concrete tunnel lining segments may be affected by the material density and self-weight due to the large size of the lining. During storage and transportation, the self-weight of the segments can initiate cracking in the tensile region and cause stress fractures. A sensitivity analysis was executed to analyse the effects of the SFRC material self-weight on the flexural load-carrying capacity of the lining segments. Extreme cases of ignoring the self weight of the specimen (i.e. $\rho = 0 \text{ kg/m}^3$), and increasing it by 100% were examined and the results plotted in Figure B.3. By varying the density input parameters by $\pm 100 \%$, the peak loading resulted in only a $\pm 4.8 \%$ change, demonstrating that only minor impacts on the output of the model are caused by material density compared to the applied flexural loads.

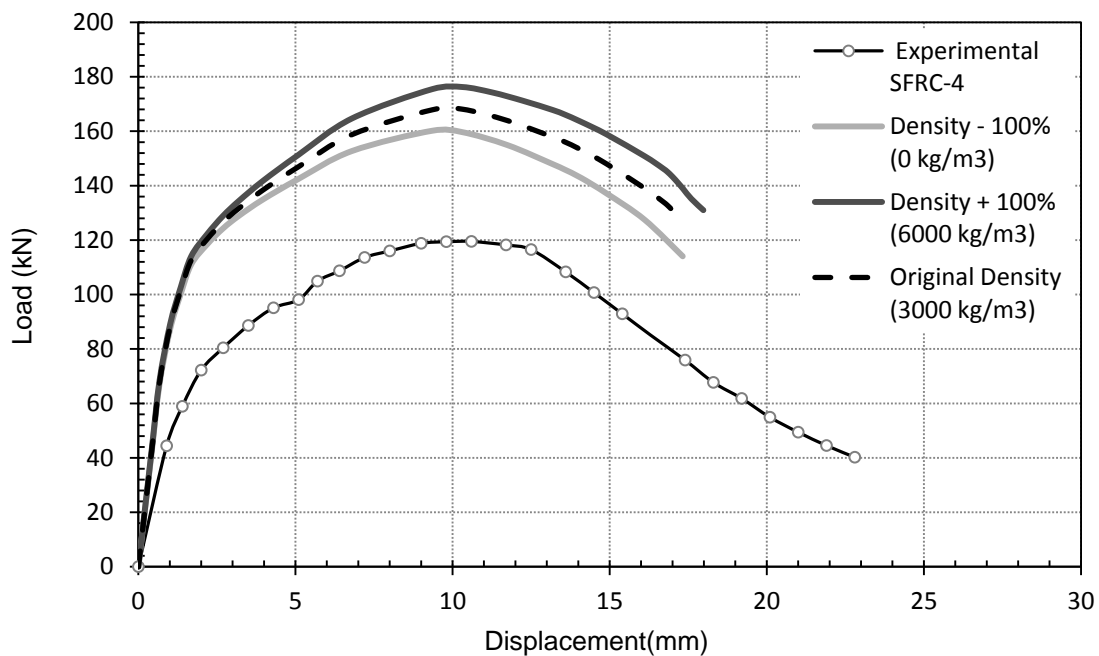


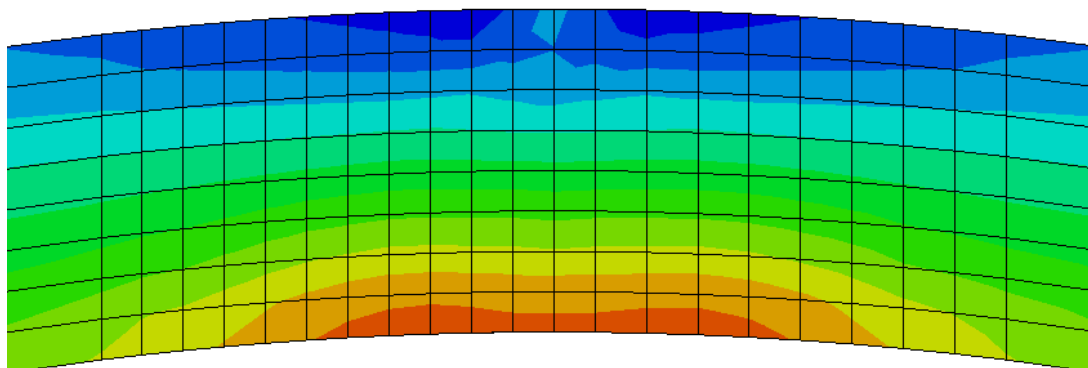
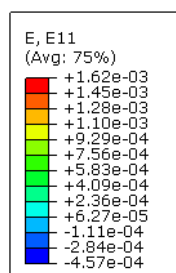
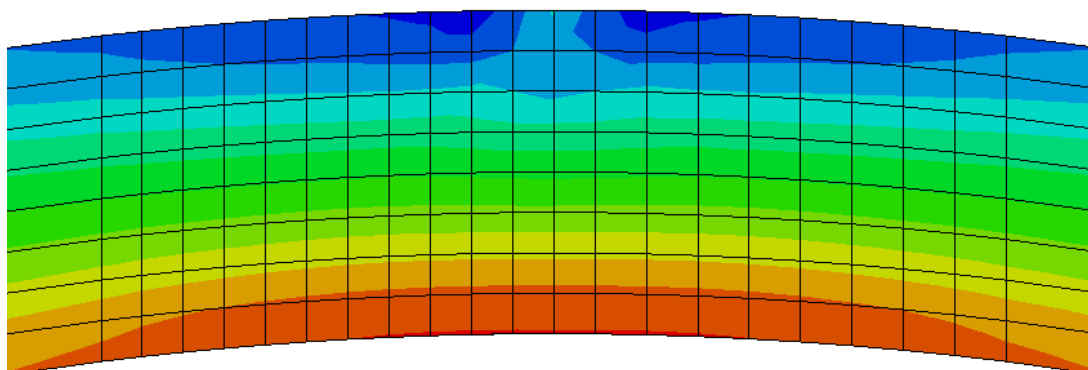
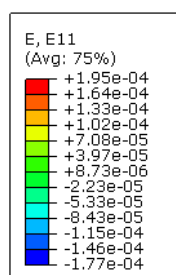
Figure B.3 - Comparison between experimental and finite element results at D-1 with modified concrete density ($\pm 100\%$)

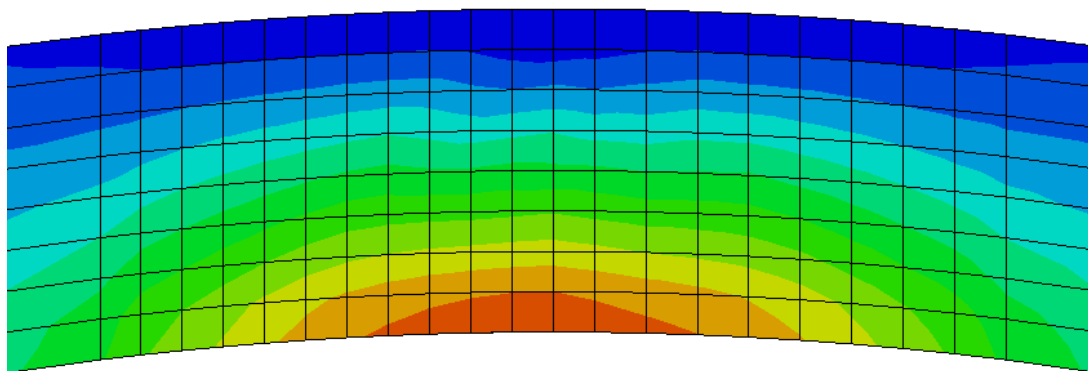
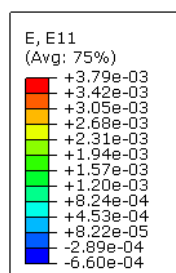
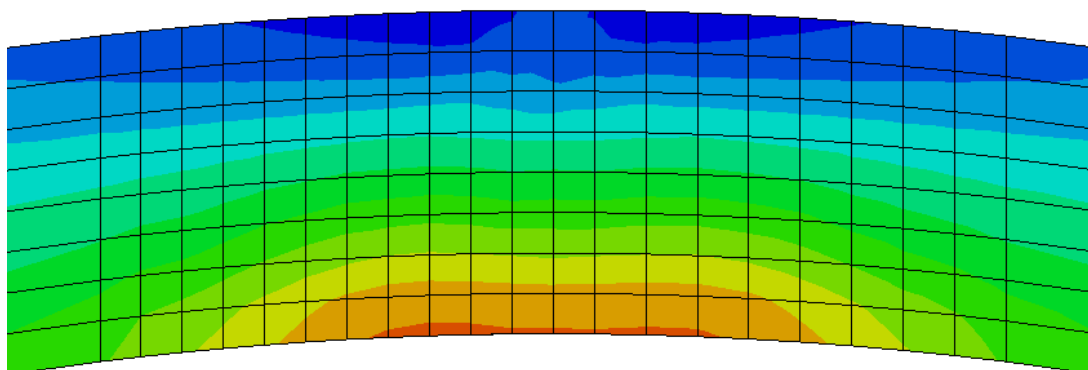
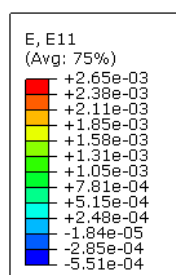
APPENDIX C – Neutral Axis Location Analysis

The location of the neutral axis with midspan displacement of the tunnel lining segments was determined from the experimental and numerical analyses. Table C.1 summarizes the experimental and numerical neutral axis location at different midspan displacements. Figure C.1 visually demonstrates the neutral axis movement as the compressive zone becomes subjected to tensile straining.

Experimental Neutral Axis Analysis	
Midspan Displacement (mm)	Distance of Neutral Axis from Intrados (mm)
4.2	117.0
6.7	168.4
9.0	196.8
12.5	203.8
16.5	213.7
24.4	215.4
Numerical Neutral Axis Analysis	
Midspan Displacement (mm)	Distance of Neutral Axis from Intrados (mm)
3.2	131.0
6.8	175.6
10.3	188.6
15.9	205.2

Table C.1 - Summary of experimental and numerical neutral axis location against displacement





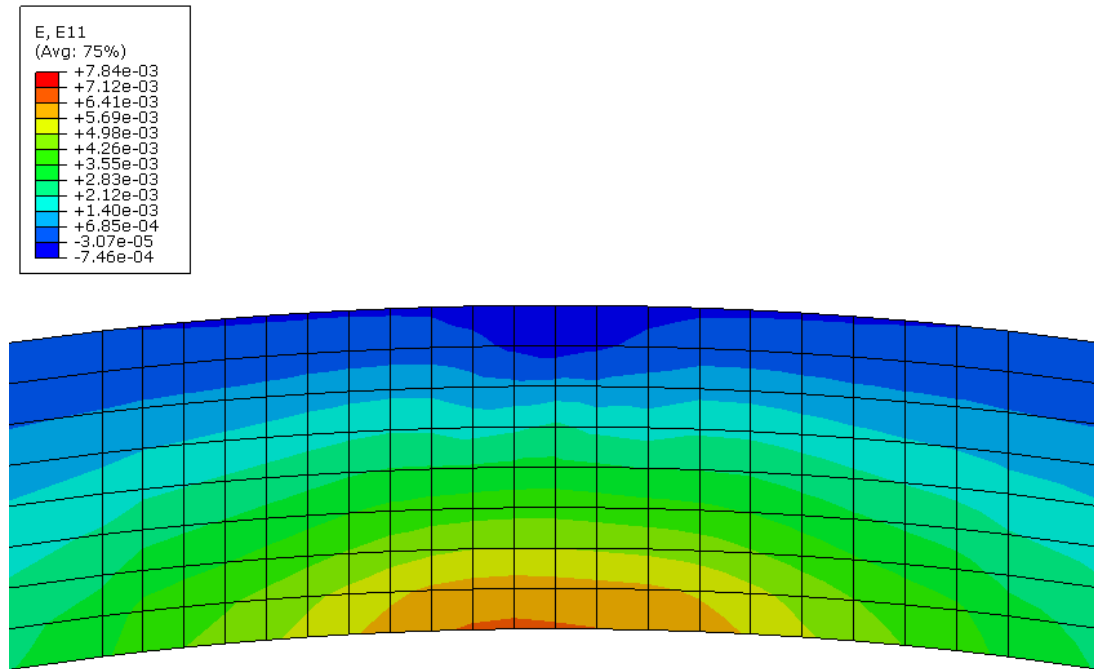


Figure C.1 - Numerical strain plot diagrams

CURRICULUM VITAE

NAME:	Martin Blazejowski
POST-SECONDARY EDUCATION:	<p>The University of Western Ontario London, Ontario, Canada 2009 B.E.Sc.</p> <p>The University of Western Ontario London, Ontario, Canada 2012 M.E.Sc.</p>
RELATED WORK EXPERIENCE:	<p>Junior Engineer Hatch Consulting Engineering 2010-2012</p> <p>Research and Teaching Assistant The University of Western Ontario 2006-2012</p>
HONOURS AND AWARDS:	<p>NSERC Undergraduate Student Research Award 2006-2009</p> <p>Vander Laan Scholarship 2008</p> <p>Sarafinchin Geoengineering Award 2009</p> <p>NSERC Industrial Postgraduate Scholarship 2009-2011</p> <p>William E. & Ruth Lardner Award 2010</p> <p>Dan Eisenstein Memorial Scholarship Tunneling Association of Canada 2011</p>